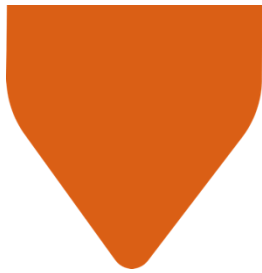# Interreg Sudoe

EUROPEAN UNION

ADDITOOL

European Regional Development Fund

D 2.1. REPORT ON MATERIAL FOR MAM

DATE: 22/02/2023

www.additool.eu

INDEX

1. INTRODUCTION

The Work Package 2 (WP2) of the ADDITOOL project with Title: *Technology transfer from MAM to the tooling sector* proposed to develop and fabricate 5 pilots to transfer the AM technologies to SMEs of the tooling sector in the SUDOE.

This report gathers the description of the manufacture and characterization of raw materials, 3D manufacturing tests, post-processing and characterizations obtained in the Activity 2.1: *Materials for metal additive manufacturing*, and Activity 2.2: *Manufacturing, post-processing and characterisation of demonstrators.*

2.OBJECTIVE

The main objective of this deliverable is to collect the results of the characterization of the different materials used in the five pilots.

3.DESCRIPTION

Table 1 Type of characterisation done by the partners in each pilot.

PILOTS	CHARACTERIZATION						
	Raw material	Microstructure	Mechanical	Thermal Conductivit	Electical Conductivity	Dilatometry &DTA	Tomography
FR1 LAUAK	CEIT	ENIT & LORTEK	ENIT & LORTEK				
PT1 MOLDETIPO	CEIT					ENIT	
SP1 MEUPE/INESPASA		CEIT & ENIT		CEIT	ENIT		
FR2 SOMOCAP	ENIT & LORTEK	CEIT & ENIT	LORTEK & ENIT			ENIT	FADA-CA-TEC & UPV/EHU
PT2 VIDRIMOLDE	CEIT						

4.RESULTS

The characterisation will be based in raw material characterisation, microstructural, chemical and mechanical properties of as-MAM materials and also after post-processing for each pilot. In addition, thermal and electrical conductivity properties will be analysed for the SP1 MEUPE/INESPASA pilot and NDT test will be performed by means of computed tomography analyses in several pilots.

Pilot FR1-LAUAK

Raw material characterization

The original material 40CMD8 is not weldable. Hence a similar material regarding mechanical properties have been selected which can be obtained in powder and wire form.

Table 2. Material specifications regarding mechanical properties for different materials.

	Designation	Re (Mpa)	Rm (Mpa)	A5 (%)
Original	40CMD8 (40CrMnMoS8-6)	850	1000	11
Proposal	EN4334 (15CrMnMoV5-4-9-3) // AIR 9117 : 15CDV6	930	1080 - 1280	10

A batch of 10 kg of powder 15CDV6 (AIR 9117) was gas-atomized on the atomisation pilot plant of CEIT. The powder was sieved in order to obtain the required powder size range for LMD process, +44-106 µm with an average size of 73 µm, Table 3. The powder shows spherical shape with high sphericity (close to one) and very low amount of satellites, which make it suitable for additive manufacturing technologies, Figure 1, Figure 2.
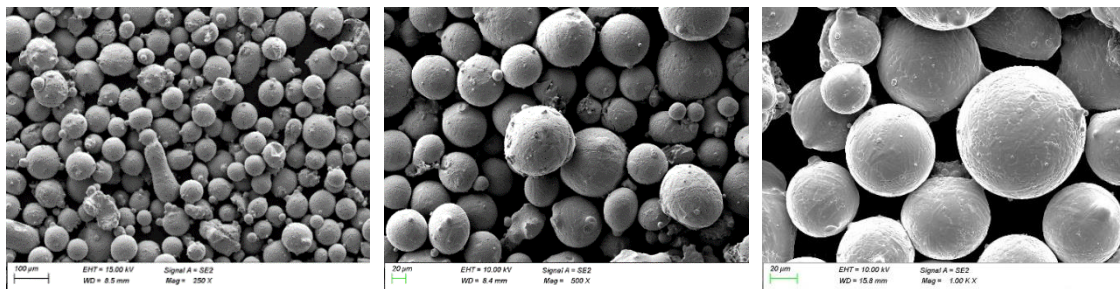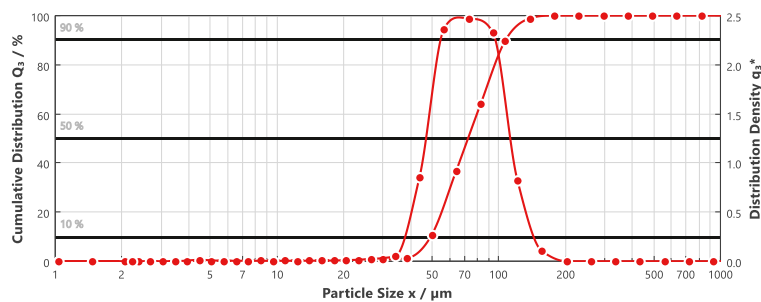

Figure 1. FEG-SEM images of the atomized 15CDV6 powder.

Table 3. Particle size distribution and sphericity of the 15CDV6 powder

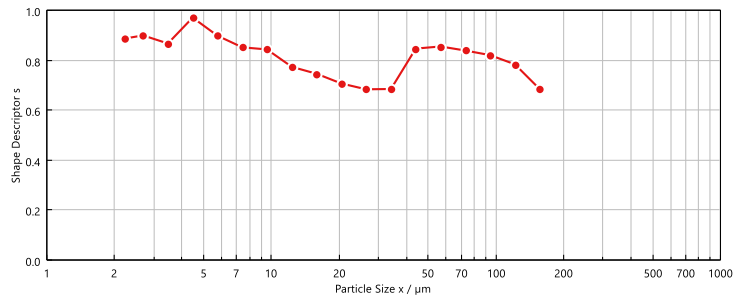| Dv(10) (µm)	49.00	S (10)	0.74
Dv(50) (µm)	73.31	S (50)	0.84
Dv(90) (µm)	107.68	S (90)	0.93

Figure 2. Particle size distribution (up) and shape factor (bottom) as function of the particle size of the 15CDV6 powder.

Physical properties of this powder, flowability and density, were also within the expected ranges, Table 4.

Table 4. Physical properties of 15CDV6 powder

Flow rate (s/50g)	Apparent density (g/cm^3)	Tap density (g/cm^3)	Pycnometer density (g/cm^3)
0.33	4,31	4,54	7,68

Cross section images of the powder were analysed, Figure 3. There was no presence of internal gas pores and the particles were enriched with Si, V, Mo y Mn.
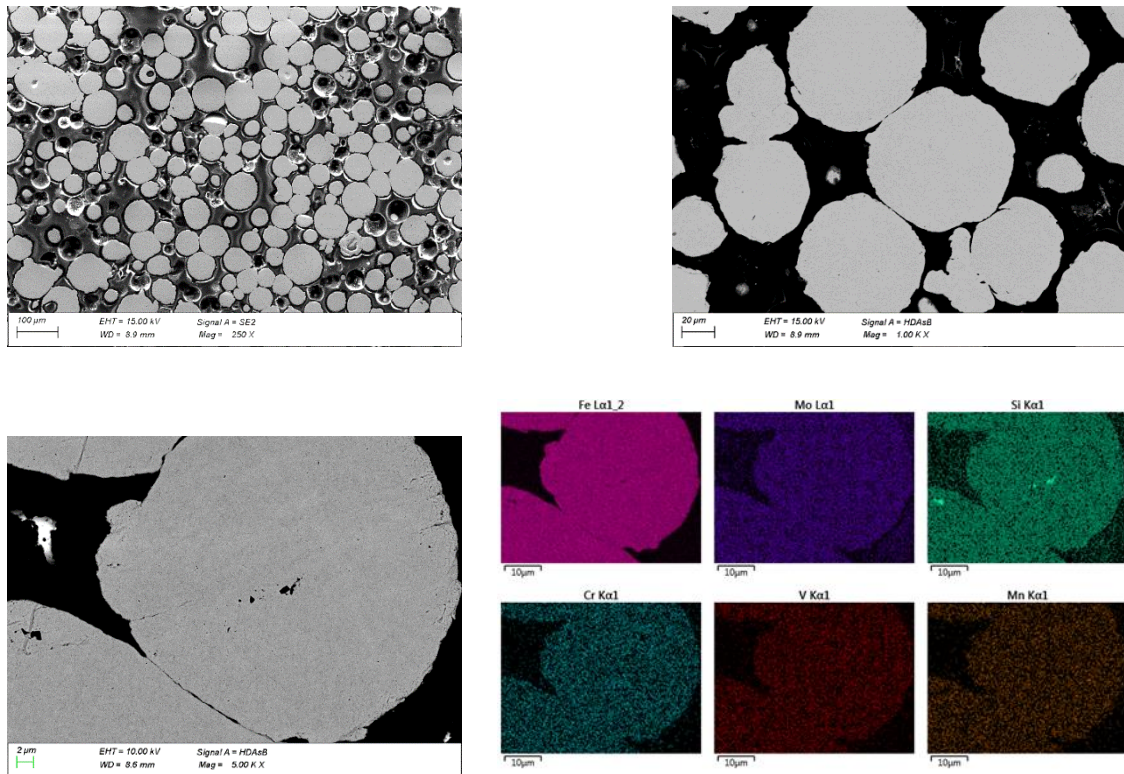

Figure 3. FEG-SEM images and EDS analysis of the atomized 15CDV6 powder.

The chemical composition of the powder measured by ICP and the interstitial content by LECO is gathered in Table 5 Chemical composition 15CDV6 powderTable 5.

Table 5 Chemical composition 15CDV6 powder

Element	Mn	Si	Cr	Mo	V	P	C	O	S	N	Fe
(%wt.)	1.01	0.150	1.57	0.94	0.287	N.D.	0,122	0,0126	0,0049	0,0014	95.8
Min-Max	0.8-1.1	Max. 0,2	1,25-1,50	0,80-1,00	0,20-0,30	Max. 0,02	0,12-0,15	-	Max.0.0015	-	-

Microstructural characterisation

Processed material with DED-Wire laser (LMD-W)

The metallurgical state and the mechanical properties of four DED-wire walls were studied, Figure 4.
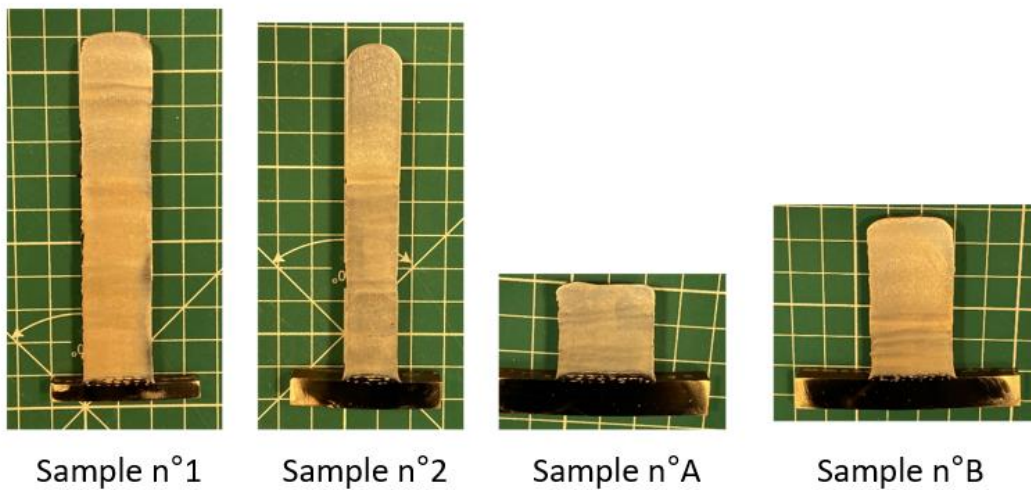
Figure 4. Metallographic sections of the different WLAM 15CrMoV6 walls.

The composition of the walls was determined by UV spark spectrometry. Several zones in the height of the walls were analysed (Figure 23). The results of the analyses are presented in Table 6. The composition of the walls is homogeneous; it corresponds well to a standard low-alloy 15CrMoV6.
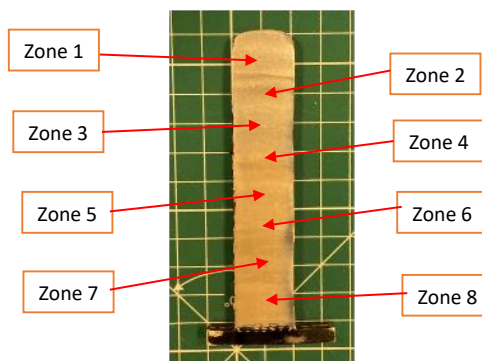
Figure 5. localisation of different zones of analyses (sample 1).

Table 6. composition of different areas measured by UV spark spectrometry.

	Fe	C	Si	Mn	P	S	Cr	Mo	Ni	V
Zone 1	95,92	0,127	0,162	0,85	0,006	-	1,4	0,92	0,187	0,246
Zone 2	95,99	0,12	0,148	0,85	0,006	-	1,397	0,91	0,182	0,237
Zone 3	95,94	0,127	0,149	0,85	0,006	-	1,401	0,92	0,183	0,24
Zone 4	95,99	0,131	0,147	0,85	0,006	-	1,394	0,91	0,185	0,24
Zone 5	95,99	0,113	0,15	0,85	0,006	-	1,403	0,91	0,188	0,243
Zone 6	95,97	0,121	0,148	0,84	0,005	-	1,398	0,91	0,185	0,241
Zone 7	95,99	0,123	0,142	0,837	0,006	-	1,404	0,89	0,187	0,238
Zone 8	95,95	0,127	0,149	0,85	0,0061	-	1,426	0,9	0,205	0,241
316L	Bal.	<0,03	<0,75	<2	<0,045	<0,03	16-18	2-3	10-14	
15CrMoV6		0.12-0.18	0.2	0.8-1	<0.02	<0.015	0.25-1.5	0.8-1		0.2-0.3

The microstructure of the walls was analysed by optical microscopy according to their construction direction. Figure 6and Figure 7 show the different micrographs obtained for sample 1. No material health defects (porosity, cracks) were observed. The fine structure corresponds to tempered martensite or even bainite. No evolution of the microstructure along the building direction was noticed.
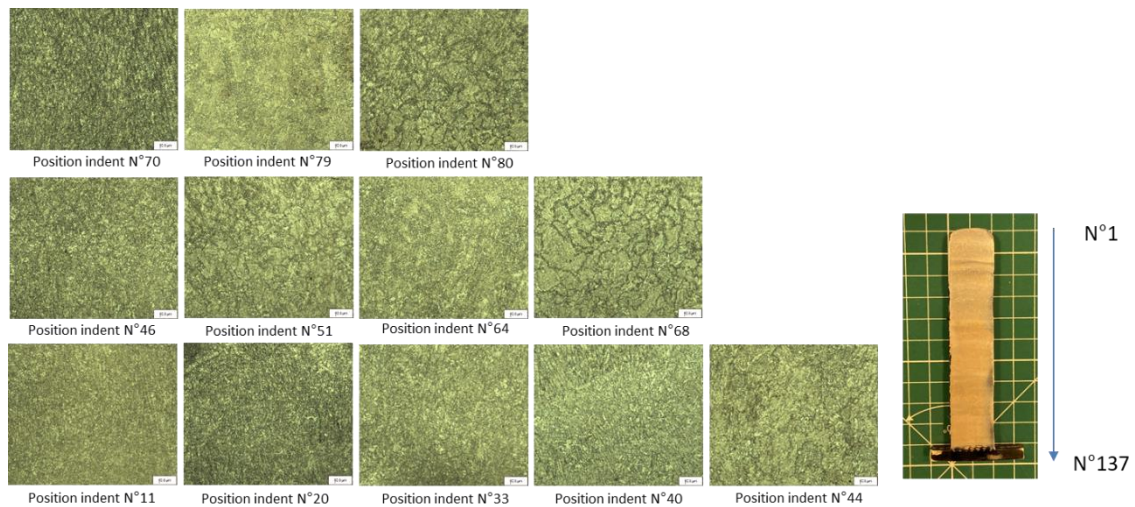

Figure 6. Microstructural observations by optical microscopy obtained at the top of wall 1
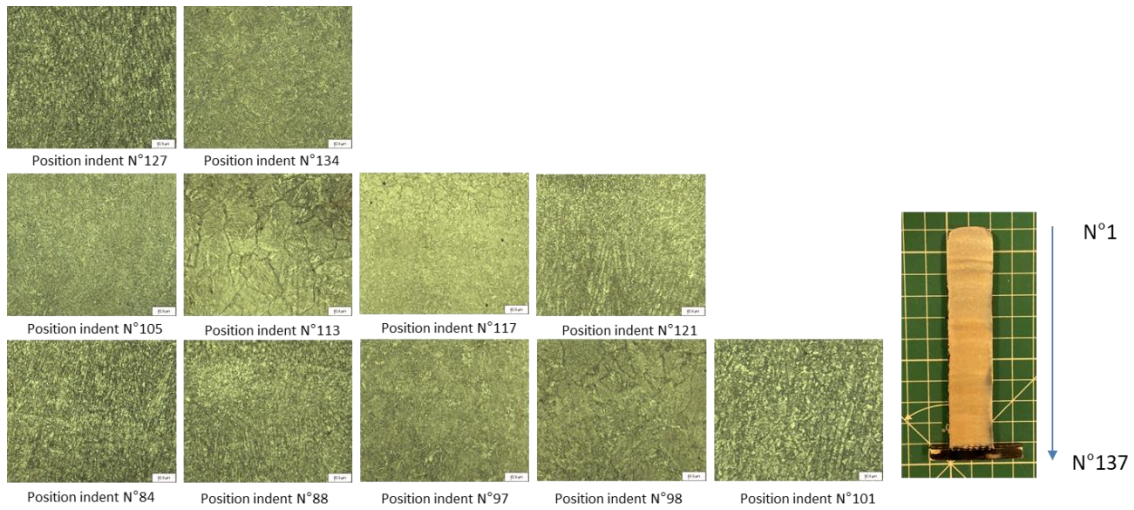
Figure 7. Microstructural observations by optical microscopy obtained at the top of wall 1

The microstructure at the interface between the 15CrMoV6 low alloy steel wall and the 316L stainless steel substrate is shown in Figure 8. Zones of different contrasts, after Nital etching, make up this zone, as corroborated by the micrographs in Figure 24.
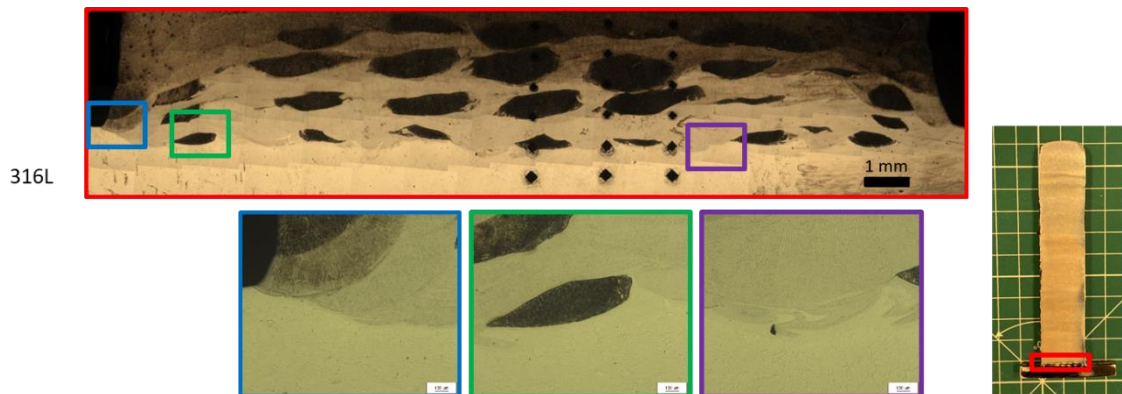

Figure 8. Microstructural observations by optical microscopy of the interface between the wall (15CrMoV6) and the substrate (316L).

They correspond to areas with different chemical compositions (Figure 9 and Figure 10). The dark and light areas correspond to regions with the composition of 15CrMoV6 steel and 316L stainless steel, respectively.
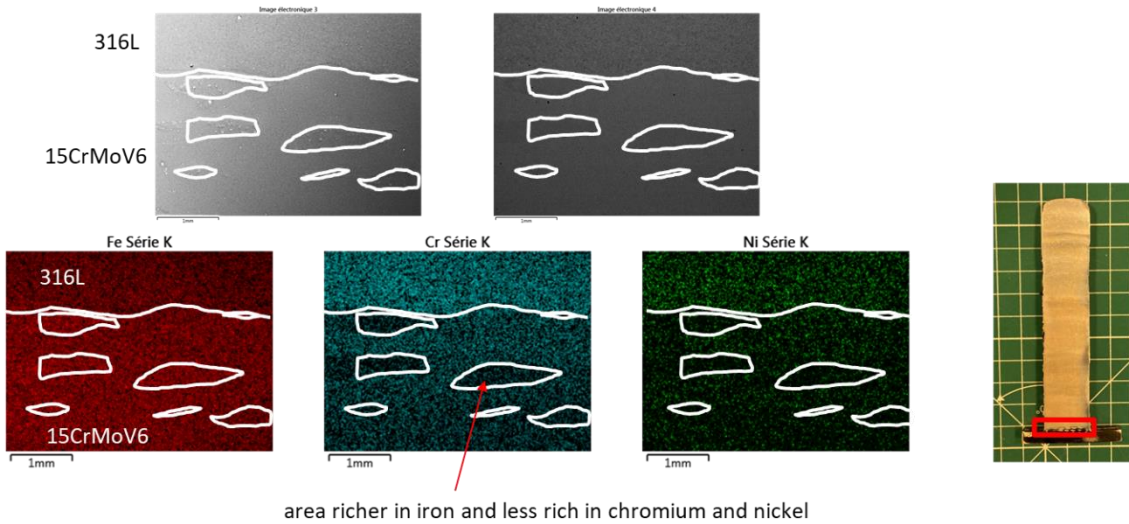
area richer in iron and less rich in chromium and nickel

Figure 9. EDS maps of the interfacial zones between the wall and the substrate.

Si	0,21
V	0
Cr	1,5
Mn	1,06
Fe	96,92
Ni	0
Mo	0

Si	0,29
V	0,21
Cr	7,61
Mn	1,26
Fe	85,27
Ni	3,97
Mo	1,38

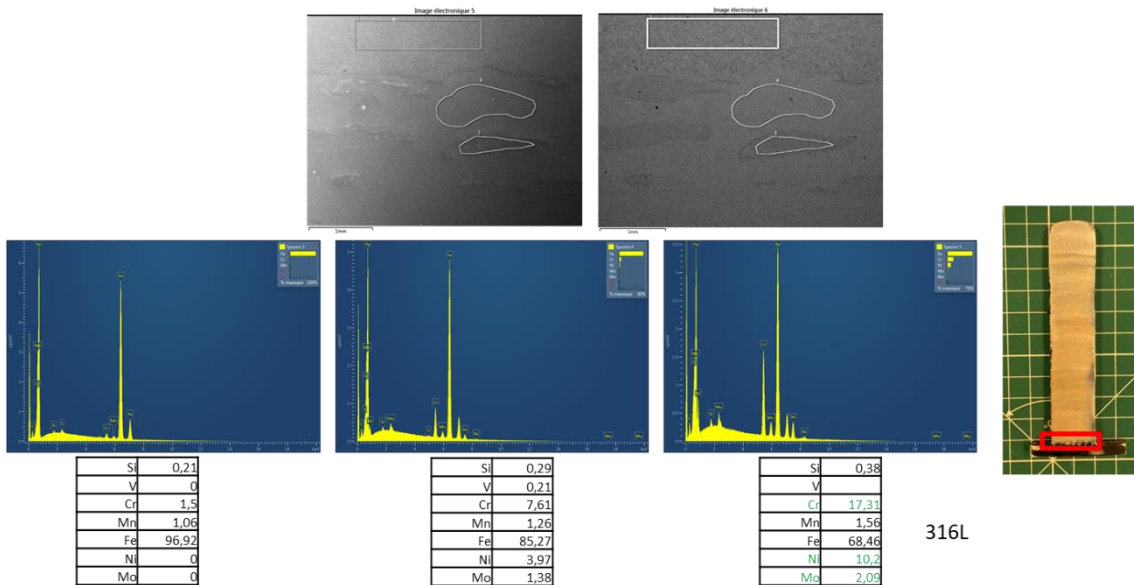| Si	0,38
V	
Cr	17,31
Mn	1,56
Fe	68,46
Ni	10,2
Mo	2,09

Figure 10. EDS analyses of the interfacial zones between the wall and the substrate.

Processed material with DED wire arc (WAAM)

Weld bead geometry and soundness was checked to select the best welding parameters, **¡Error! No se encuentra el origen de la referencia.**. For that, the cross sections of the weld beads were analysed in the optical microscope. The selected weld bead had a thickness of 7.08 mm and a height of 2.5 mm.
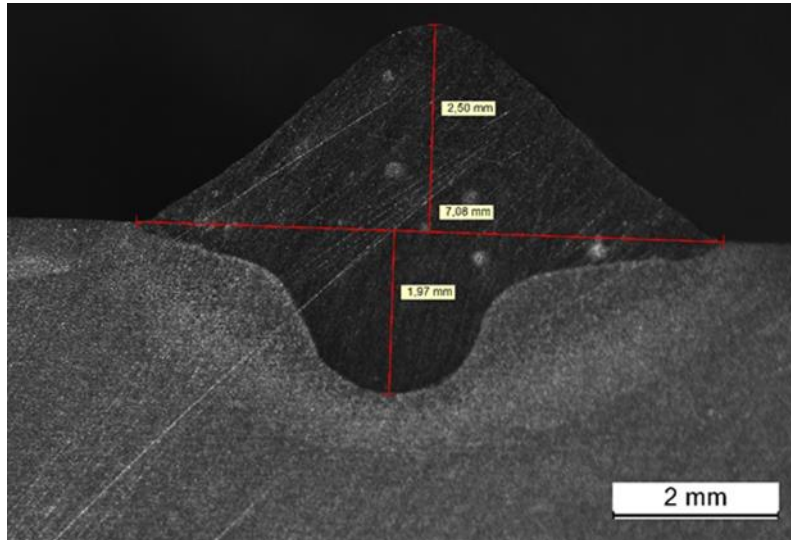
Figure 11. Image of deposited weld bead.

Moreover, the cross sections of small parts were also analysed to select the best strategies to grow in height. Walls done by two overlapped weld beads and circling strategies were analysed.
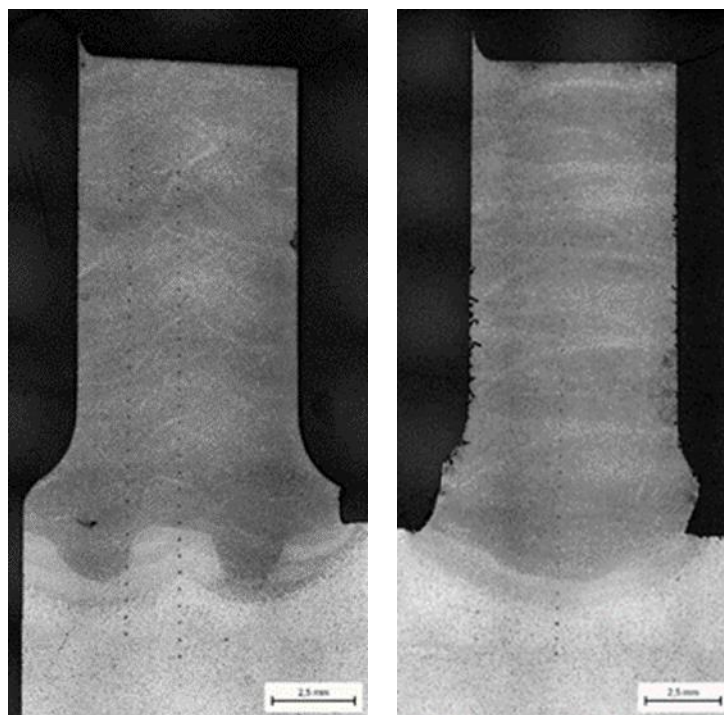

Figure 12. Cross section of wall and their microstructure. Left: two overlapped weld beads. Right: single weld bead by circling.

As can be observed from the microstructure, quasi homogenous microstructure was found without columnar grains with both strategies, **¡Error! No se encuentra el origen de la referencia.**. However, the heat affected zones with the two overlapped weld beads shows a more complex shapes than the circling strategy with single weld bead per layer.

At higher magnifications, expected microstructure was found for both strategies, composed by non-preferentially oriented small and equiaxed grains.
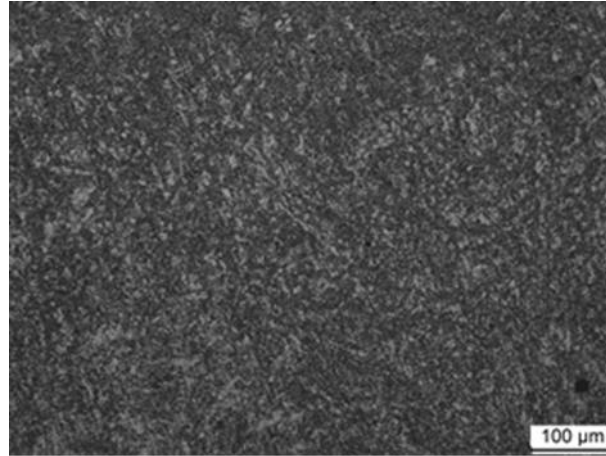
Figure 13. Higher magnification of deposited material microstructure composed by non-preferentially oriented small and equiaxed grains.

Mechanical characterisation

Processed material with DED-Wire laser (LMD-W)

More than one hundred Vickers HV10 hardness measurements were carried out at the height of the wall. The hardness varies between 300 and 350 HV10. These values correspond to a bainitic structure or a tempered martensite structure. No evolution of hardness on the sample height was noticed. Hardness measurements at lower loads were carried out at the interface, Figure 14 and Figure 15. A hardness gradient is observed between the wall and the substrate. This hardness gradient between the 15CrMoV6 and 316L stainless steel rich zones can also be observed.
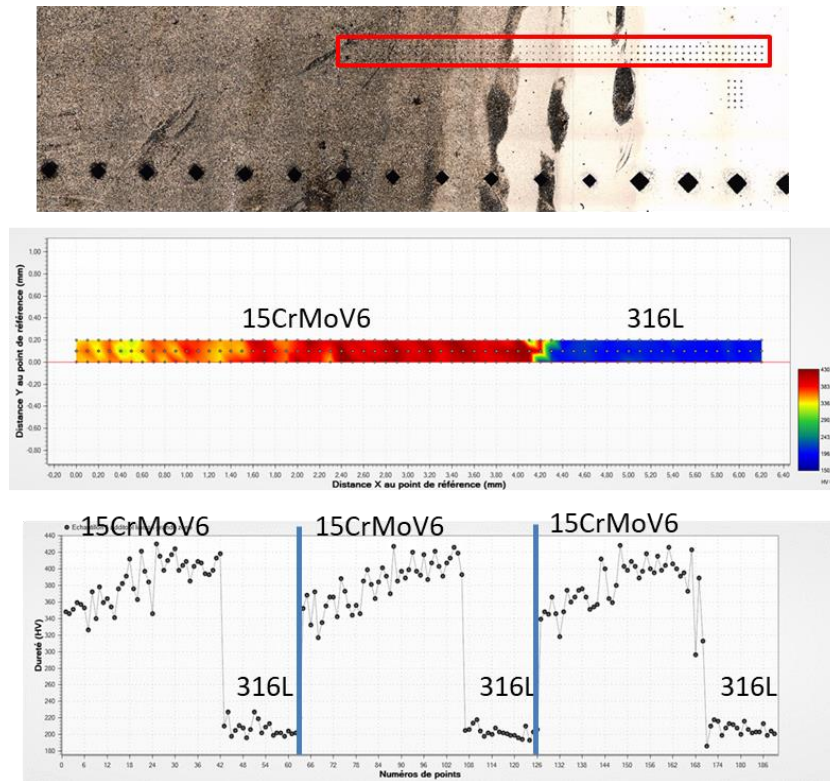
Figure 14. Hardness evolution at wall/substrate interface
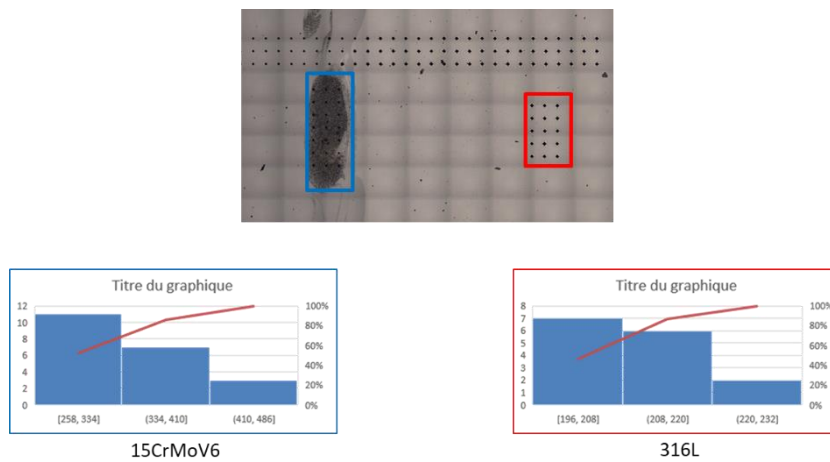

Figure 15. Hardness values of zones with different chemical compositions at the interface.

The tensile behavior of the wall material was also determined by tensile testing. The tests were conducted at room temperature at an imposed displacement speed of 2 mm/min. The tensile curves are shown in Figure 16.
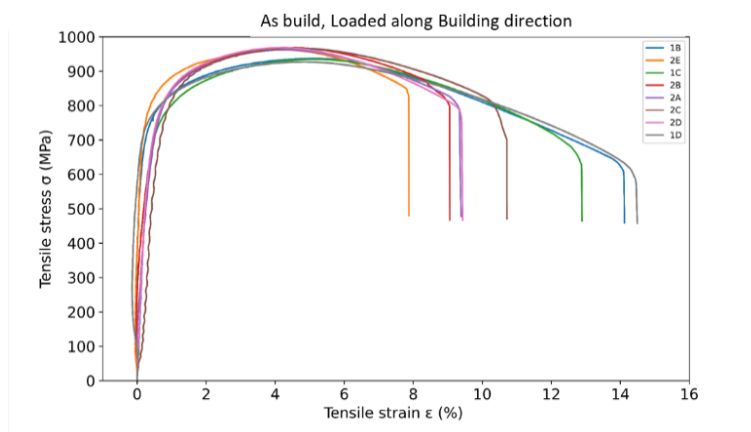
Figure 16. Tensile curves of vertical specimens taken from DED-wire walls.

The values for yield strength, maximum strength and elongation are given in Table 7.

Table 7.mechanical properties of 15CrMoV6 steel walls.

	YS	UTA	A%
Wall 1	747	936	13
Wall 2	782	966	9

The deformation fields of the specimens during the tensile test were also measured by digital image correlation. The maximum deformation of the specimen appears in a zone of resumption of wall after a voluntary stop of manufacturing (Figure 17).
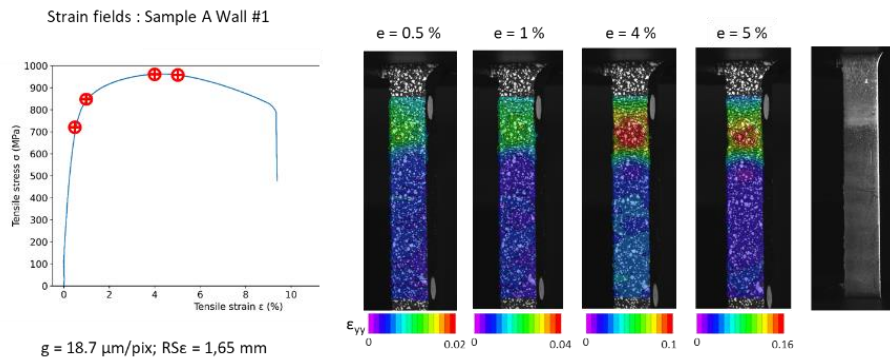
Figure 17. Deformation fields determined by digital image correlation.

Fractographic observations of the fractured zones confirm the high elongations at the break. The fracture surfaces show numerous cupules, which attest to ductile behavior, Figure 18.

Figure 18. Fractographic observations of tensile specimens after failure.

Processed material with DED wire arc (WAAM)

From big walls tensile specimens were extracted following the ASTM E8 standard in two orientations.

Figure 19. Position and geometry of ASTM E8 tensile specimens extracted from the WAAM wall.

The obtained mechanical properties from tensile tests at room temperature are shown in Table 8.

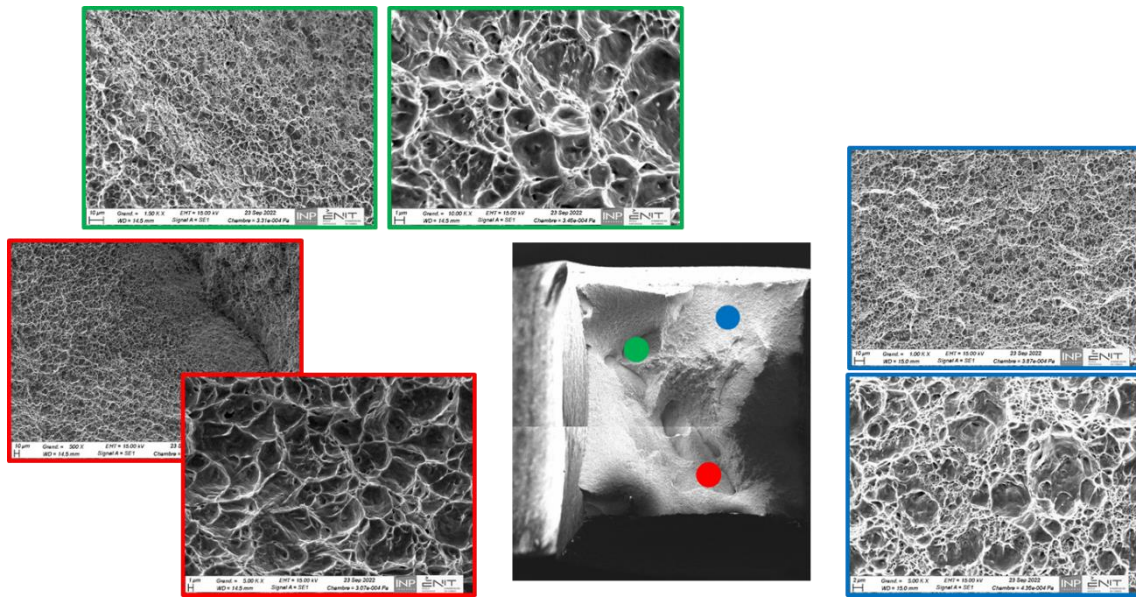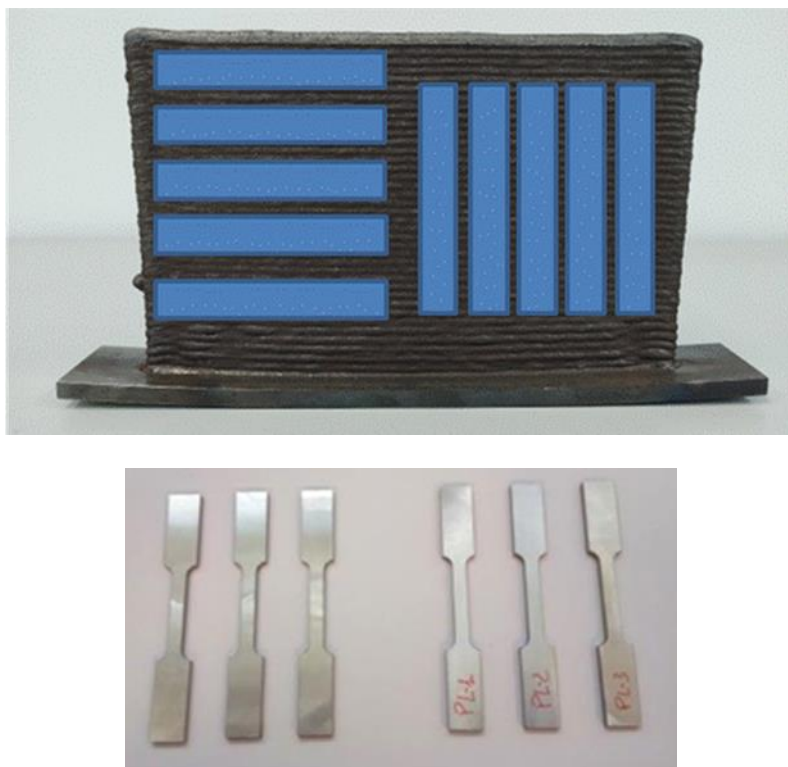*Table 8. Obtained mechanical properties from tensile test.*

Orientation	Elastic limit (MPa)	UTS (MPa)	Elongation (%)
Vertical	777.8 ± 8.5	1005.8 ± 7,5	12.3 ± 2.4
Horizontal	7744 ± 5.9	1031.8 ± 11.4	11.9 ± 3.7

No anisotropy was detected between orientations. Compared with the material specifications and the original material of the part done with conventional processes (40CMD8), obtained results were very close.

9

Regarding the microhardness, an expected transition was found between the metal base and the WAAM part. The WAAM part obtained an average hardness of 330 HV1, which could be enhanced with a posterior thermal treatment. The oscillations are due to the interlayer and weld bead differences.
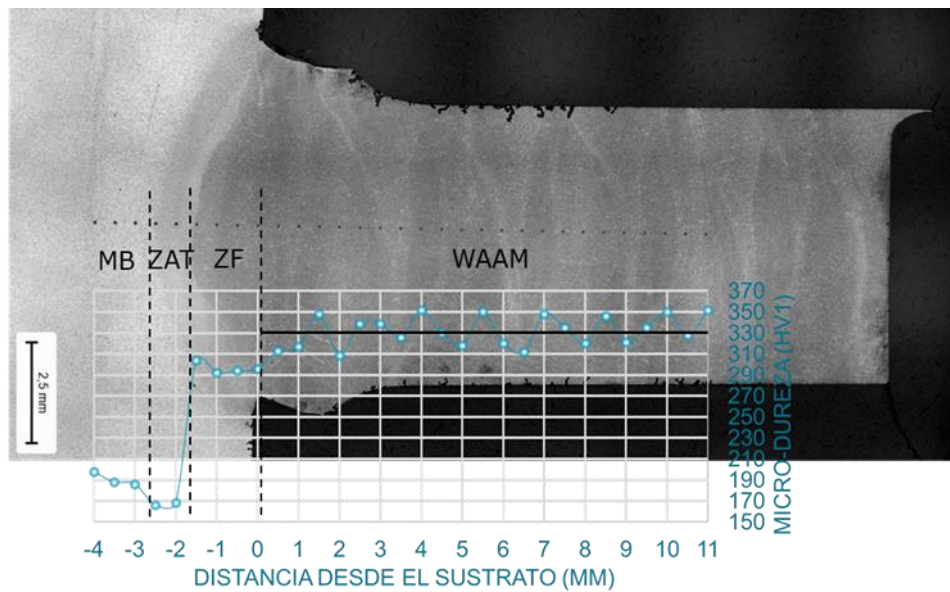

Figure 20. Image of the wall with the measured HV1 microhardness from the substrate to the wall.

The hardness evolution at the interface between the substrate and the wall was confirmed by low-load hardness tests (Figure 21 and Figure 22).
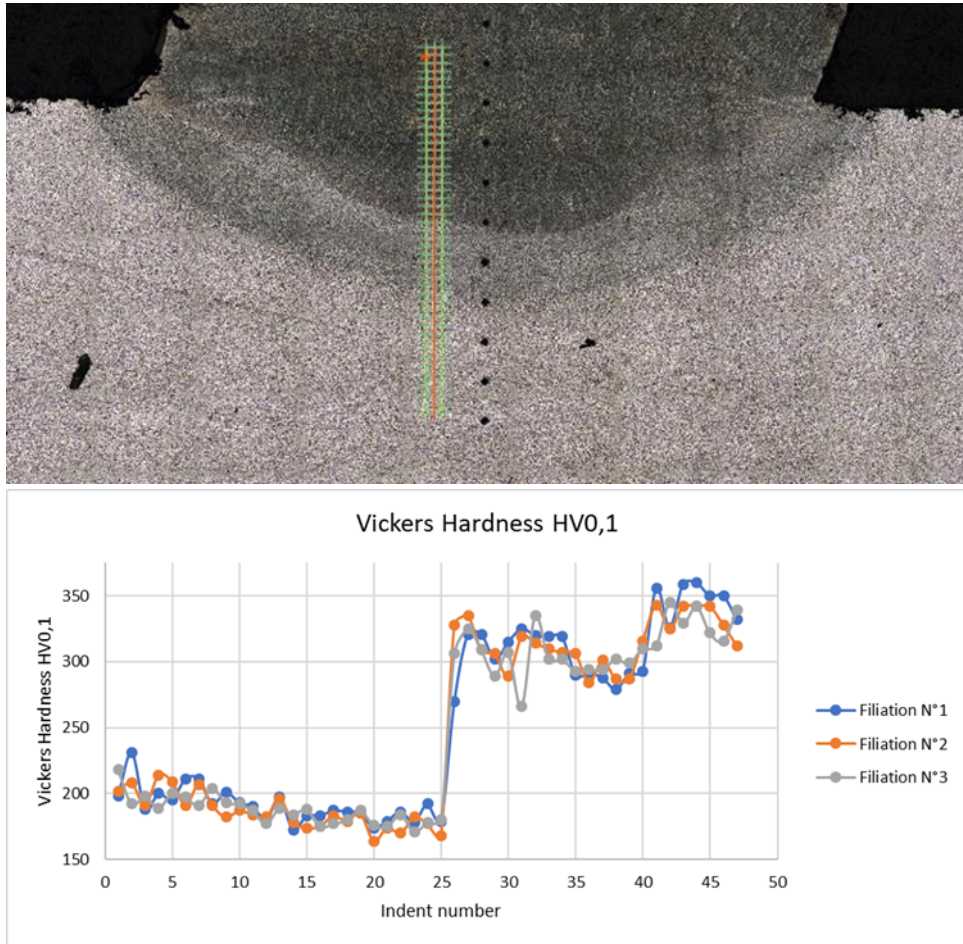
Figure 21. Image of the wall with the measured HV1 microhardness from the substrate to the wall.
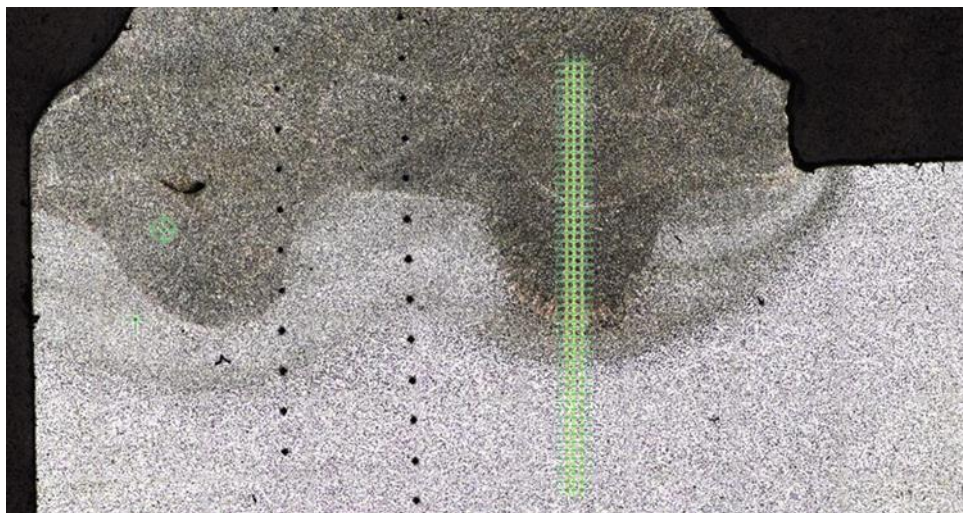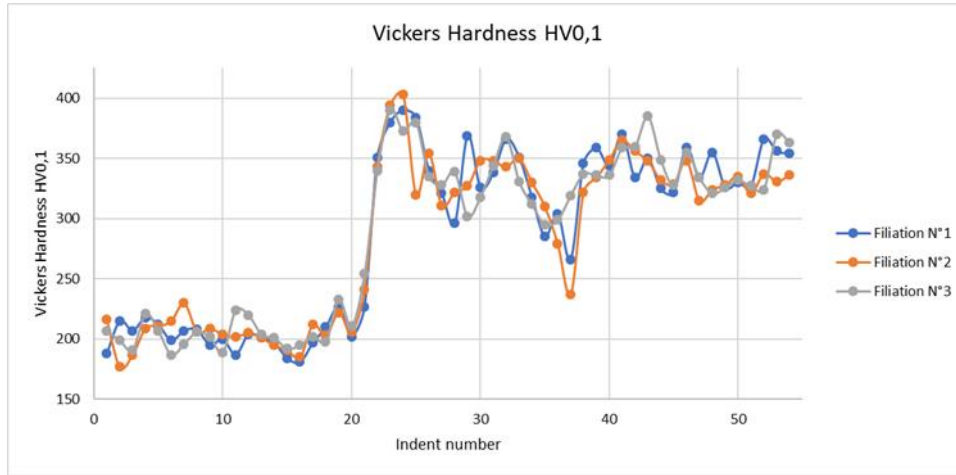
Figure 22. Evolution of the microhardness at the interface between the substrate and the wall (two overlapped weld beads)

Pilot PT1-MOLDETIPO

<u>Raw material characterization</u>

Physical properties and chemical composition of W360 powder with particle size +20-45 µm are gathered below, Table 10 and Table 11.

Table 10. Physical properties W360 powder

Flow rate (s/50g)	Apparent density (g/cm^3)	Tap density (g/cm^3)	Pycnometer density (g/cm^3)
No Flow	3.78	4.43	7.74

Table 11. Chemical composition of W360 powder.

Elements	C	S	Mn	Cr	Mo	V	O	N	C	S
(%wt.)	0,50	0,20	0,20	4,50	3,00	0,55	0.280	0.004	0.481	0.0007

Electronic microscopy (SEM) images show a typical gas atomised powder with generally spherical shape and with the presence of several satellites and some splat, Figure 23.
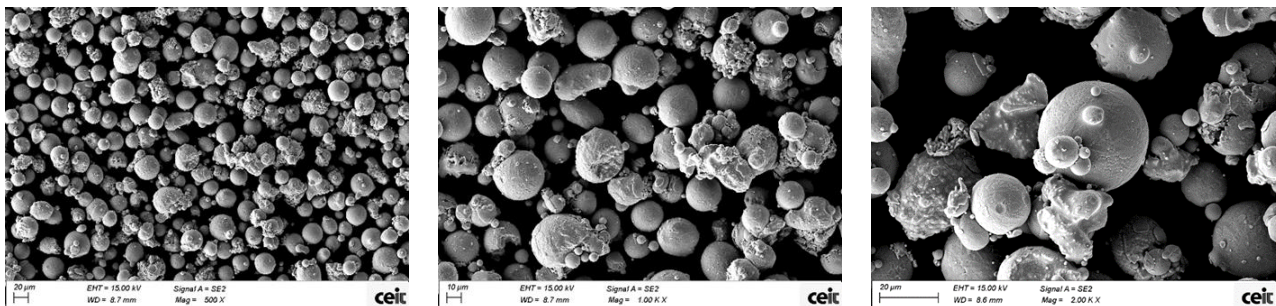
Figure 23. FEG-SEM images of W360 powder. Spherical morphology showing some satellites.

Cross section images of polished powder have been analysed. There is no presence of internal porosity and the EDS analyses show homogeneous distribution of S, V, Mo and Mn (Figure 24).
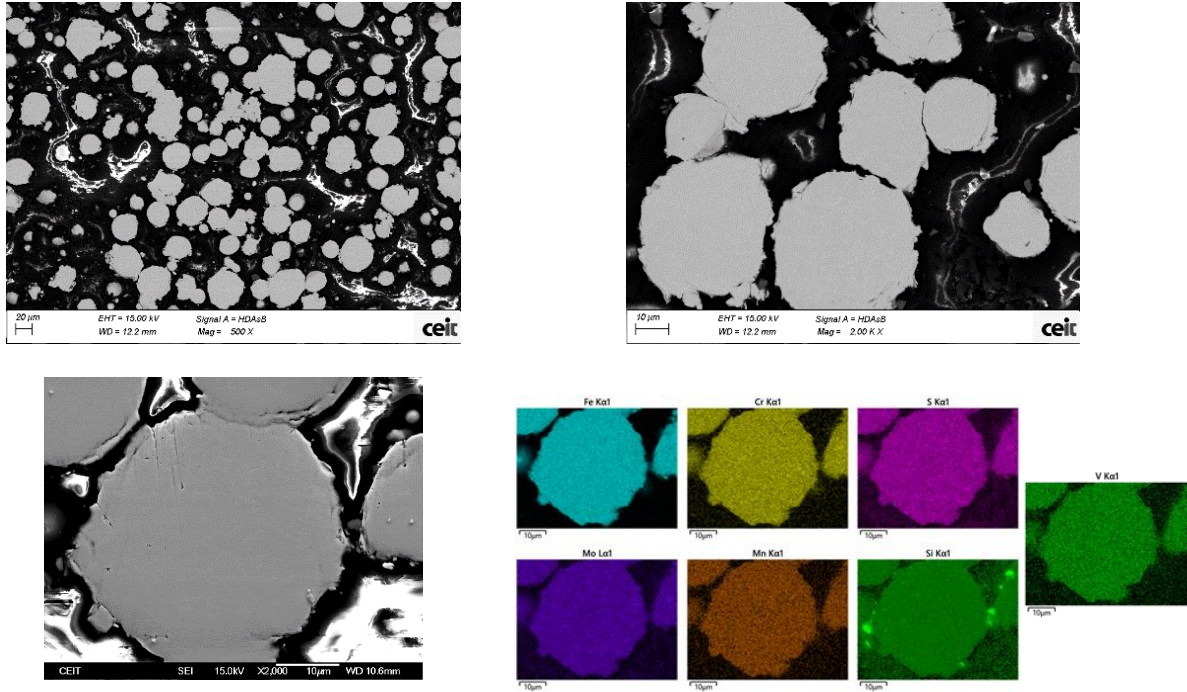
Figure 24. FEG SEM images and EDS analysis (bottom) of the W360 powder

Particle size distribution and powder sphericity has been measured using a Sympatec QIPIC/L02 with Rodos and Vibri as dispersion modules and results are collected in Figure 25 and Table 12. It can be asserted that both fulfil the requirements to be deposited by LPBF (sphericity close to one) with an average powder particle size of 32 µm.

Table 12. Particle size distribution and sphericity of the W360´s powder

Dv(10) (µm)	21.25	S (10)	0.66
Dv(50) (µm)	32.05	S (50)	0.81
Dv(90) (µm)	45.77	S (90)	0.90
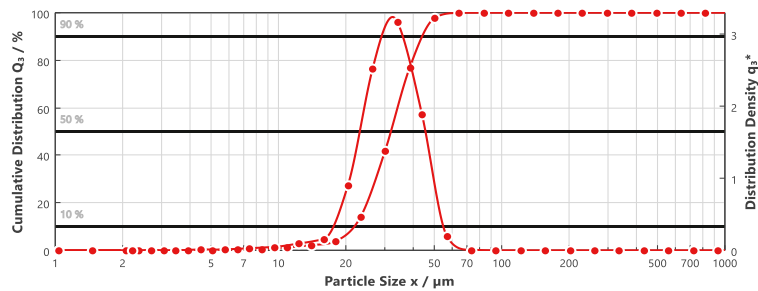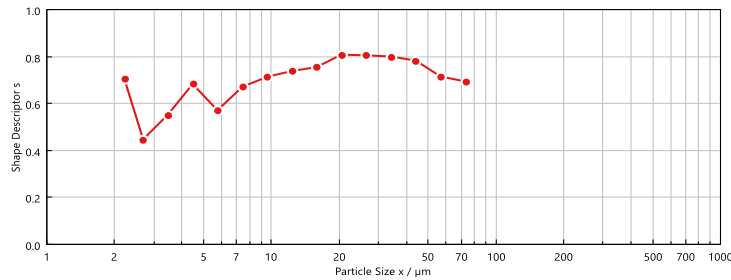
Figure 25. Particle size distribution (up) and shape factor (bottom) as function of the particle size of the W360´s powder.

Microstructural characterisation

In this part, the first production defect will be investigated with the surface roughness and internal defect analysis then macro and microstructure will be analysed.

Methods

Surface roughness was measured using a numerical microscope (Keyence) with the 3D mapping mode. For the material health and microstructure characterization, sample cross-sections were observed using an optical microscope Olympus PMG3 and a ZEISS EVO HD15LS scanning electron microscope (SEM) coupled with an energy-dispersive X-ray (EDX; Oxford). The sample preparations consisted of several steps, starting with automatic mechanical polishing (Mecatech 334) and ending with P4000 SiC grit papers. The final polishing steps were performed using colloid diamond solutions (3 µm, 1 µm) and oxide polishing solutions (OPS). A Nital etchant (97 mL ethanol, 3 mL nitric acid) revealed the microstructure. Quantitative image analysis was performed using Fiji image analysis software[1]. XRD spectra were recorded using a Philips X'PERT machine, utilizing Cu-Kα radiation with a wavelength of 1,540598 Å and Position Sensitive Device (PSD) (acquisition in a circular angle of 8°). The samples were scanned from 20° to 90° with a step size of 0.022° and 2000 s per step.

Results: Composition

The as-built sample composition was measured by a Foundry Master spark OES spectrometer (Oxford). 6 measurements were done, and the result is displayed in Table 13. Except for the presence of tungsten, the composition is consistent with the one given by Böhler for the powder.

Table 13. Material composition (weight per cent).

(w%)	Fe	C	Si	Mn	Cr	Mo	V	W
Powder (Böhler data)	Bal.	0.5	0.2	0.25	4.5	3	0.55	/
Isobloc (Böhler data)	Bal.	0.5	0.2	0.25	4.5	3	0.6	/
As-built LPBF (exp)	91.05 ±0.02	0.459 ±0.004	0.181 ±0.003	0.207 ±0.002	4.42 ±0.02	2.83 ±0.01	0.582 ±0.002	0.128 ±0.004

Results: Material Health

Surface roughness

Samples were built with a chess scanning strategy. An example of the measure of the roughness on one island (top layer) is shown in Figure 26. Results give an average of Sa = 17.4 µm. This value is quite in the upper range of the literature and may be decreased by changing strategy and optimizing lasing parameters [2]–[6].
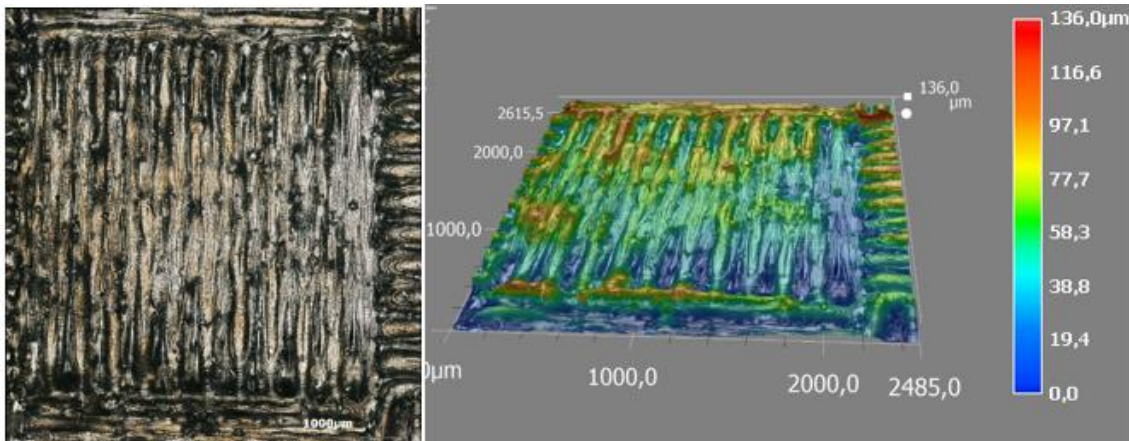
Figure 26. Micrograph of surface (left), 3D surface analysis (right).

Qualitative defect analysis

Polished surfaces were observed to investigate the materials' health. The result of this investigation is shown in Figure 27. Some pores are visible in the bulk part, and some are aligned in the building directions. These last ones may be explained by a contouring strategy [7][8]. In addition, some microcracks are observed in the upper area, especially in the last layer. Tool steel, such as AISI M2 and AISI M50, with a composition close to W360, are well known to be prone to cracking. Avoiding cracking is reached by reducing the thermal gradient by pre-heating the build plate [9]–[11]. The crack observed in the last layer may result from the different thermal history compared to the bulk area. Due to the upskin and contouring effect, defects will be removed by machining; therefore, there are not expected to be harmful.
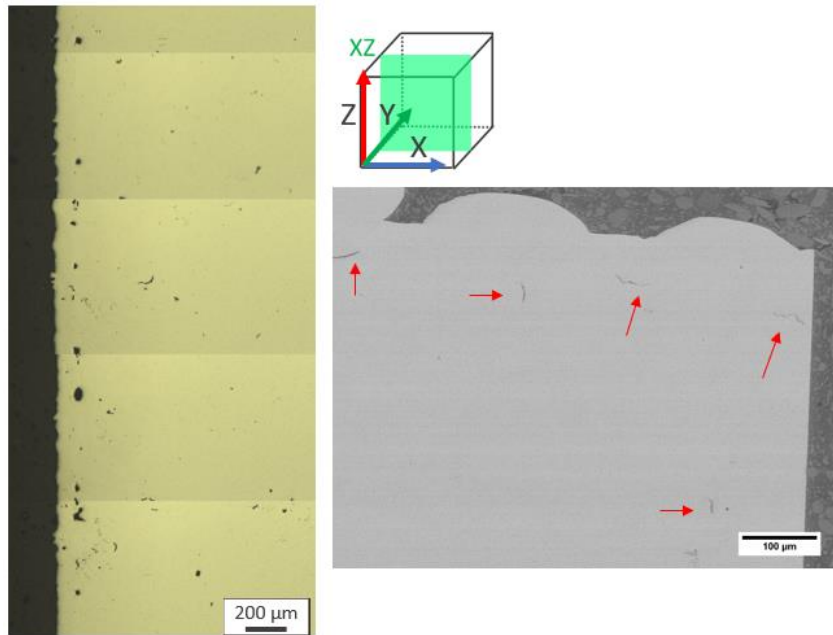
Figure 27. OM micrography highlighting pores (left) SEM micrography of the top surface cross-section. Red arrows highlight micro-cracks.

A quantitative analysis was also performed. Around 22 µm² in each plan were analysed, and only defects with an equivalent diameter higher than 0.7 µm were considered. Statistical results are summed up in Table 14, proving the excellent material health. Sharp defects lead to stress concentration which favors crack initiation; therefore, defects were separated into circular ones (circularity > 0.9) and non-circular ones. The repartition of these defects with the size is plotted in Figure 28. 99 % of circular defects have an average diameter lower than 15 µm, while only 80 % of non-circular pores show this size. Non-circular defects are less abundant but have a higher equivalent diameter.

In conclusion, some classical LPBF defects are detected. However, the high density and the small defect diameter give excellent material health consistent with LPBF literature results.

Table 14. Statistical analysis of defects population.

Average surface density	99.86 ± 0.06 %
Average defect diameter	5 ± 6 µm
Maximum defect diameter	76 µm
Number of circular/non-circular defects	1092/647
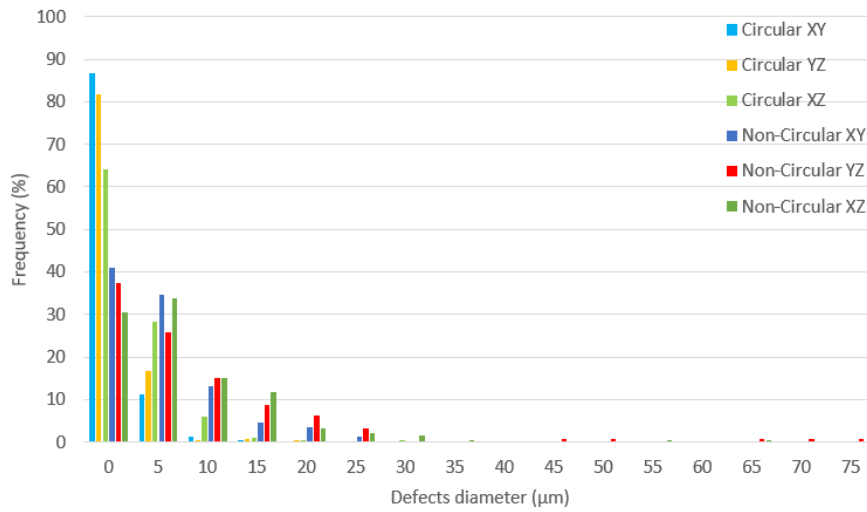
Figure 28. Repartition of defects depending on their size.

Results: macro and microstructure

Samples macrostructure were observed with optical microscopy (Figure 29). Melt pool can be easily distinguished. This macrostructure is typical of the one expected for LPBF samples. The zoom on the top layer differs from the sample's heart. This etching difference proves a difference in the microstructure or composition of this last layer. No specific reason can explain a different composition in the last layer. In contrast, the absence of remelting and subsequent heat-treatment caused by the construction of the upper layer implies a different thermal history of this layer which may lead to a different microstructure.
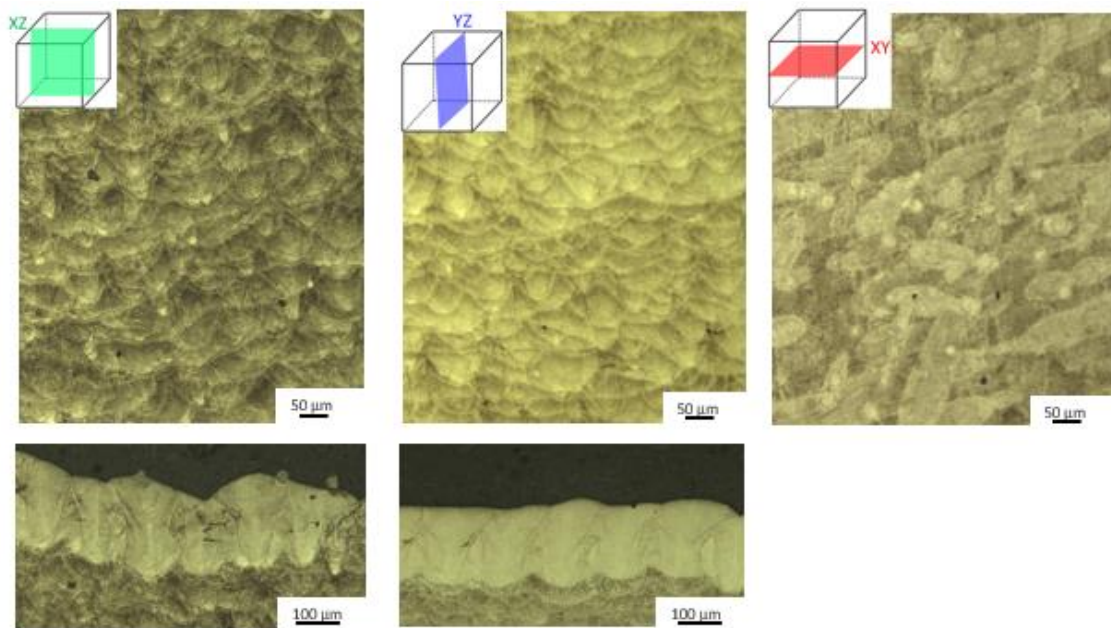
Figure 29. Samples macrostructure with melt pool observations. The bottom images correspond to zoom on the top layer.

From this last layer, melt pool dimensions were measured. Results are presented in Table 15. Melt pools are isotropic, and the large height to width ratio testify to melting keyhole mode [12][13]. The keyhole mode is due to a high energy density and may lead to keyhole porosity [12][13]. Usually, the conduction mode is considered preferable; however, in this specific case, a good material health was noticed; therefore, the keyhole mode has not negative impact on the production.

Table 15. Melt pool dimensions.

|	**XZ plan**	**YZ plan**
Melt pool height	190±20	186±15
Melt pool width	86±9	96±10
Melt pool height / (width/2)	~4.4	~3.9

At higher magnification, the melt pool reveals a cellular microstructure. This microstructure is typical for most LPBF samples. However, LPBF martensitic steel may present either a cellular or needle-like structure. The needle-like structure may be due to an *in situ* heat treatment leading to a more homogenous [10], [14] As shown in Figure 30, cells near melt pool boundaries or near sample edge have no homogeneous size. For a given alloy, cell size is related with cooling rates during solidification. This difference in cells size implies different cooling rates [15]. Cells size average is 0.7±0.3 µm which is in line with values mentioned in the literature for various alloys. These small cell sizes do not allow us to measure the composition gradient implied by cellular structure. But an attentive observation of the cores of cells revealed a needle-like or lathy features, typical of martensitic microstructures.
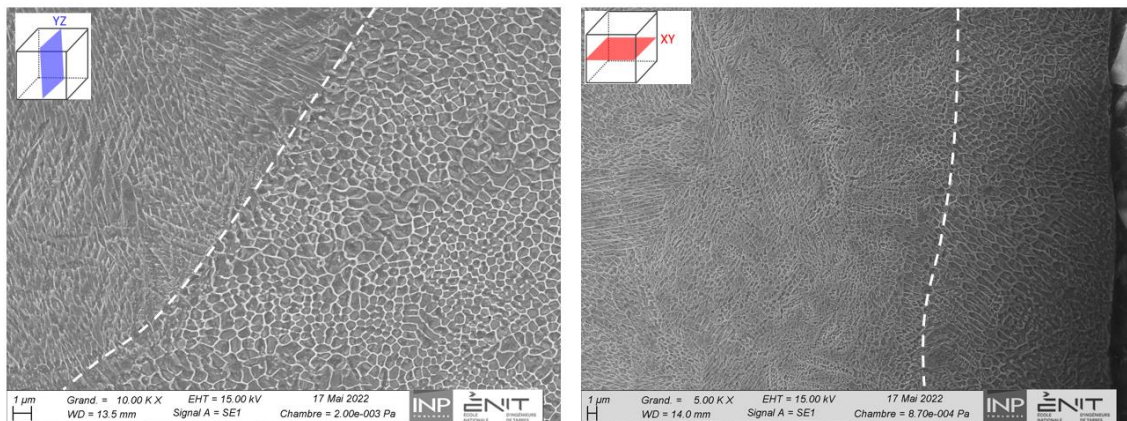
Figure 30. SEM micrography of the cellular microstructure. Dash lines correspond to a microstructure modification at the melt pool boundary (left) or the sample edge (contouring effect, right).

XRD investigated the crystallographic structure of this alloy (Figure 31). W360 is martensitic steel. No remained austenite was detected with this technique. The presence of the double peak for the (110) plan suggests the presence of both the ferrite and martensite phases. A similar pattern was observed for the as-built AISI M50 (with a composition close to W360) [11]. Martensite BCT phase may be transformed *in situ* in ferrite BCC and carbides by thermally heat

affected by upper layers construction. Another hypothesis is the chemical segregation at cells' edges which may lead to a different crystallographic structure, undetermined for now.

Figure 31. XRD spectra. Phase is indexed as BCC.

In conclusion, an excellent material health was measured, and a microstructure consistent with the literature was observed.

Mechanical characterisation

This part will investigate mechanical properties in a room and at high temperatures. Hardness, tensile and impact behavior will be studied.

Methods

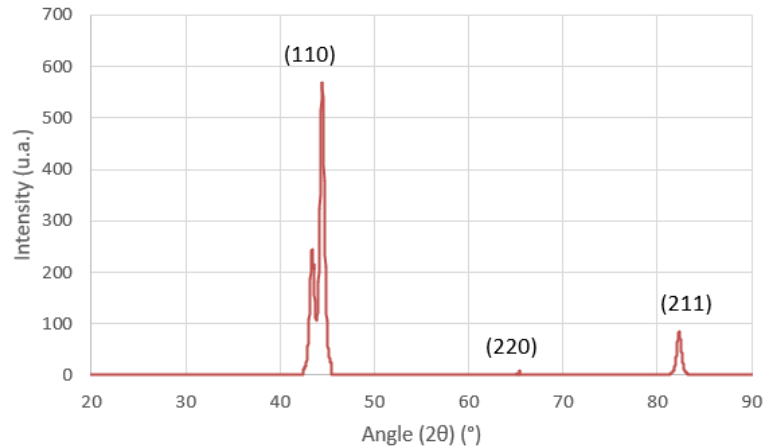Macro and micro Vickers hardness were measured using Zwick/Roell ZHV2.5 equipment with a 10 kg (HV10) and 0.2 kg load (HV0.2). All tests were performed using the EN ISO 6507-1 norm. The bulk global hardness was measured with 30 indents (microhardness), while 300 indents on each plan were recorded for the microhardness. Tensile tests were performed with an electromechanical Instron 5892 tensile machine with a cross-head displacement control mode (2 mm/min leading to an approximative strain rate of 2×10^{-3} s^{-1}) on a dog-bone sample with a gauge length of 35 mm and a cross-section of 5 × 3 mm². Before the tensile tests, samples were polished with P600 SiC paper to remove excessive roughness and to allow a reliable measurement of samples' cross-sections. The strain measurement was carried out with a digital video extensometer. Yield stresses are not easily determined, and the elastoplastic transition was determined using 0.2% proof stress. The Charpy impact test were performed on as-built 2.5 x 10 mm, V-notched samples, using a Zwick HIT 50P with a 50 Joules pendulum.

Results: Hardness

Different hardness measurements were performed, as shown in Table 16. Filiation was performed, and no variation in sample edge or width was noticed. A high macro-hardness value was measured. However, this as-built value is slightly lower than expected after heat treatment (590-630 HV) from the powder supplier [16]. A low anisotropy between vertical and horizontal

plans was measured, indicating an isotropic macroscopic mechanical behavior. An upskin effect explain the higher value measured in the first layer. This first layer was neither remelted nor tempered by thermal reloading. The supplier suggests heat treatment may improve global hardness value.

Table 16. Hardness values.

	XY plan	**XZ plan**	**YZ plan**
Macro-hardness	550±30 HV$_{10}$		
Micro-hardness	678±41 HV$_{0.2}$	648±31 HV$_{0.2}$	644±47 HV$_{0.2}$
Top layer	819 ± 54 HV$_{0.2}$		

Results: Tensile properties

Tensile properties were investigated at room temperature on as-built net-shape samples. Building direction strongly impacts the sample surface, as observed in Figure 32. Horizontally built samples show a surface roughness which is not isotropic: down skin is rougher than upskin. Engineering stress-strain curves were recorded (cf. Figure 32), showing very low ductility. Properties were extracted from the curves and are displayed in Table 17. Contrary to hardness, where a low anisotropy was registered, tensile properties are anisotropic and lower for horizontally built samples. The high surface roughness of these last ones may influence the properties. Even if the yield stress and UTS are high, they are slightly lower than the ones given by Böhler [16]. However, reference values are mentioned for heat-treated samples; therefore, considering the as-built properties, LPBF samples are expected to reach the targeted properties after heat treatment.
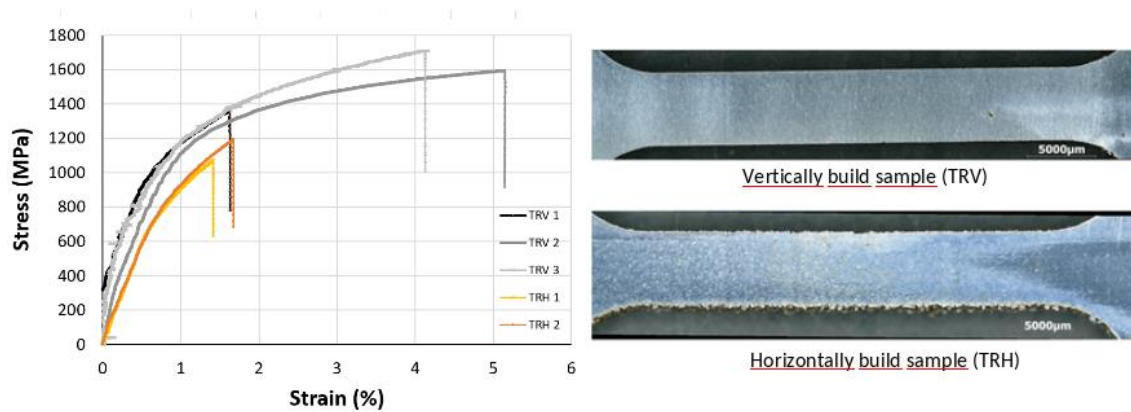
Figure 32. Stress-strain curves of vertically and horizontally built samples (left), picture of tensile test specimens (right).

Table 17. As-built tensile properties extracted from Figure 8 curves. A ca comparison of reachable mechanical properties of the LPBF heat-treated sample promised by Böhler [16] is written.

	YS$_{0.2}$ exp (MPa)	**YS Böhler (MPa)**	**UTS exp (MPa)**	**UTS Böhler (MPa)**	**A% exp**	**A% Böhler**
Vertical	1189 ± 52	1500-1670	1552± 52	1970-2010	2.4±1.6 %	6.6-8.1%

| **Horizontal** | 940 ±61 | | 1140±61 | | 1.5±1.7 % | |

Some tensile tests were also performed at 300 °C on vertically built samples (as-built neither polished/machined nor heat-treated). Tests shows a good reproducibility. It was found a yield stress YS = 1235±54 MPa, an UTS= 1665±2 MPa and an A % = 2.4±0.9 %. Therefore, room temperature mechanical properties are preserved at 300 °C.

Results: Impact properties measured by Charpy impact test.

Impact properties were measured at room temperature on an as-built sample by the Charpy impact test. As for tensile properties, horizontal samples show lower values. It is essential to notice that these need to respect perfectly the theoretical dimensions (some geometrical inaccuracy was detected). Vertical samples almost reached theoretical properties. Therefore, the property is expected to be reached after the heat treatments. SEM images after failure (Figure 33) revealed a brittle behavior and that fracture surface Exhibits features which sizes corresponds to melt pool measured above.

Table 18. As-built resilience values. A comparison reachable resilience of the LPBFat-treated sample promised by Böhler [16]is written.

	Vertical samples	**Horizontal samples**	**HT Böhler [16]**
Sample geometry	ASTM V-notch reduced size 2.5 x 10 mm		ASTM V-notch 10 x 10 mm
Resilience (J/mm²)	9.52 ± 1.08 J/cm^2	7.79 ± 1.06 J/cm^2	10-17 J/cm^2

Horizontal samples   Vertical samples
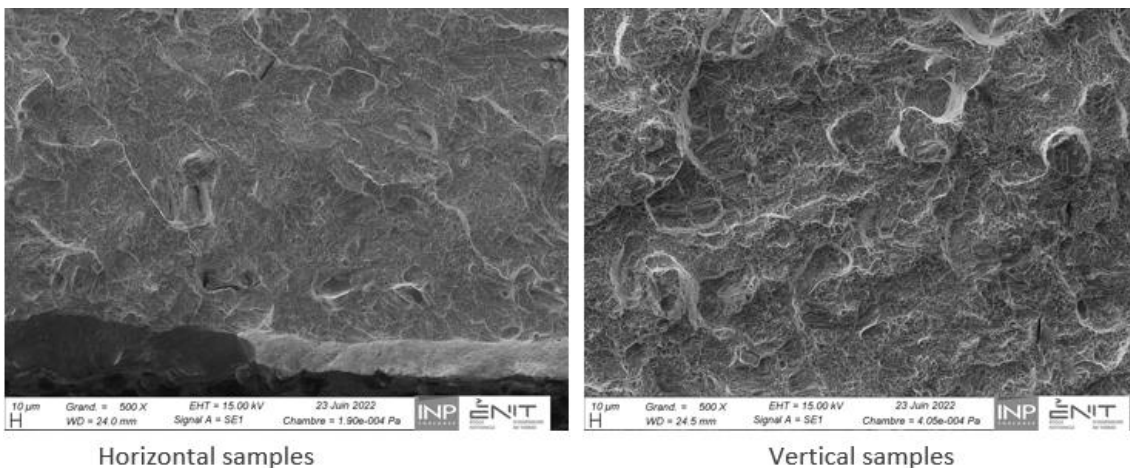
Figure 33. SEM observation after failure.

Heat treatment study

In this part, the influence of the production process on the heat treatments will be investigated by differential thermal analysis and dilatometry. CCT will be established and compared with the one given by Böhler for conventional W360.

Methods

Phase transformations were studied to investigate the influence of initial microstructure (LBPF) compared to conventional material on heat treatment. A continuous cooling transformation diagram was drawn by dilatometry. These experiments were carried out on a DIL L78 Q machine (Linseis) on 4 mm diameter, 10 mm long cylinders. Before the measurement, the furnace atmosphere was twice brought to vacuum until 2×10^{-2} mbar and then filled with Argon. The temperature was controlled using a type K thermocouple welded on the sample. The heating ramp were formed at 15°C/min, and samples were homogenized at 1050 °C for 30 min, then cooled down at different cooling rates (from 0.7 to 360 °C/min). In addition, differential thermal analysis (DTA) measurements were performed with an equal heating and cooling rate (5 °C and 15 °C, holding 1050 °C for 30min) under a 40 ml/min flow of argon on around 80 mg samples.

Results: Dilatometry

During dilatometry measurement, the length variation is recorded (blue curve). An example of the result (heating segment) is displayed in Figure 34. Phase transformation appears as a wave on the curve, while others transformations correspond to slope modification. To detect them, the derivative can be used (orange curve). When heating the martensite phase, η-Fe_2C carbides may appear between 100 and 200 °C, ε-Fe_2C may appear alone until 250 °C then together with θ-Fe_3C (cementite), and above 450 °C only θ-Fe_3C persist. Higher temperature precipitation corresponds to non-iron carbides [17]–[20]. Curie temperature can also be measured by dilatometry [21]. Those transformations are also caught in our measurement (Figure 34).
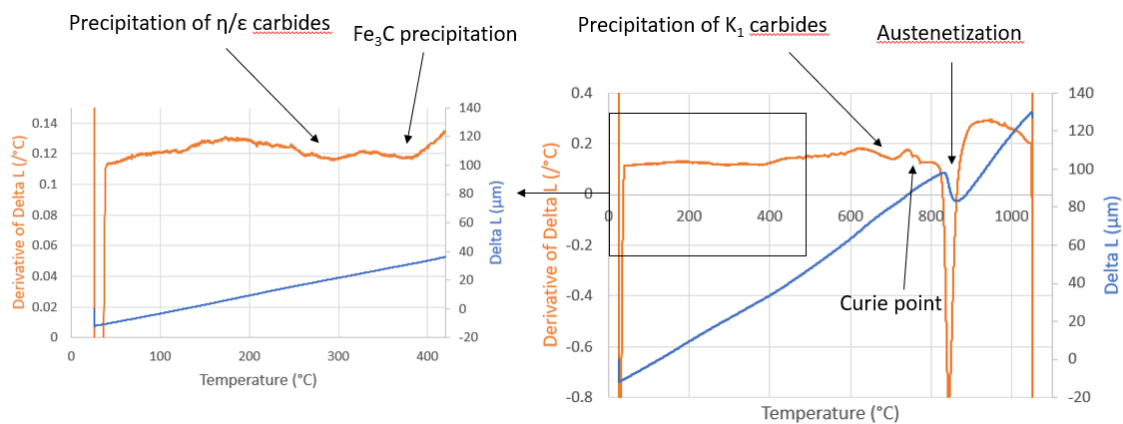

Figure 34. Example of dilatometry curve analysis on the heating segment..

During cooling segments, several phase transformations were noticed depending on cooling rates. Curves with phase transformations and associated micrography are displayed in Figure 72.
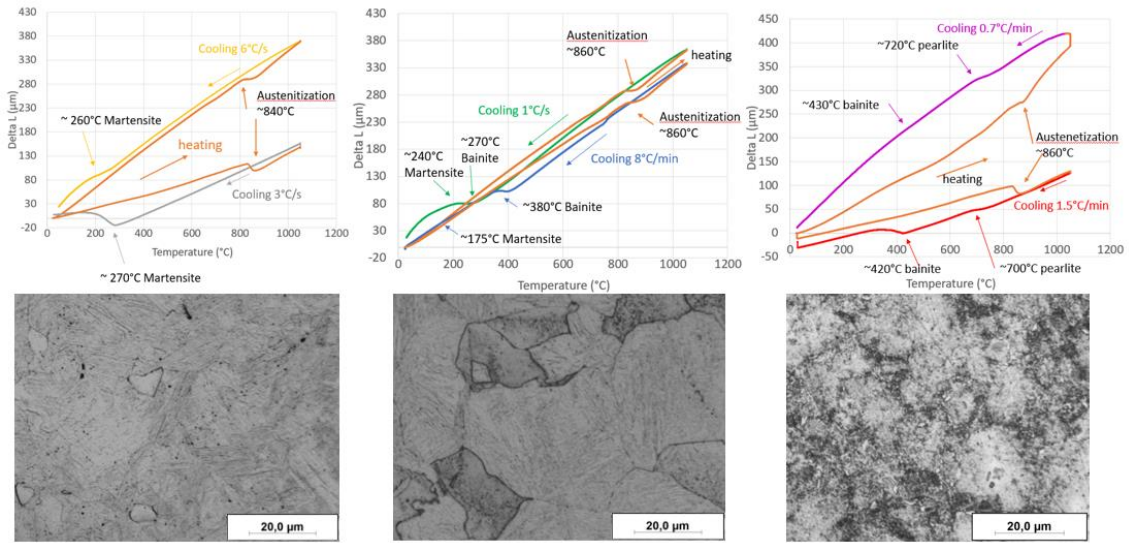
Figure 35. Dilatometry curves for different cooling rates and their associate micrographies.

From these curves, a modified CCT diagram is drawn and compared to the one furnished by Böhler for conventional materials (Figure 36). For each cooling rate hardness was measured and compared to Böhler data (for conventional wrought material) in Table 32. The austenitization step of LPBF samples was performed in the condition indicated by the Böhler CCT diagram. LPBF samples show phase transformations shift to the left (higher cooling rates) compared to conventional material. This may be explained by the homogenization on step not adapted to LPBF samples (cellular structure) and/or by the slight composition difference. Martensitic samples show a lower hardness compare to conventional ones. For other cooling rates hardness is also lower, but the difference in phase presence of phases proportion may explain it.
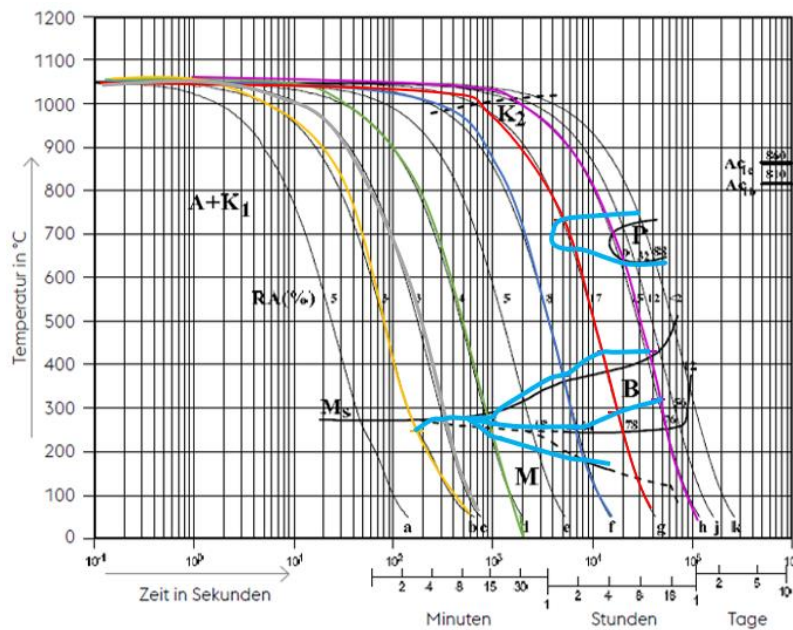

Figure 36. CCT diagram. Black lines: Böhler data [22], coloured lines: experimental measurements

Table 19. Harness values for different cooling rates.

	Hardness (HV5) Experimental data	Hardness (HV10) Böhler data [22]
360°C/min (6°C/s)	703 ±16 HV	750 HV
180°C/min (3°C/s)	676 ± 4 HV	750 HV
60°C/min (1°C/s)	645 ± 24 HV	740 HV
8°C/min	492 ± 12 HV	580 HV
1.5°C/min	348 ± 20 HV	500 HV
0.67°C/min	212 ± 8 HV	450 HV

Results: Differential thermal analysis (DTA)

From the temperature difference between a sample and reference (air), heat flow can be calculated by DTA during heating and cooling. Various phase transformations were recorded, as described in Figure 37.
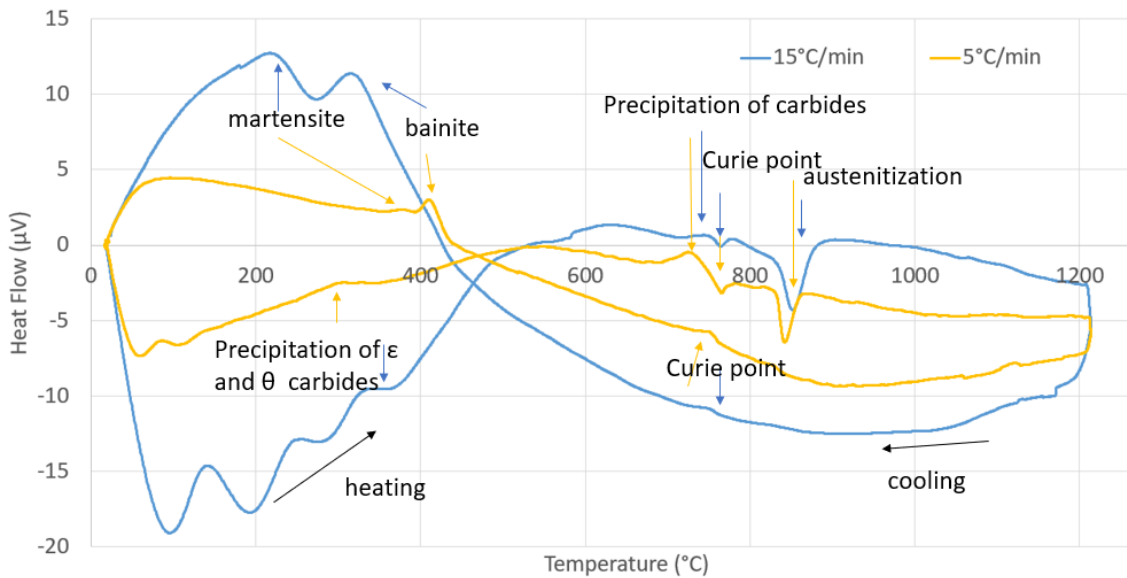

Figure 37. DTA curves for two different heating/cooling rates

Results: Comparison of both methods

Phase transformations measured by DTA and dilatometry (15 °C/min) during heating were compared. Similar methods were applied for cooling with DTA (5 and 15 °C/min) and dilatometry (8 °C/min). Results are given in Table 20 and are compared with theoretical ones from the literature [17]–[20] for heating and the CCT diagram for cooling [22]. Even if the same transformations were detected for both methods, dilatometry makes cooling transformation temperature more accurate. Considering heating phase transformation temperature, DTA curves show some noise for low temperature (under 250 °C), corresponding to troubles of following the targeted temperature. For higher temperatures, the standard deviation is smaller than dilatometry ones. Therefore, DTA seems here more accurate. In conclusion, both methods are consistent with each other's values and the reference's values.

Table 20. Comparison of phase transformations measured by DTA and dilatometry with references (literature for heating, CCT diagram for cooling).

Transformation	DTA	Dilatometry	References
Precipitation of η/ε carbides (heating)	noise	282 ± 17°C	100-250°C
Decomposition of residual austenite (heating)	/	/	~280°C
Precipitation of θ carbides (Fe$_3$C) (heating)	313 ± 17°C	419 ± 53°C	250-450°C
Precipitation of K$_1$ carbides (heating)	729 ± 1°C	704 ± 6°C	?
Curie point (heating)	766 ± 2°C	760 ± 11°C	~750-760°C
Austenitisation (heating)	842 ± 9°C	846 ± 7°C	835±25°C
Curie point (cooling)	756 ± 4°C	758°C	~750-760°C
Pearlite (cooling)	/	/	X
Bainite (cooling)	400 ± 35°C	382	~370°C
Martensite (cooling)	325 ± 86°C	175	180°C

Conclusion and perspectives

W360 was produced by the LPBF method, and as-built net-shape samples were analysed. Excellent materials health was measured with a very high density (>99.8 %). Some defects, such as cracks, and pores, are linked to the contouring strategy and upskin effect and will be removed during the machining of the final part. A cellular microstructure was observed with very thin cells (around 0.7µm). This submicronic microstructure should be investigated by TEM in the future to get more detail, specifically on elements segregations. Concerning the as-built net-shape mechanical properties, tensile and impact properties are already high. They are not reaching the machined heat-treated expectation but are very promising. In the future mechanical properties of heat-treated samples should be investigated. Finally, heat-treatment possibilities were explored by DTA and dilatometry. A modified CCT diagram was established, and the transformation domains appears shifted to higher cooling rate. Therefore, standard heat treatment (for conventional materials) seems inappropriate for LPBF materials. And specifically, in the future study a focus on the homogenization step should be done: the initial cellular microstructure may need a higher temperature or longer step to disappear.

Pilot SP1-MEUPE/INESPASA

During the development of this pilot, 2 different aluminium alloy have been studied: AlSi10Mg and Scalmalloy ®.

Raw material characterization

No characterization on the raw materials (powder) have been considered on this pilot, as the main objective was to characterize electrical and thermal properties of both material (AlSi10Mg and Scalmalloy ®) once that they are melted (solid). The information delivered by the powder
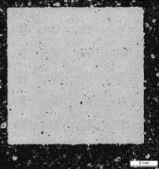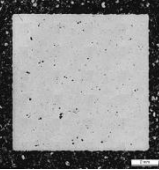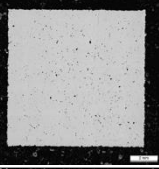
supplier was considered as baseline (flowability, particles size distribution, …). Scalmalloy ® powder was supplied by TOYAL and AlSi10Mg from LPW.

Microstructural characterisation

In this part, the microstructure analyses of two aluminum alloys, AlSi10Mg and Scalmalloy, manufactured by LPBF will be presented.

All the AlSi10Mg samples presented low porosity content (less than 0.5 %). This same result was obtained for the first DoE of Scalmalloy. However, after carrying out a second DoE with optimized process parameters, the porosity content of Scalmalloy was reduced to values close to 0.1 %. Table 21.

Table 21. Porosity fraction in both alloys AlSi10Mg and Scalmalloy

	Material	Heat treatment	Porosity (%)	Hardness (HV 0.2)
	AlSi10Mg	No	0.43	
	AlSi10Mg	325 °C /4h	0.39	
	Scalmalloy DoE 1	No	0.34	
		325 °C /4h	0,56	
	Scalmalloy DoE 2	No	0.13	113
		325 °C /4h	0.10	173
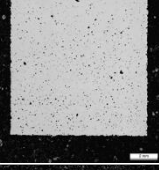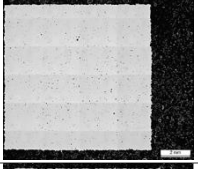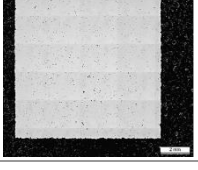
A microstructural study of each material has been carried out in as-LPBF and heat-treated samples. The dendritic (cellular) structure of as-LPBF AlSi10Mg collapses after the heat

treatment and forms equiaxed particles, larger in size and with a spherical morphology, Figure 38. This change is usually motivated by the formation of Mg_2Si phases [23].
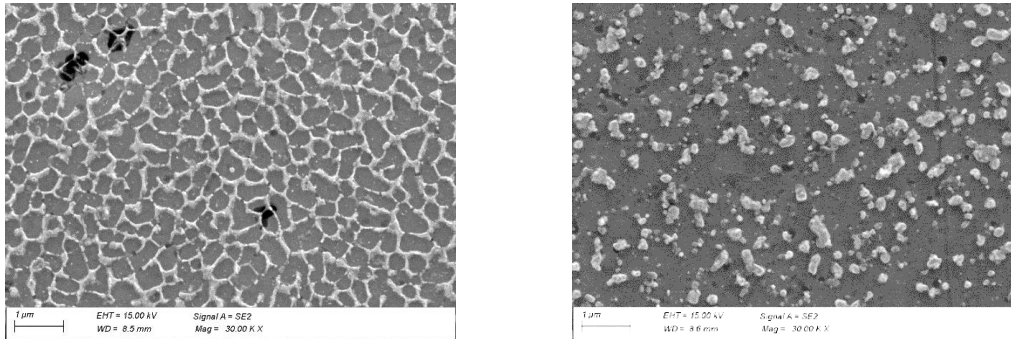
Figure 38. FEG-SEM microstructures of ALSi10Mg as-LPBF (left) and heat-treated (right)

As-LPBF Scalmalloy shows a very fine and homogeneous microstructure, Figure 39. As-LPBF Scalmalloy have a super fine grain structure including ultrafine equiaxed grains as well as more refined columnar grains compared to other aluminium alloys [24]. Scalmalloy shows FCC crystal structure as seen in the X-Ray diffractome, Figure 40.

After heat treatment, Mg, Sc and Zr enriched precipitates are formed on the edges and inside the grains, Figure 39 and Figure 40. Other authors also found nano-size Al_3Sc and Al_3Sc precipitates after heat treatment in Scalmalloy [24].
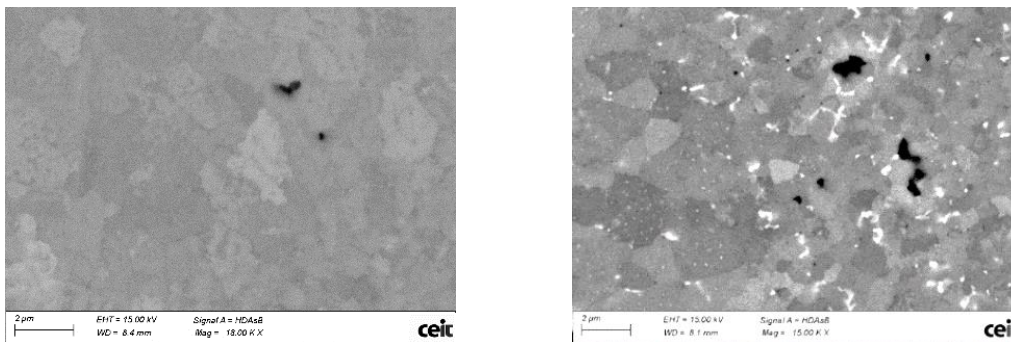
Figure 39. FEG-SEM microstructures of Scalmalloy as-LPBF (left) and heat-treated (right)
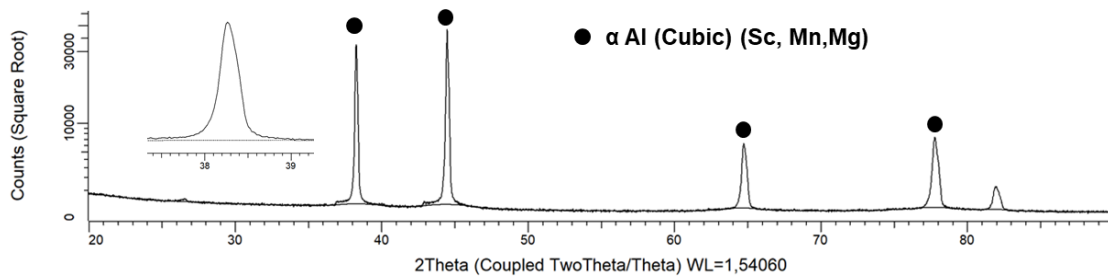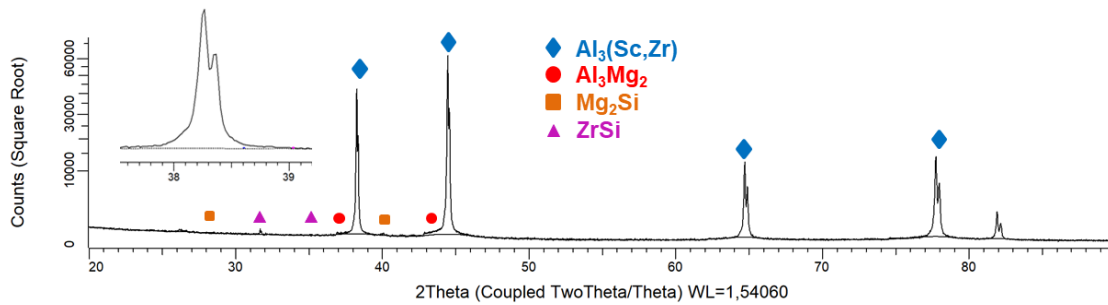
Figure 40. X-Ray diffractogram of Scalmalloy as-LPBF (up) and heat treated (bottom)

The metallurgical structure is bimodal or duplex, consisting of regions of very fine grains located at the edges of the melts and their bases, Figure 41 and Figure 42. This bimodal structure is a characteristic of aluminum alloys whose chemistry has been modified by the addition of Sc or Zr elements [25], [26], [35], [27]–[34]. The very fine grains have a rather equiaxed geometry and are sub-micrometer in size. The coarser grains are columnar. In fact, in an XZ section, they are elongated in the direction of manufacture, and in an XY section, they have an equiaxed cross-section with a diameter of the order of a micrometer. As the grains are very small, the EBSD analysis did not allow a total indexation of the structure, especially in the zones where the grains are the finest.
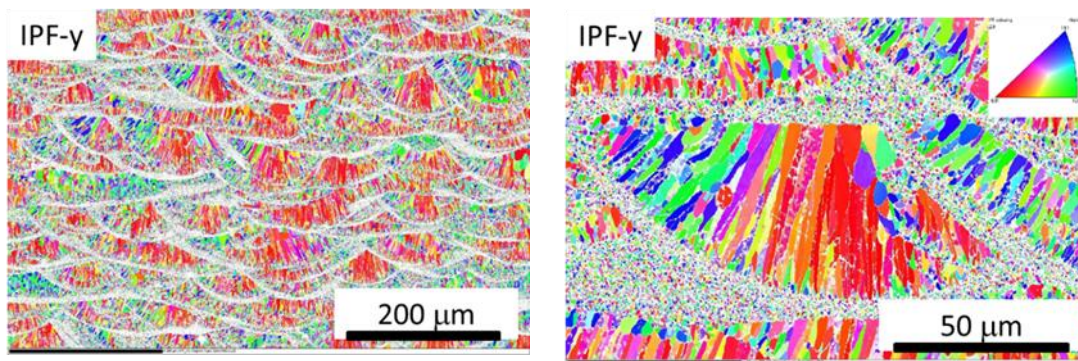
Figure 41. EBSD analysis of Scalmalloy manufactured with LPBF untreated.
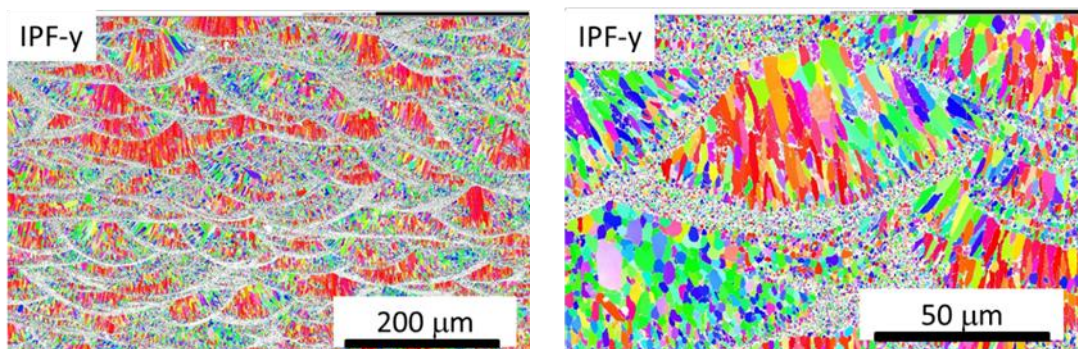
Figure 42. EBSD analysis of Scalmalloy manufactured with LPBF and heat treated.

Mechanical characterisation

Micro-hardness tests (HV0.1) were carried out on both treated and untreated AlSi10Mg and Scalmalloy alloys. In the untreated state, the AlSi10Mg alloy has a higher hardness partly due to

its cellular network. In the untreated state, the processed material has an excellent cell structure consisting of aluminum cells surrounded by a silicon-rich eutectic. The solid solution is supersaturated with Si. However, after heat treatment, Scalmalloy (Al-Mg-Mn-Sc-Zr) is much harder due to the formation of the hardening precipitate.
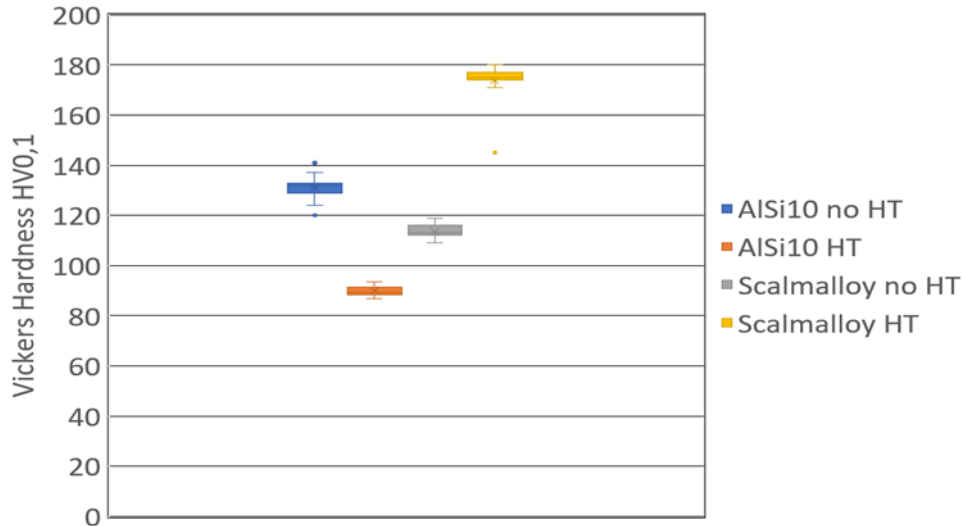
Figure 43. Average hardness values obtained for AlSi10Mg and Scalmalloy.

Electrical and thermal conductivity analyses

➢ *Electrical Conductivity*

The test method has been adapted from the following standard IEC 468 (1974) "Method for measuring the resistivity of metallic materials". The measurements were carried out at a temperature of 20 °C ± 2 °C, 50±10 % RH. The measurement method is the 4-wires method.
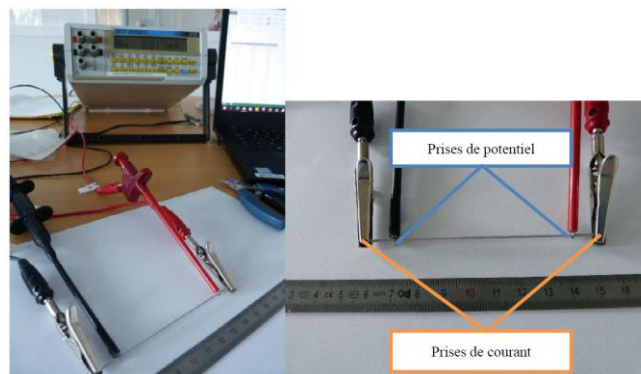
Figure 44. Measurement of the resistance of the test piece by the 4-wire method.

The diameter of the specimens was measured at 12 points along their length to calculate their average cross-section. However, due to the roughness of the material and the measurement method, the measured values correspond to a "peak to peak" measurement of the diameter. As a result, the cross-section of the specimens is undoubtedly overestimated. This overestimation of the cross-section will mathematically lead to an overestimation of the resistivity and an underestimation of the conductivity.

The diameters were measured for the different specimens. Table 22 present the results for the AlSi10Mg Heat treated samples.

Table 22. Diameters of the samples AlSi10Mg Heat treated.

Number	Sample	Sample	Sample
1	1.086	1.096	1.08
2	1.13	1.102	1.126
3	1.065	1.162	1.165
4	1.127	1.143	1.122
5	1.079	1.11	1.121
6	1.157	1.135	1.187
7	1.168	1.109	1.127
8	1.094	1.164	1.105
9	1.109	1.08	1.127
10	1.194	1.174	1.113
11	1.104	1.104	1.162
12	1.048	1.038	1.119
Average	1.11	1.12	1.13
Median	1.11	1.11	1.12
Standard	0.04	0.04	0.03

The electrical resistance of each specimen is measured by the 4-wire method. A fixed current (1A) is passed through the specimen, and the potential difference generated is measured between two points on the specimen, remote from the current sockets. The measurement is carried out using an AOIP OM 21 micro-ohmmeter. The measuring equipment automatically calculates the resistance.

The current is applied in alternating mode: the direction of the current is alternated, and the value measured is the average resistance for the two directions of current flow. This makes avoiding parasitic currents (thermoelectric currents, etc.) possible. The current is sent in pulsed mode to limit the heating of the test piece. The distance between the two potential taps is measured with a ruler.

$$\rho = R \times \frac{S}{l}$$

P: resistivity [Ω.m]
R: measured resistance [Ω]
S: cross-sectional area of the test piece [m²].
l: standard length [m].

The results of electrical resistance measurements by the 4-wire method on the four material references are given in the following Table 23. The electrical conductivity of materials is shown in Table 24.

Table 23. The working distance between the electrodes and measured resistance values

	sample	Standard length (distance between the potential taps) (mm)	Measured resistance (mΩ)
Sample AlSi10Mg heat treated	1	85.5	4.805
	2	79	4.420
	3	78	4.301
Sample AlSi10Mg	1	80	5.99
	2	74.5	5.659
	3	74	5.620
Sample Scalmalloy Heat treated	1	78	7.423
	2	71.5	6.917
	3	71.5	6.866
Sample Scalmalloy	1	78	9.27
	2	71.5	8.47
	3	71	8.402

Table 24. Resistivity and conductivity values of AlSi10Mg alloy and scalmalloy

	Sample	Resistivity (Ohm.m)	Conductivity (S.cm-1)
Sample AlSi10Mg Heat treated	1	$5{,}47.10^{-8}$	$1{,}83.10^{5}$
	2	$5{,}49.10^{-8}$	$1{,}82.10^{5}$
	3	$5{,}53.10^{-8}$	$1{,}81.10^{5}$
	average	$\mathbf{5{,}5.10^{-8}}$	$\mathbf{1{,}82.10^{5}}$
Sample AlSi10Mg	1	$7{,}13.10^{-8}$	$1{,}40.10^{5}$
	2	$7{,}37.10^{-8}$	$1{,}36.10^{5}$
	3	$7{,}24.10^{-8}$	$1{,}38.10^{5}$
	average	$\mathbf{7{,}3.10^{-8}}$	$\mathbf{1{,}38.10^{5}}$
Sample Scalmalloy Heat treated	1	$9{,}73.10^{-8}$	$1{,}03.10^{5}$
	2	$1{,}00.10^{-8}$	$1{,}00.10^{5}$
	3	$9{,}87.10^{-8}$	$1{,}01.10^{5}$
	average	$\mathbf{9{,}9.10^{-8}}$	$\mathbf{1{,}01.10^{5}}$
Sample Scalmalloy	1	$12{,}1.10^{-8}$	$0{,}83.10^{5}$
	2	$12{,}1.10^{-8}$	$0{,}83.10^{5}$
	3	$12{,}1.10^{-8}$	$0{,}83.10^{5}$
	average	$\mathbf{12{,}1.10^{-8}}$	$\mathbf{0{,}83.10^{5}}$

> *Thermal Conductivity*

The thermal conductivity analyses of AlSi10Mg and Scalmalloy carried out between room temperature and 200 °C are shown in Figure 45. The conductivity of both aluminium alloys increases after the heat treatment. In the case of AlSi10Mg the conductivity (K) is constant but the K of Scalmalloy increases linearly with the temperature. Rapid solidification in AM processes produce a nanosized cellular structure and a supersaturated lattice that give a very low thermal diffusivity and thermal conductivity, but when heat treating a large quantity of microstructural features (i.e. Sc and Zr rich precipitates) reduce the heat transfer properties of AM produced samples [36]. Comparing both aluminium alloys can be observed that AlSi10Mg has higher conductivity than Scalmalloy and this has been related the more homogeneous microstructure of AlSi10Mg due to a lower number of alloying elements.
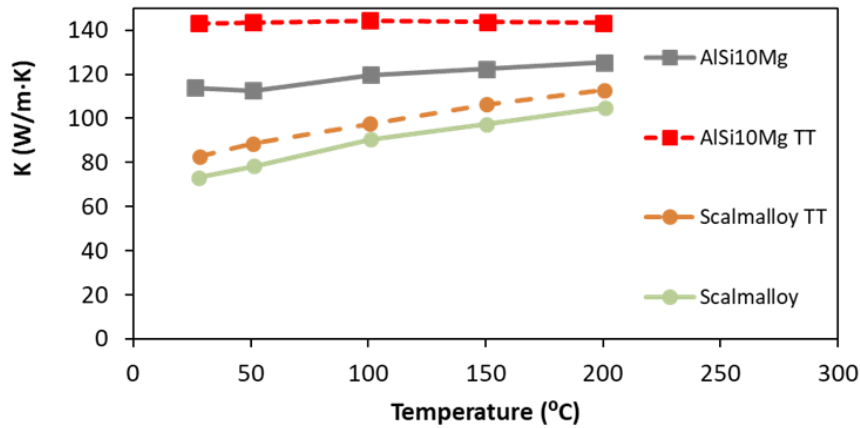
Figure 45. Thermal conductivity for as-LPBF and Heat treated AlSi10Mg and Scalmalloy.

The effect of manufacturing orientation on thermal properties with analysed. In Figure 46 can be seen that the conductivity is isotropic as it remains constant regardless of the build direction (Z or XY).
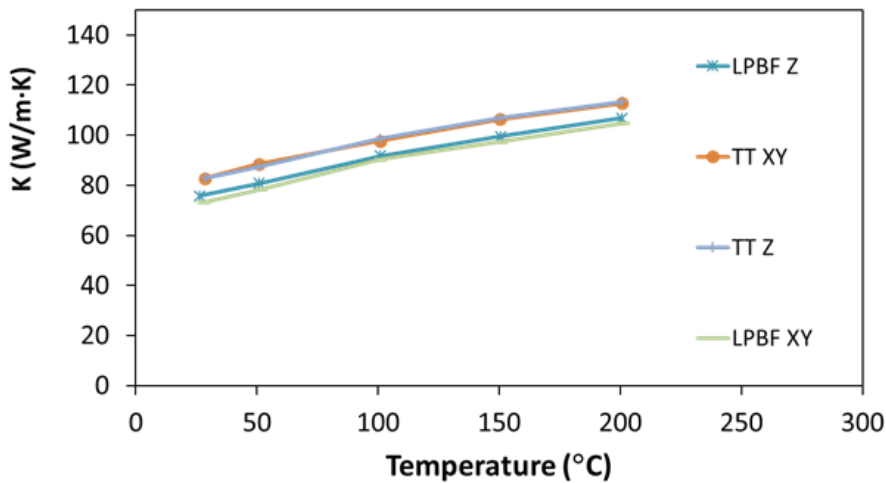
Figure 46. Thermal conductivity for as-LPBF and Heat treated Scalmalloy in the two manufacturing orientations, build direction (Z) and perpendicular to build direction (XY).

Finally, the effect of porosity in the material has been analysed, Figure 47. Samples with less porosity (DoE2) show higher conductivity due to lower dispersion centres and therefore higher heat transference.
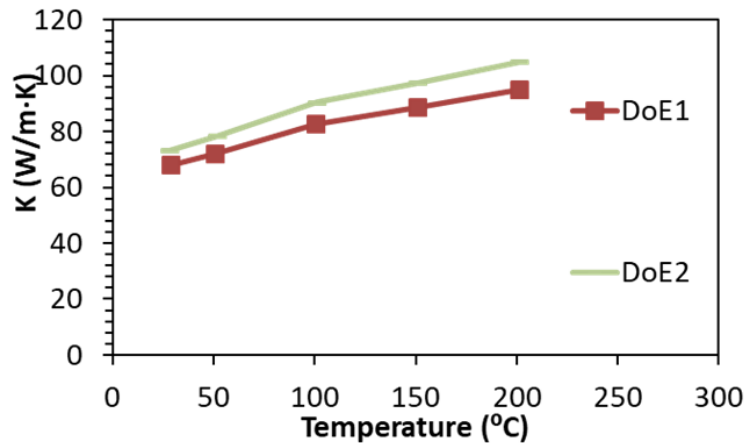
Figure 47. Thermal conductivity results for Scalmalloy samples from two batches, DoE 1 with elevate porosity and DoE 2 with low porosity.

Mechanical characterisation

Several build jobs have been manufactured in order to obtain enough coupons to characterize mechanically both materials (Figure 48). To analyse the influence of surface roughness, machined and as-build coupons have been considered. Also, coupons to study the influence a thermal treatment have been taken into account.
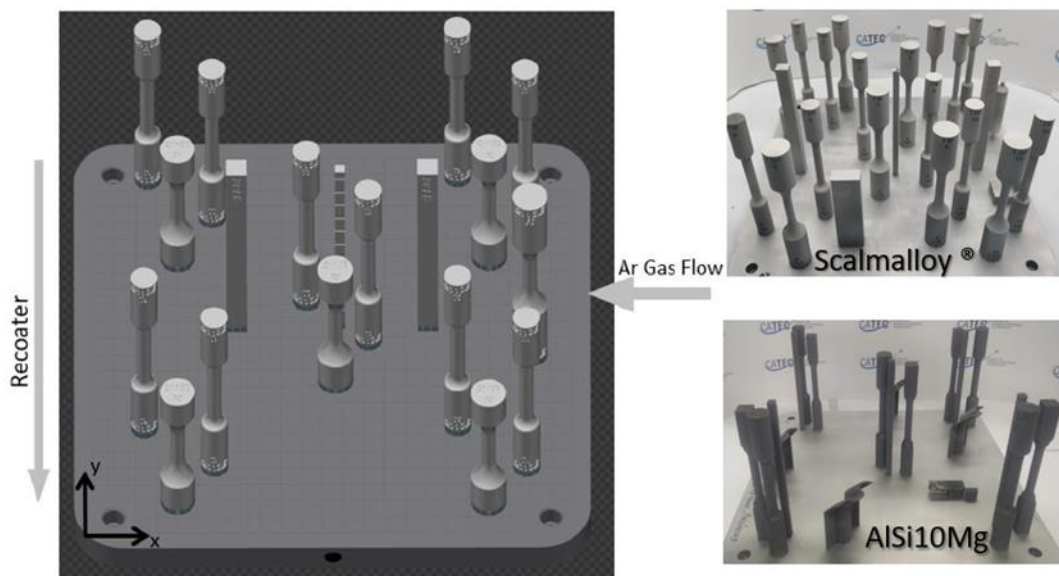
Figure 48. (left) Schematic view of a generic tensile and fatigue coupons, (right top) image of Scalmalloy ® and (right bottom) AlSi10Mg build jobs

Figure 49 shows the results of mechanical test performed in the AlSi10Mg coupons. Finally, 20 different sample have been analysed: as-build with HT (x5), as-built without HT (x5), machined with HT (x5) and machined without HT (x5). It can be observed below that the heat treatment increases the elongation but reducing the strength. With regards the surface condition, machining coupons produce a slight increase in the properties when comparing with the sand blasted samples.
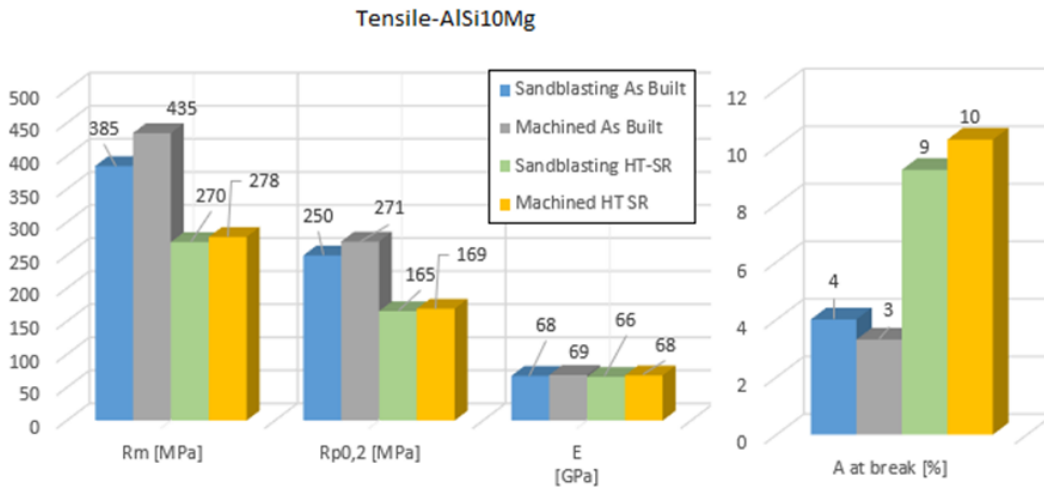
Figure 49. Mechanical properties of AlSi10Mg with and without heat treatment

Regarding the Scalmalloy® coupons (Figure 50) only heat treatment samples have been tested, since preliminary studies has demonstrated better results in terms of hardness when this material is heat treated. It can be observed below when comparing both surface conditions (sand blasting and machining), that the roughness has a slight influence on the properties, decreasing them.
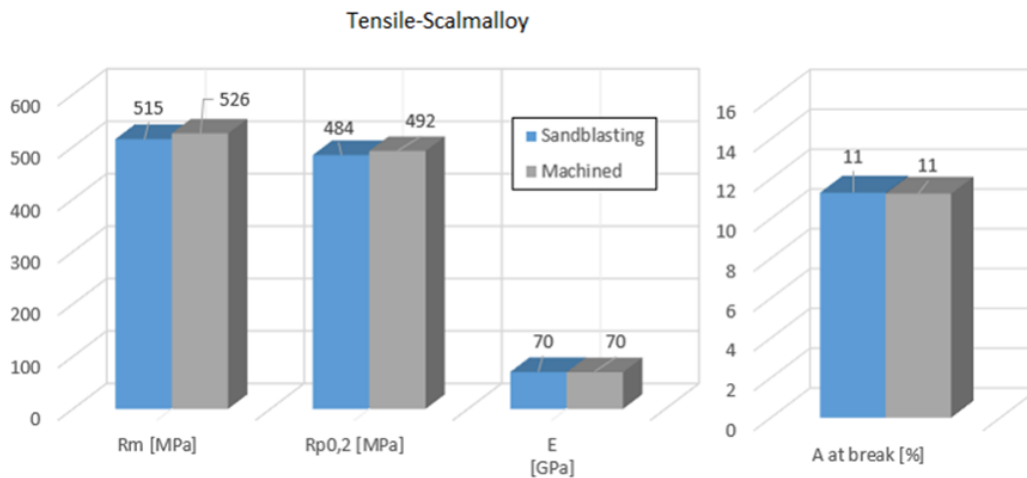
Figure 50. Mechanical properties of Scalmalloy® with heat treatment

Additionally, dynamic behaviour (fatigue) of Scalmalloy® was also analysed, since this material was detected as better approach for this pilot (lower thermal conductivity, better static properties…). Figure 51 shows the fatigue curve of this materials, considering sand blasting and machining samples. It can be observed no big differences between both surface condition and low dispersion in the results, excluding the results obtained for 220 MPa.
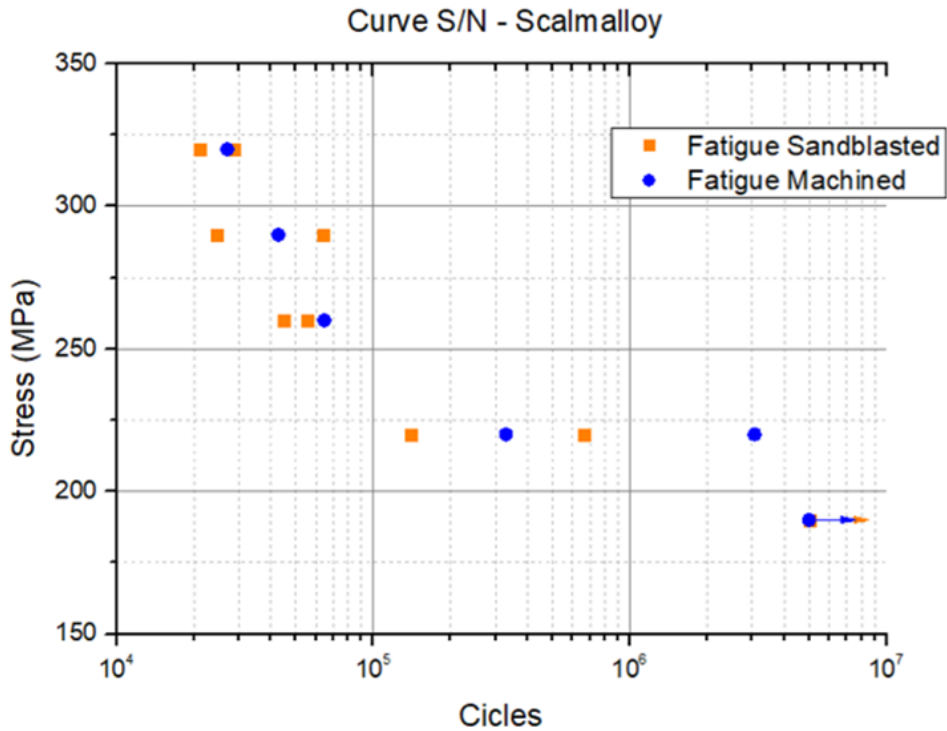
Figure 51. Fatigue curve of Scalmalloy® with heat treatment (machined and sandblasting)

Thermal simulation and experimental test on coupons

The UPV/EHU together with FADA CATEC have performed the thermal simulations of the proposed geometry. In order to ensure the validity of the results, as an initial step the thermal behaviour and the heat dissipation capacity of the different geometries have been evaluated experimentally and the results have been employed for defining the convective coefficient of the different surfaces.
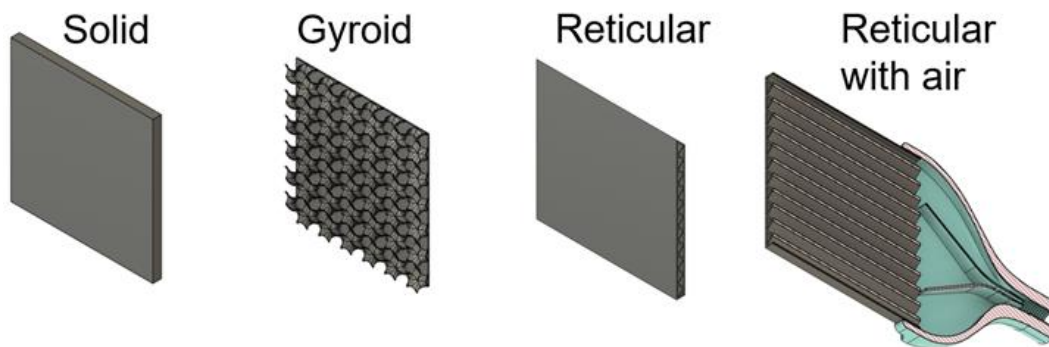
Figure 52. 3D views of the studied geometries.

As shown in Figure 53 the temperature of each component is measured using a thermal camera. The component is heated from the back by means of radiation coming from a lamp and the time required to reach an 85ºC temperature is measured, as well as its posterior cooling.
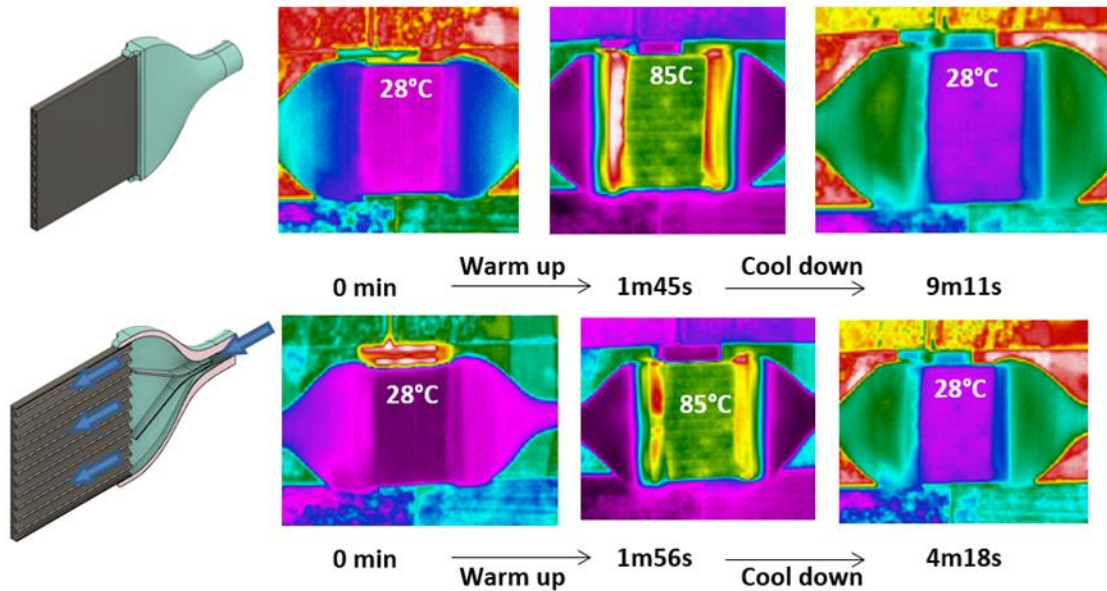
Figure 53. Experimental thermal fields during the heating and cooling cycle.

The simulations are run using the software Ansys Workbench 2021-R2 and the transient thermal module is employed in all cases. The heat introduced via radiation from the lamp is defined as a constant input for all situations (3, 200 W/m^2) and the convection coefficient for the heat dissipation is determined based on the experimental tests. The obtained convection coefficients are summarized in Figure 54 and the comparison between the simulated and experimental results is shown in Figure 55.

Situation	Convection coefficient [W·m^{-2}K^{-1}]
External natural	10
External Gyroid	4
Internal natural	1
Internal Forced	100

Figure 54. Convection coefficients employed in the simulations.
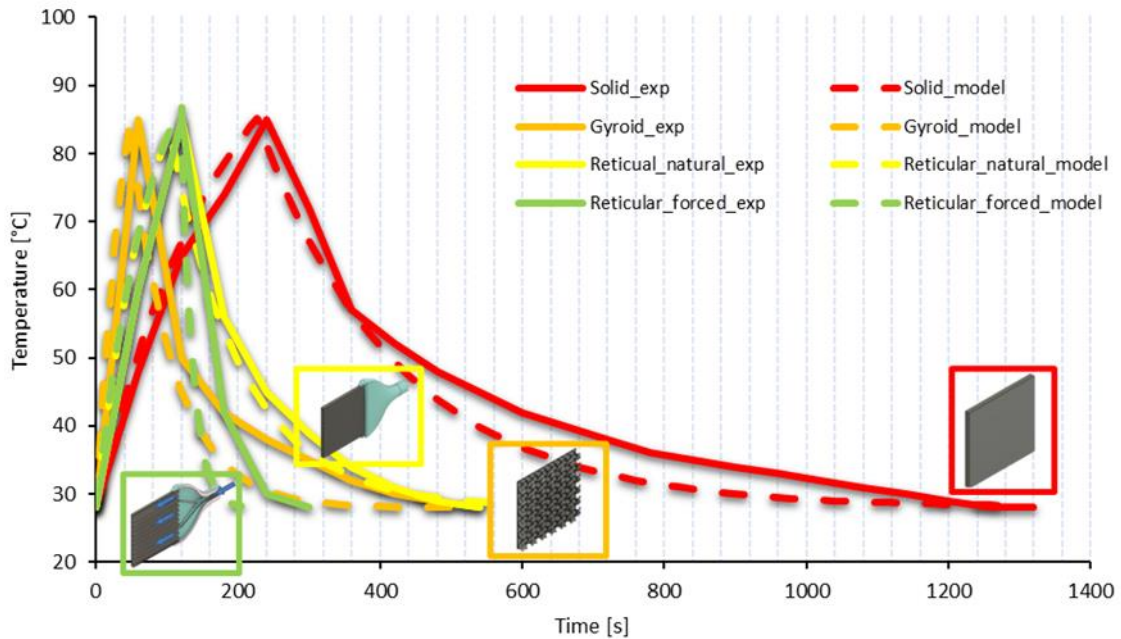
Figure 55. Comparison between experimental and simulation behaviour of the components.

Conclusion and perspectives

- Scalmalloy® seems to be the best approach for the functionality of this pilot at it has better mechanical properties but also, at it has lower thermal conductivity, the heat produce by the motors inside the case has more difficulties to reach the surface and burn the operator.
- In both materials, AlSi10Mg has higher thermal and electrical conductivity. Moreover, in the case of thermal conductivity, the presence of porosity reduces the heat transfer.
- Tests on coupons have shown a good match between thermal simulation and experimental tests. This procedure will be evaluated and taken into account when redesigning the final AM case. A thermal simulated analysis will be performed in order to validate the procedure.

Pilot FR2-SOMOCAP

Raw material characterization

First, polymer-metal wires were analysed.

Methods

The filament samples provided by Markforged were subjected to the same polishing procedure as the as-sintered samples. However, due to the small size of metal powder particles in filaments, an additional step of polishing with a colloidal solution containing silica particles of 0.25 μm (OPS) was added to the process. The 12 optical images of the filament samples were acquired randomly using a PMG3 optical microscope from Olympus at x20 magnification and were captured using the Archimed software. These images were then treated with an open-source image processing software called ImageJ [1] to determine the size and surface ratio of the metal particles that are bound with the polymer. The images captured comprise a total area of 1.55 mm² that was analysed, and only metal particles with a minimum diameter of 0.2 μm were considered during the image processing.

Results

The metal powders in the 17-4 PH and H13 filaments were spherical, with an average roundness of 0.79 ± 0.26. The 17-4 PH filament had relatively smaller metal particles with an average diameter of 3.6 μm compared to the H13 filament, which was around 4.6 μm. Metal powders can be seen in Figure 48 and Figure 49 as grey particles, whereas polymer matrix can be seen in black. It is essential to approach the interpretation of metal particle size results cautiously since the metallographic section preparation technique may not completely represent the particle shape. This limitation can hinder the ability to conduct a thorough analysis of the metallic charge. Although removing the matrix through chemical or thermal debinding could be beneficial, it was not feasible to perform this procedure safely using available laboratory equipment.
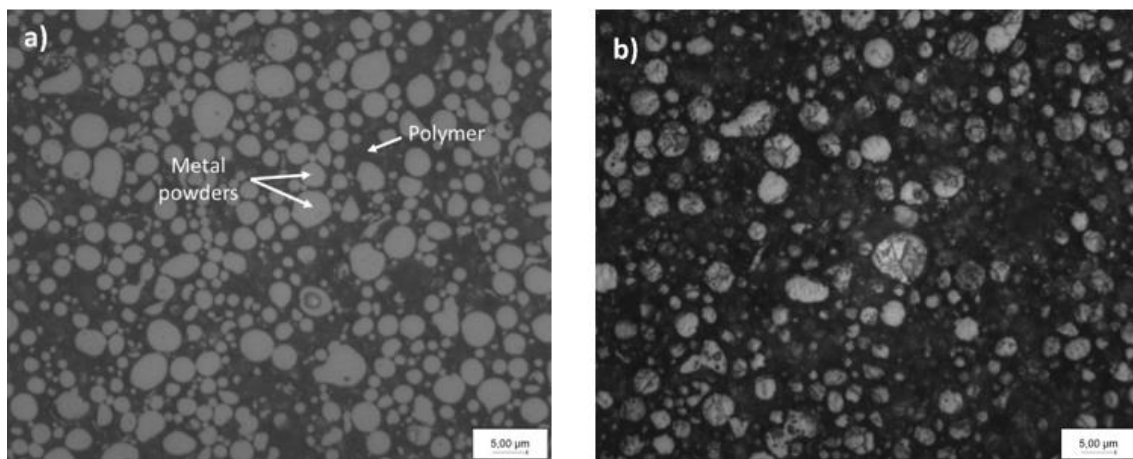
Figure 48. Optical micrographs of 17-4 PH metal-polymer filament a) before etching b) revealing microstructure

Furthermore, the metal-to-polymer powder ratio was higher in H13 filaments (46.2 ± 0.7 %) than in 17-4 PH filaments (41.2 ± 0.7 %) from optical image processing. As both sheets of steel, 17-4 PH and H13, are martensitic steels, the metal particles in the filament samples exhibited a microstructure similar to martensite after etching, presented in Figure 48 and Figure 49.
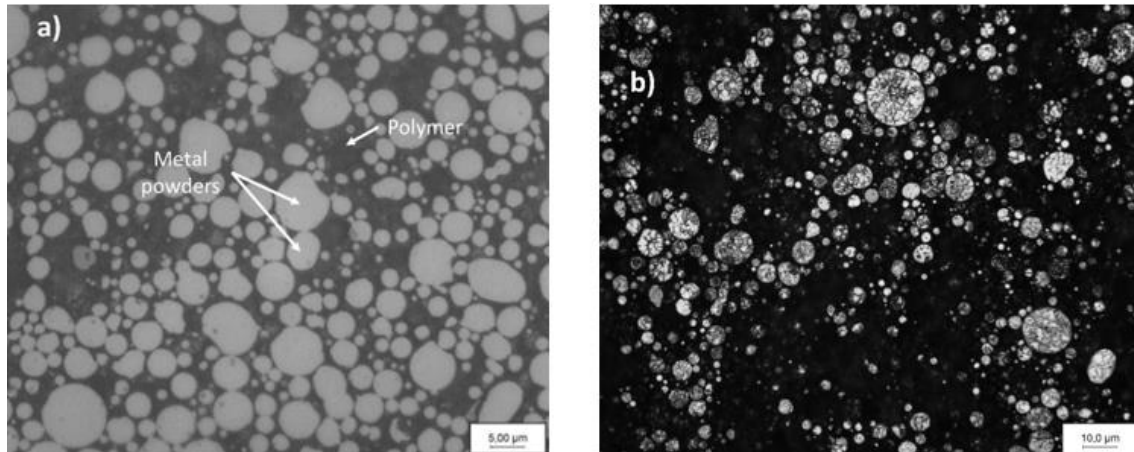
Figure 49. Optical micrographs of Markforged H13 metal-polymer filament a) before etching b) revealing microstructure

Material health

Methods

The preparation of samples involved cold mounting in a resin and a series of abrasive grinding using Silicon Carbide (SiC) papers from the grit of 800 up to 4000, decreasing coarseness. This was followed by polishing with a solution comprising diamond particles of 3 and 1 µm and ultrasonic cleaning for at least 10 minutes. After these steps, the samples were etched by exposing them to Kalling's № 2 or Nital 3 % etchants for around 30 seconds to reveal their microstructure. The Kalling's №. 2 reagent is a solution of copper chloride ($CuCl_2$), hydrochloric acid (HCl) and ethanol (C_2H_5OH) which is used for particularly high-speed steels and stainless steels (17-4 PH in this case). In contrast, Nital 3 % is a solution of nitric acid (HNO_3, 68 % pure) diluted in ethanol (C_2H_5OH) compatible with H13, which is less rich in chromium. The as-sintered samples were also processed in a similar way using an optical microscope and image processing software, as mentioned above. However, this time the focus was on determining the porosity content and the size of the pores rather than the metal density. The optical images captured at a magnification of x20 were converted to greyscale (0-255 being black-to-white intensity). The porosity was defined as an intensity threshold of 40-125. While processing the images for porosity measurements, pores having less than one µm² area were not considered in the analysis; they were too small to be adequately detected, and such tiny pores have a negligible impact on mechanical properties.

Results

The analysis of the surface of as-sintered 17-4 PH and H13 steel specimens revealed the presence of several cavities, as shown in Figure 50 and unfilled deposition layers. Porosity and deposition issues, as observed here, are typical of metal extrusion additive manufacturing processes. It is likely caused by material under-extrusion, meaning that the extruder is not supplying enough filament to the manufacturing process or manufacturing process parameters are inappropriate [37].
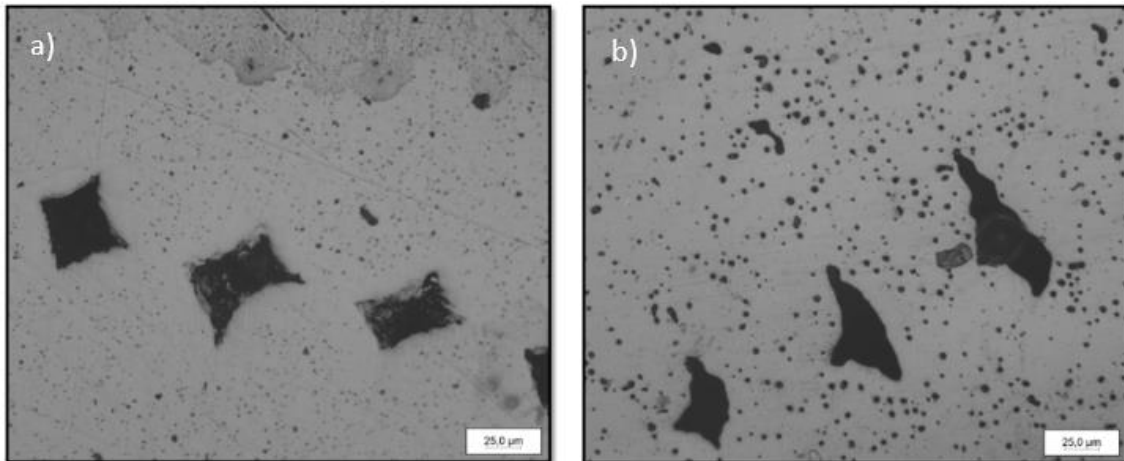
Figure 50. Optical images showing porosity and cavities in a) 17-4 PH and b) H13 on XY plane.

In 17-4 PH specimens, the porosity was primarily dominated by tiny pores measuring around 3 μm in diameter. A significant percentage (approximately 85 %) of pores were less than 20 μm in size, as seen in Figure 51. Additionally, most pores were found to be in the typically spherical-shaped with an average circularity of 0.85. The analysis was conducted on a 6.5 % and 12 % surface area out of the available 40 and 13 mm² sections.

In H13 samples, pores with a diameter of 2-4 μm were the most prevalent, with around 97 % of pores measuring under 12 μm in size, as shown in Figure 51. These pores were circular in shape, with an average circularity of 0.86. Pores with a circularity between 0.2 and 0.6 could be related to cavities as they were also considered in the porosity analysis. If these cavities were not considered, the porosity percentage and circularity would have been improved. A summary of the results can be found in Table 25. Comparing these results to the reference, it can be derived that the porosity percentages found in this study are similar to the ones reported in [38], where relative porosity of 4.08-6.48 % on the XY face and 2.22-3.07 % on the XZ face in 17-4 PH sample and in [37], where relative porosity of 6 % in 17-4 PH and 5 % in H13 on the XY face was found.
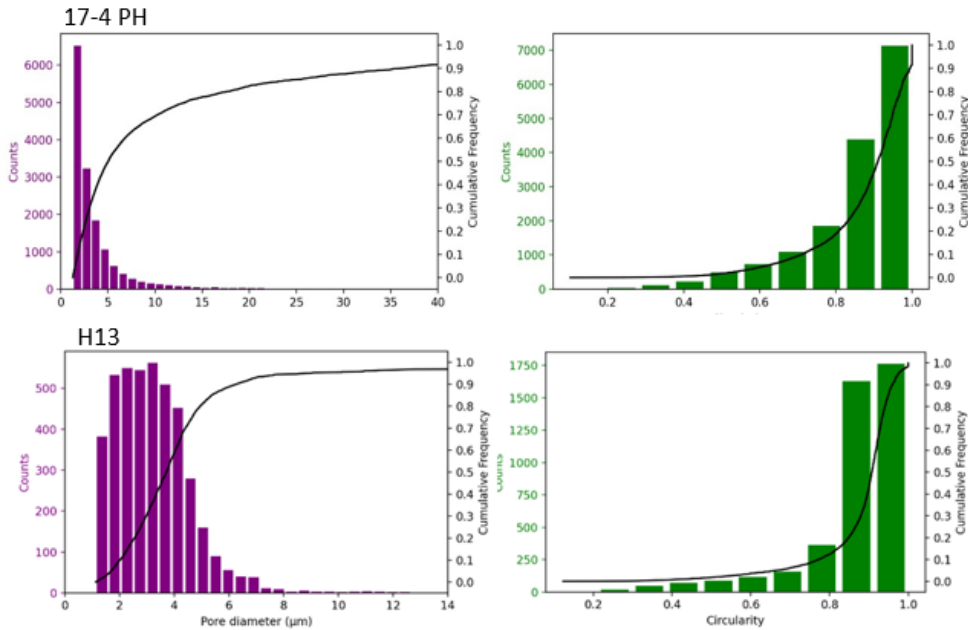
Figure 51. Pore size distribution and circularity distribution of as-sintered samples.

Table 25.Summarized results of porosity for both steel samples.

Samples	17-4 PH		H13	
Direction	XY plane	XZ plane	XY plane	XZ plane
Property	Value	Value	Value	Value
Diameter of pores	3.2 µm	2.3 µm	4.2 µm	3.7 µm
Circularity	0.85 ± 0.14	0.86 ± 0.14	0.86 ± 0.13	0.85 ± 0.14
Porosity	4.8 % ± 2.1	2.1 % ± 0.8	5.6 % ± 2	4.5 % ± 1.5

Microstructural characterisation

Ceit and Enit has fulfil the characterization of H13 and 17-4PH samples manufactured by Fused Filament Fabrication (FFF). 17-4PH was manufactured using Markforged FFF equipment while H13 samples were manufactured with two different equipment: open machine Lynxter with NANOE filament and Markforged equipment.

Methods

The X-ray diffraction analysis was conducted using a Philips X'PERT machine, using Cu-Kα radiation with a wavelength of 1.540598 Å. The samples were scanned at a voltage of 40 kV and current of 50 mA, using a 0.5 mm beam diameter, over a range of 30° to 125° with a curved Position Sensitive Device (PSD) that covers a circular arc of 8° with a step size of 0.012° and 30.05 s per step. Additionally, an H13 sample was scanned between 43° to 46° with a step size of 0.01° and 1000 s per step for a more detailed analysis of the peak in that range. The phase identification was determined by analysing the XRD spectra using the X'pert High Score software

and the JCPDS database, which included potential phases such as ferrite, martensite, and austenite of steel.

Samples were prepared as explained in the material's health parts. The microstructure of the as-sintered and heat-treated samples was examined using a PMG3 optical microscope from Olympus. Additional analysis on as-sintered samples was performed using a ZEISS EVO10HD15 Scanning Electron Microscope (SEM) equipped with a LaB$_6$ gun. The SEM had a Secondary Electron (SE) and Backscattered Electron (BSE) detector. An Energy Dispersive Spectrometer (EDS) X-MaxN 50 XMX1003 from Oxford Instruments was utilized to highlight the concentration of alloying elements in micro-segregated zones and determine their composition. An accelerating voltage of 15 kV and a work distance of 10 mm were used during this SEM analysis.

Results

17-4 PH: Parts done with Markforged

The microstructure of 17-4 PH steel at room temperature is shown in Figure 52. It comprises pores and martensite laths arranged in packets of varying sizes. It cannot be ruled out that a small amount of retained austenite may be present, as the quantity may be so low that it is nearly impossible to observe through optical microscopy. It is also possible that delta ferrite may have formed during the high-temperature sintering process of 17-4 PH stainless steel. This is supported by the iron-carbon phase diagram of steel, which indicates that low amounts of carbon can increase the formation of delta ferrite. Previous research by Wu et al. [39] suggests that sintering 17-4 PH stainless steel above 1220 °C can form delta ferrite in a continuous grain boundary morphology. Black dots larger than the pores (mentioned in the previous section) could be observed after etching the sample. From an optical microscope, it was impossible to conclude if this feature was a precipitate revealed or dissolved by etching or pores. In summary, the microstructure of 17-4 PH steel is closer to that of the wrought 17-4 PH stainless steel described by Sabooni et al. [40] than the microstructure of 17-4 PH LPBF as-built parts reported by Yeon et al. [41]. Scanning Electron Microscopy (SEM) and X-ray diffraction (XRD) analysis were conducted to understand the microstructural components better. SEM analysis reveals that the dark point observed by OM after etching are pores and composition in the range of 17-4 PH standards.
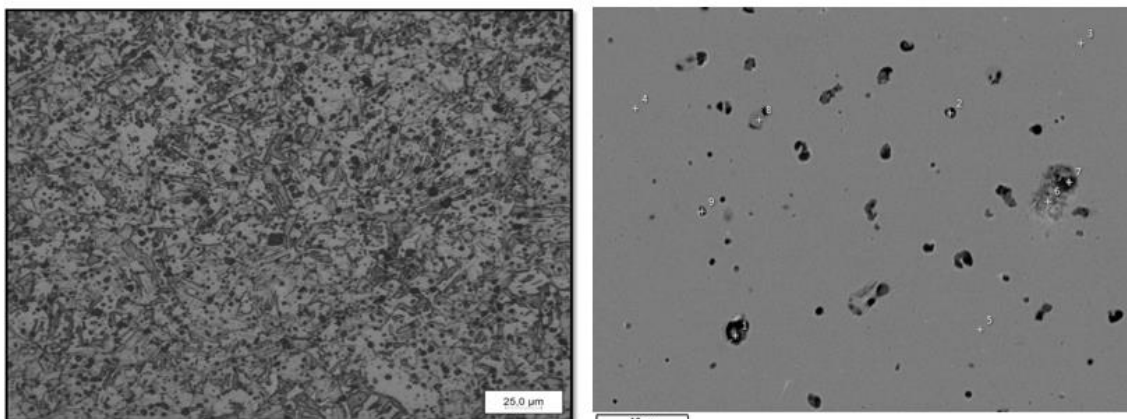
Figure 52. Optical micrograph after etching (left) and SEM images (right) of as-sintered 17-4 PH stainless steel.

The sample phase analysis was conducted through XRD, and the spectra collected for 17-4 PH are shown in Figure 53. Unlike LPBF [42], comparing these spectra to JCPDS Powder Diffraction File (PDF) revealed that any retained austenite phase or carbides were not detected in the as-sintered samples. Due to the low carbon quantity in these alloys, the BCT martensite displays minimal lattice distortion. As a result, it is not possible to differentiate between the BCC ferrite and BCT martensite by XRD alone. In this case, the standard convention for steels is applied, in which both phases are considered to have the BCC structure and hence, indicated by the α phase (representing α-/δ-ferrite and martensite phase).
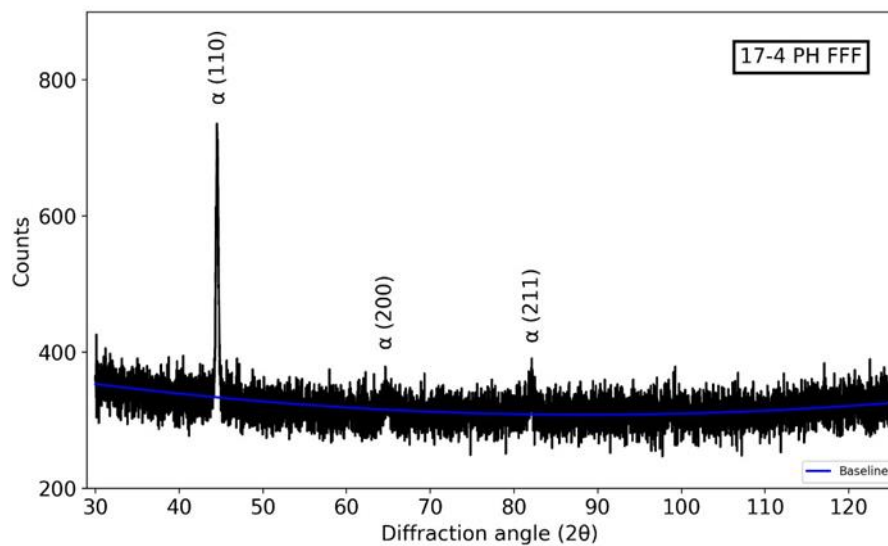
Figure 53. XRD spectra of as-sintered 17-4 PH stainless steel specimen

In the XRD spectrum of 17-4 PH, the (110) peak at a 2θ angle of approximately 44.51° has a higher intensity than other peaks of bcc structure at 64.63° and 82.13°. Since 17-4 PH is a precipitate-hardened martensitic stainless steel, the sample is likely composed of multiple phases, with martensite being the dominant phase and potentially some ferrite. However, the positions of the experimental peaks do not perfectly match theoretical peaks due to the presence of the different amounts of carbon and alloying elements in the sample compared to the reference. Still, they are closer to the characteristic peaks of martensite than ferrite (Table 26). Additionally, the relative intensity of the (200) and (211) peaks show a similar trend to the thermally debound 17-4 PH sample XRD spectra peaks reported by Schroeder et al. [43]. The remaining two peaks (220) at 99.26° and (310) at 117.07° were difficult to distinguish from the noise created by the diffractometer. The diffraction pattern is generally consistent with the standard diffraction pattern, indicating that there is probably no preferred orientation or texture in the sample along any of the diffraction planes. In conclusion, the microstructure is martensitic and in harmony with the literature.

Table 26. Diffraction angles for each peak in both steels and referential data for steel phases [1] and [2] correspond respectively to data from reference [43] and Standard JCPDS no. 00-006-0696.

Samples					Phase reference						
17-4 PH			H13		Martensite[1]		Ferrite[2]		Austenite[1]		
hkl	2θ	I (%)	2θ	I (%)	2θ	$I_{\alpha'}$ (%)	2θ	I_α (%)	hkl	2θ	I_γ (%)
110	44.51	100.0	44.63	100.0	44.652	100	44.674	100	111	43.695	100
200	64.63	14.3	64.97	61.0	64.817	11.6	65.023	20	200	50.794	42.5
211	82.13	17.1	82.22	9.3	82.095	17.4	82.335	30	220	74.739	17.8
220	99.26	-	98.75	8.0	98.711	4.5	98.949	10	311	90.629	16.6
310	117.07	-	116.44	6.7	115.83	6.2	116.39	12	222	95.98	4.6

H13: Parts done with Markforged

The microstructure of H13 steel at room temperature is illustrated in Figure 54. It features a combination of pores and prior austenite grain boundaries. The martensite laths that should be present in the matrix could not be observed, leading to the perception that the microstructure is mainly composed of ferritic/pearlitic phases. The grain boundaries appeared to have segregation zones with high concentrations of alloying metals. Therefore, Scanning Electron Microscopy (SEM) was conducted to understand the microstructural components better. The composition determined by the energy dispersive x-ray spectra suggests that it is similar to the standard ASTM A681 composition of H13.
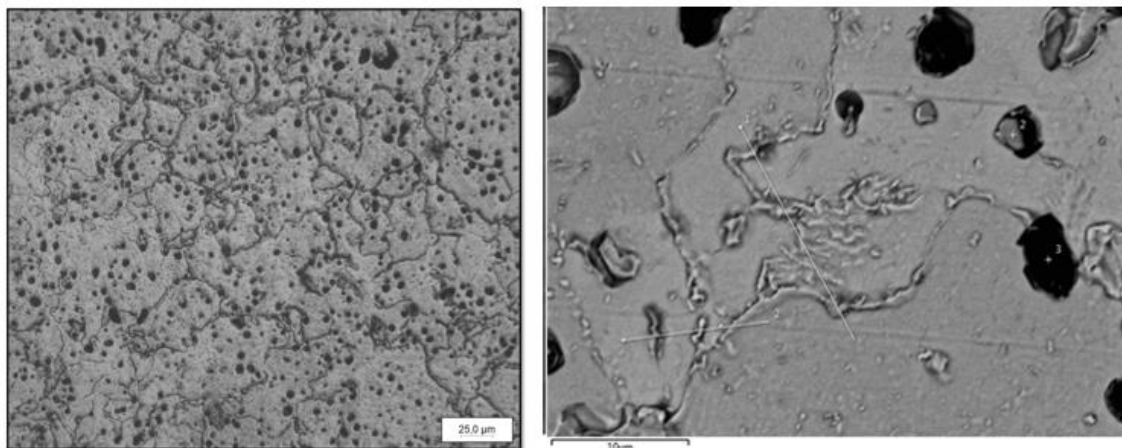
Figure 54. Optical micrograph (left) and SEM image (right) of as-sintered H13 PH steel after etching.
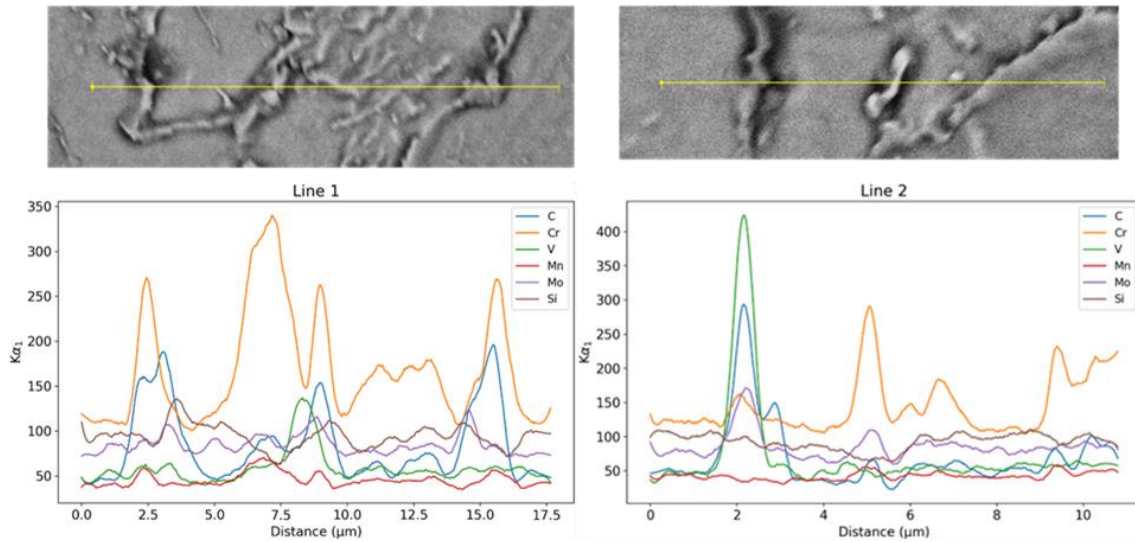
Figure 55. Zoomed-in view of both lines and their composition distribution.

Finally, to confirm the composition of the segregation zones at the grain boundaries, the line analysis was performed in those areas, as shown in Figure 55. The results indicate that these zones are rich in carbon, chromium, molybdenum, and vanadium, with concentrations higher than those typically found in the matrix.
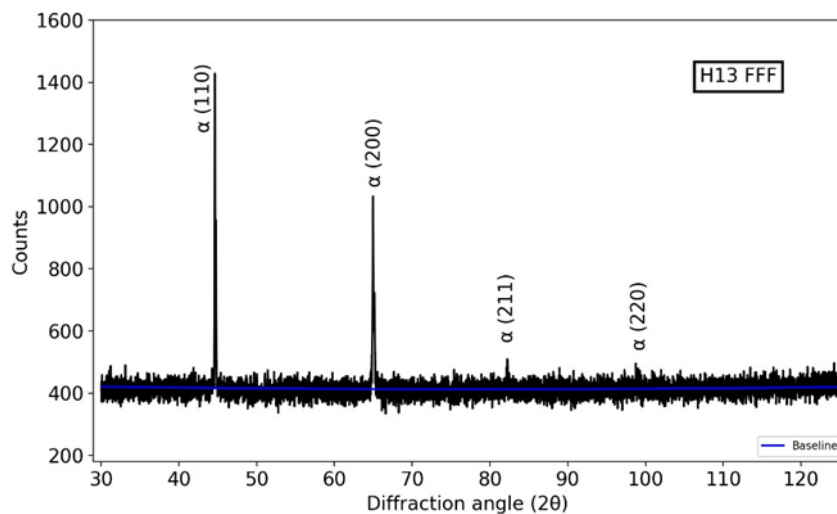
Figure 56. XRD spectra of as-sintered H13 specimen in XY plane.

Concerning XRD analysis, similar to 17-4 PH, only BCC peaks are observed in H13 XRD spectra (shown in Figure 56), and no retained austenite was detected too. The first peak (110) at 44.63° has the most vigorous intensity. However, the second (200) peak at 64.97° also has a noteworthy intensity compared to the standard H13 diffraction pattern [44]. This suggests that texture may be present in the (200) direction, but further EBSD analysis is required to confirm this. The other two peaks (211) at 82.22° and (220) at 98.75° have a minimal intensity, and the last peak (310) is difficult to distinguish from the noisy background. The hardness value of the as-sintered H13

sample was significantly lower than the expected value given by the data sheet [45], raising concerns about ferritic phases in the as-sintered samples.

Comparison (Markforged vs Nanoe Filament) and summary of characterisation

Table 27 and Two sintering temperatures (1350 and 1400 °C) were used in order to densify H13 alloy manufactured with Nanoe filament. Sintering at 1400 °C, generated a higher densification and different microstructure, with presence of liquid channels, as it is showed in the

Figure 58. The liquid channels appear because the temperature is close to supersolidus liquid phase [46]. Furthermore, the sample sintered at higher temperature present higher hardness due to the formation inside the grains of a lamellar structure.

Table 28 shows the density and hardness values obtained for H13 and 17-PH after different sintering temperatures and HIP treatments. In all the cases, the density and the hardness increased after HIP treatment at 1150 °C and 150 MPa.

Table 27. Density and hardness values for H13 steel

FFF Technology	Heat treatment	Density (%DT)	Hardness (HV1)	Hardness (HRC (conversion))
Markforged	As received (sintered with Markforged conditions)	92	169	6
	HIP 1150 °C/1h	96	645	58
Lynxter + Nanoe fila-ment	HT 1400 °C / 2h	85	725	62
	HT 1350 °C / 2h	81	510	50
	HT 1400 °C / 2h + HIP 1150 °C/1h	97	817	65
	HT 1350 °C / 2h + HIP 1150 °C/1h	93	701	61

Two sintering temperatures (1350 and 1400 °C) were used in order to densify H13 alloy manufactured with Nanoe filament. Sintering at 1400 °C, generated a higher densification and different microstructure, with presence of liquid channels, as it is showed in the

Figure 58. The liquid channels appear because the temperature is close to supersolidus liquid phase [46]. Furthermore, the sample sintered at higher temperature present higher hardness due to the formation inside the grains of a lamellar structure.

Table 28. Density and hardness values for 17-4PH steel.

Technology	Heat treatment	Density (%DT)	Hardness (HV1)	Hardness (HRC (conversion))
Markforged	As received	94	368	38
	HIP 1150 °C/1h	98	392	41

HIP treatment is able to close most of the porosity (only open porosity in the contour was not able to be closed) and therefore the density of samples increased (Figure 57,

Figure 58 and Figure 59).
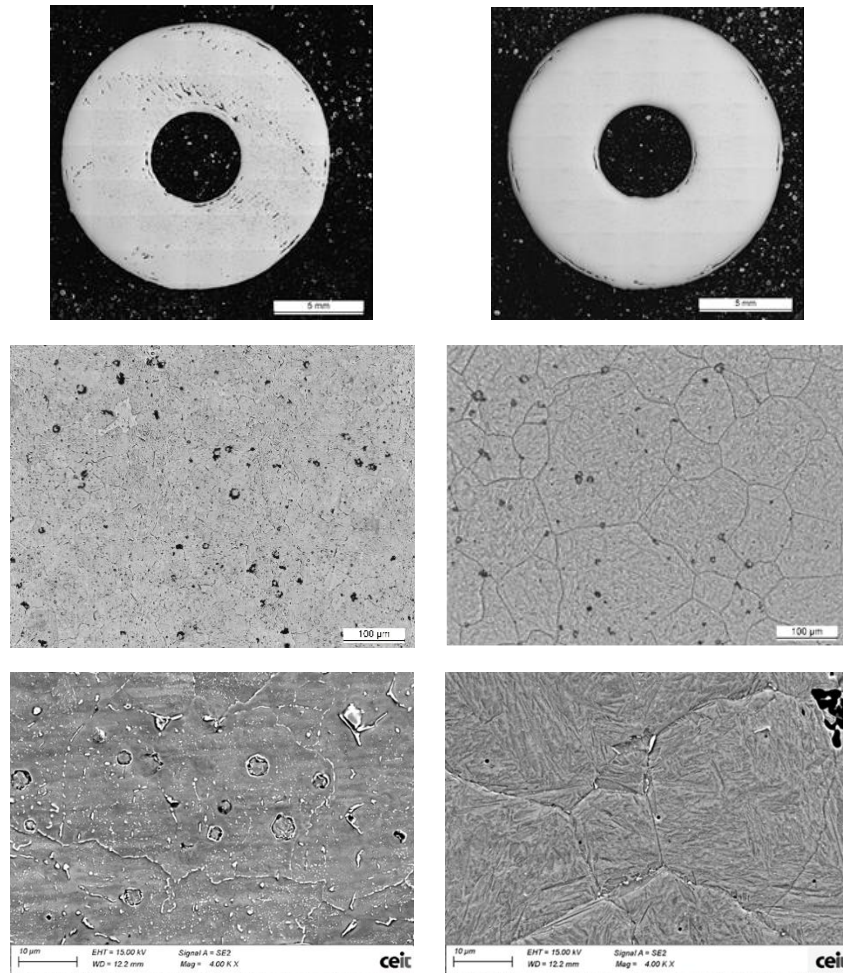
Figure 57. Optical and FEG-SEM images of Markforged H13 as manufactured (left) and after HIP (right).

In addition, after HIP the microstructure changes forming a lamellar structure in H13 steel which leads to a significant increase in hardness (Figure 57 and

Figure 58).

Sintering @1350 °C   Sintering @1350 °C + HIP

Sintering @1400 °C   Sintering @1400 °C + HIP
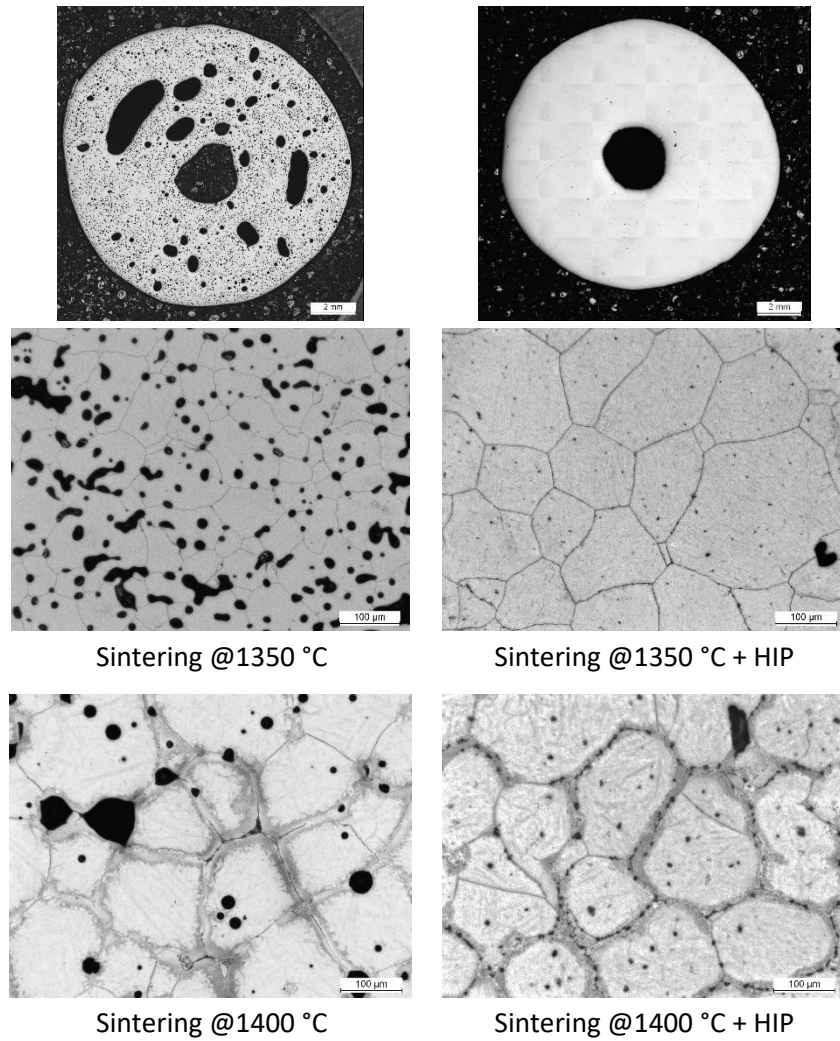
Figure 58. Optical images of H13 FFF-Nanoe after sintering (left)and after HIP (right).
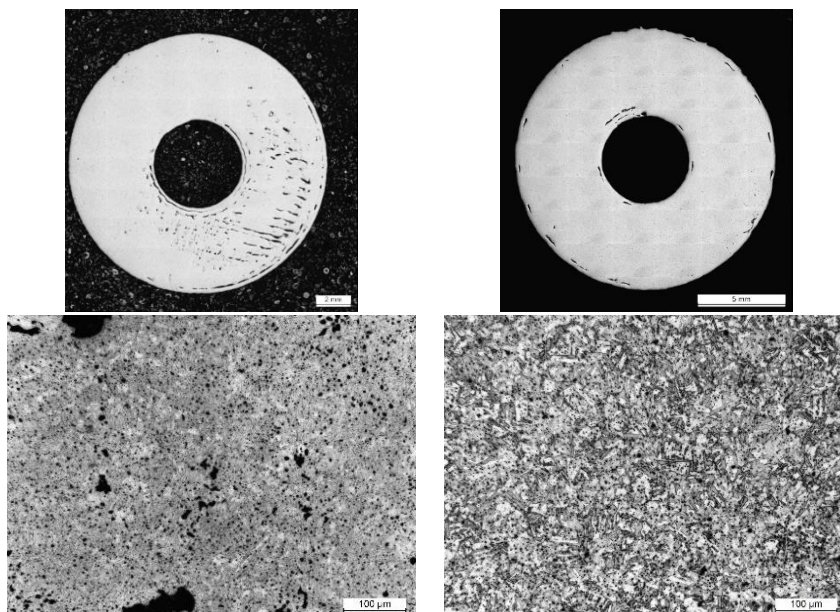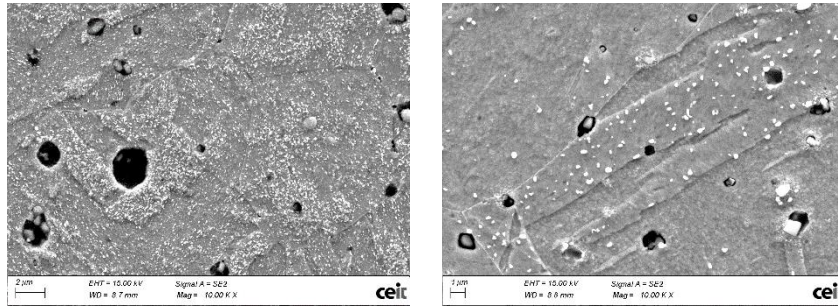
Figure 59. Optical and FEG-SEM images of Markforged 17-4PH as manufactured (left) and after HIP (right).

The microstructures present lower amount of precipitated after HIP treatments in both materials. This could be related with the higher cooling rate used in the HIP cycle in comparison with the slow cooling rate of the sintering treatment. Figure 60 and Figure 61 shows EDS analyses of the different alloys after sintering and after HIP treatment. On one hand, H13 steel presented grain boundary precipitates enriched in V, Mo, Cr and Mn. On the other hand, 17-4PH had Cu precipitates along the microstructure and Cr or Nb precipitates at grain boundary.
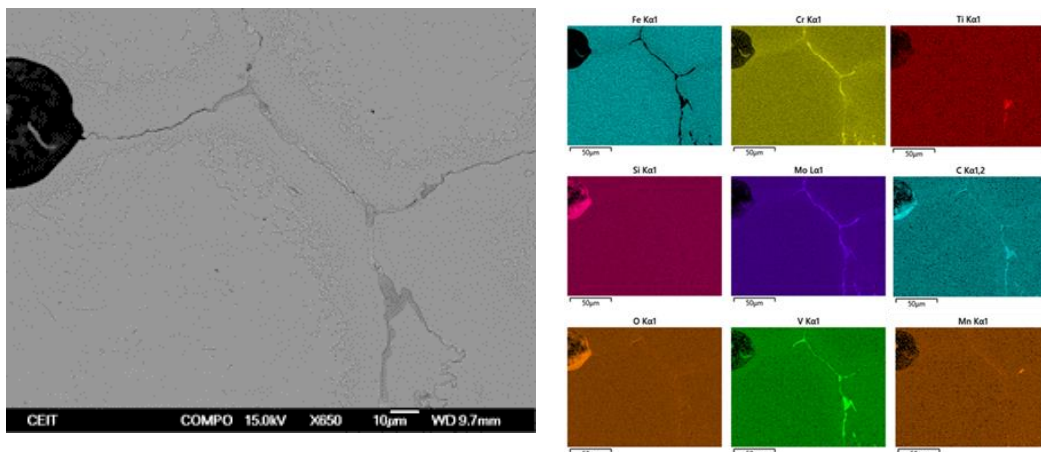
Figure 60. EDS analysis of H13 FFF after sintering treatment.
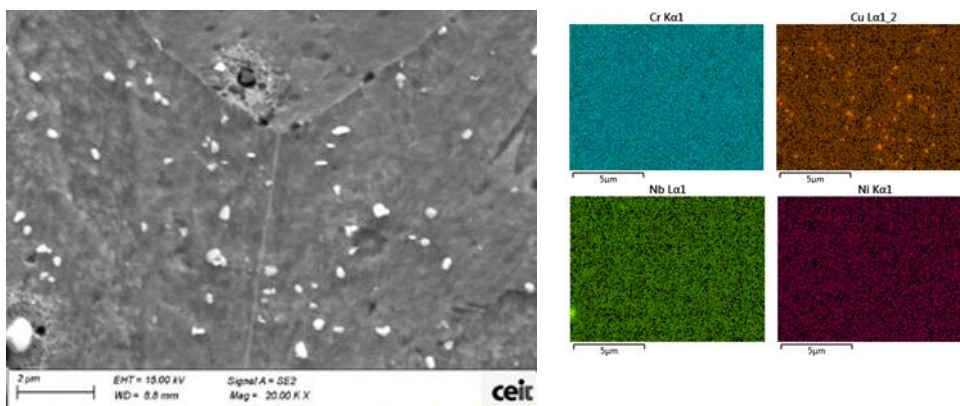
Figure 61. EDS analysis of 17-4PH after HIP treatment.

Mechanical characterisation

Methods

The macro-hardness test was performed using the Vickers method with a load of 1 kgf (HV1) and five kgf (HV5) on Zwick/Roell ZHV2.5 hardness tester in compliance with the ISO 6507-1 standard, and at least five indents were made on the central section of the specimen. The results of the macro-hardness test may be affected by the porosity of the FFF samples, so micro-hardness tests were also conducted using a Zwick/Roell Durascan 70 micro-hardness tester with a load of 100 gf (HV0.1) to gain a more detailed understanding of the sample's hardness. The microhardness profiles chosen can be seen in Figure 62 as dashed lines. On each profile, 100 indents were made with a distance of 77 µm between them on the 17-4 PH sample and 87 µm between them on the H13 sample. This means that the indents were made closer together on the 17-4 PH sample than on the H13 model, which is likely due to the difference in hardness of the two materials and the distance between the two indents was set higher than three times the value of diagonal of indents. The TestXpert software provided by Zwick/Roell was used for the hardness measurements. Again, the Zwick/Roell ZHV2.5 hardness tester was used for determining the Vickers hardness of heat-treated samples on the XY plane, with a one kgf load (HV1) in compliance with the ISO 6507-1 standard. Twenty-five indents were made on the central part of each sample in the XY plane, and the distance between each indentation was 300 µm.
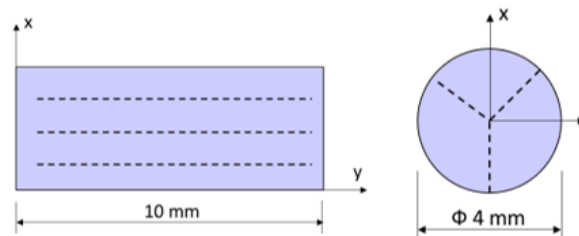
Figure 62. Micro-hardness test plan

Results

Parts done with Markforged

The results of the macro-hardness test on as-sintered 17-4 PH reported higher hardness values on the XZ plane (average value 331 ± 12 HV1) than those on the XY plane (average value 318 ± 4 HV1). However, the HV5 values in the 17-4 PH sample presented the opposite trend, with the average weight being higher on the XY plane (324 ± 4 HV5) than on the XZ plane (306 ± 30 HV5). The H13 samples had average hardness values of 164 ± 3 HV5 on the XY surface and 163 ± 1 HV5 on the XZ surface. Overall, the results did not provide a clear conclusion about the mechanical anisotropy caused by the fabrication process. Therefore, further verification was needed through micro-hardness testing and analysis to confirm this observation. However, it is worth noting that the macro-hardness values for both 17-4 PH and H13 samples were consistent across both the XY and XZ planes, indicating a lower degree of anisotropy in this sample.

The micro-hardness results of 17-4 PH samples are illustrated in Figure 63. As expected, the Vickers hardness values HV0.1 on both the XY and XZ surfaces showed homogeneous hardness across the sample (average value of 348 ± 17 HV0.1 on the XY face and 344 ± 13 HV0.1 on the XZ face) except on some indents which may have impacted by pores. The difference between the hardness values on each surface is negligible, indicating that the as-sintered 17-4 PH samples have a very low degree of anisotropy or nearly isotropic in hardness even though slightly of anisotropy was observed in porosity. Macro hardness is typically used to evaluate the material's overall resistance to wear. In contrast, microhardness is used to assess the hardness of specific microstructural regions or phases or to examine property gradients at the mesoscale level.

Figure 63 shows the microhardness variations in the building direction (XY plane) and the radial direction (XZ plane) of the as-sintered H13 FFF sample. The results indicate that the microhardness of the sample is consistent and evenly distributed in both the building direction (XY plane) and the radial direction (XZ plane), with similar average values of 177 HV0.1 and 176 HV0.1 respectively, and relatively small standard deviations of 11 and 12 respectively. The results provided in the literature [37] for as-sintered 17-4 PH steel components show a value of 34 HRC, roughly equivalent to 320 HV, and a hardness value for as-sintered H13 steel components 37 HRC, which is nearly equal to 351 HV. The authors involved have presented the value as an average, and therefore, there needs to be more information available on the value variations in different directions. The reference value provided by the supplier is 30 HRC (~285 HV) for as-sintered 17-4 PH [47] and 40 HRC (~388 HV) for as-sintered H13 [45]. It is evident that both the macro and microhardness values of the as-sintered H13 steel samples are significantly lower than the reference data [37] and the supplier's value [45]. This discrepancy could be attributed to several factors, such as the sintering conditions, the composition of the powder used, or the cooling rate of the sample. On the other hand, both macro and microhardness values of the 17-4 PH samples are higher than the supplier's value [45] on both planes and higher than the reference data [37] on the XY plane. Since the CCT diagrams of conventional 17-4 PH [48] and H13 [49] indicate that the hardness of 17-4 PH is less affected by the cooling rate than H13.
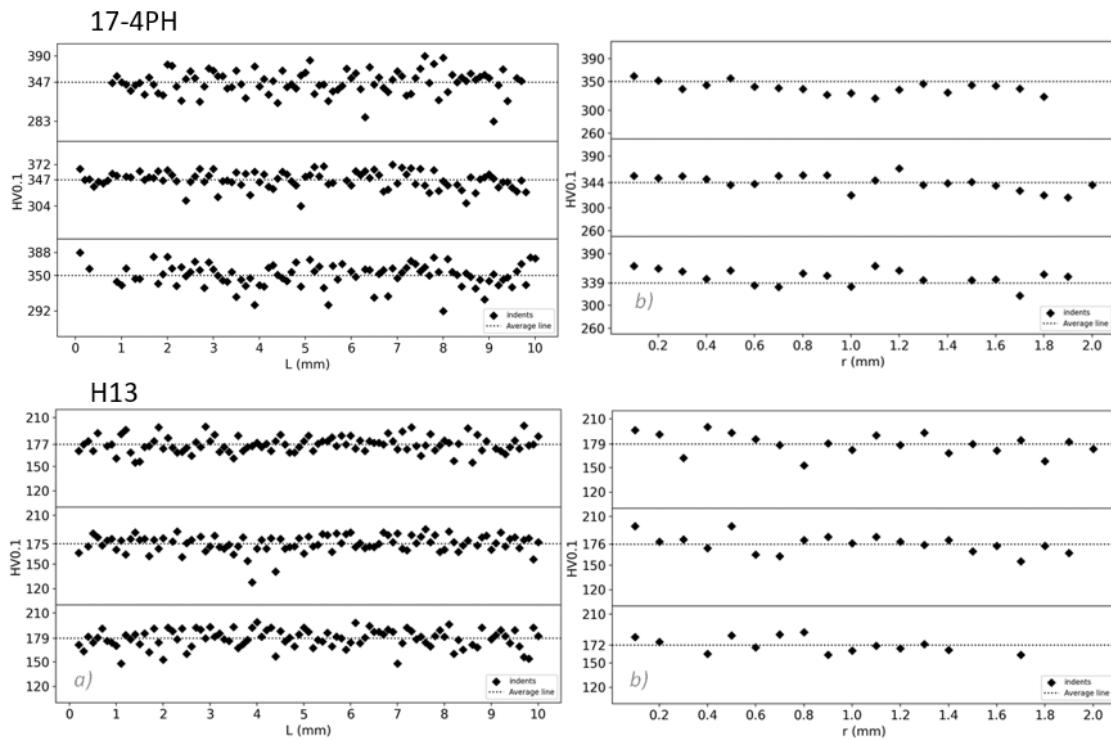
Figure 63. Microhardness profiles of as-sintered 17-4 PH (top) and H13 (bottom) specimens on (a) XY surface and (b) XZ surface.

Parts done with Nanoe Filament

Vickers hardness (1Kg) results for H13 samples manufactured with Nanoe filament are summarized in the following table:

Thermal cycle	HV10
Sinter at 1400 °C	725 ± 52
Sinter at 1350 °C	510 ± 72
Sinter at 1400 °C + HIP	817 ± 14
Sinter at 1350 °C + HIP	-

Samples sintered at 1400 °C show higher hardness than samples sintered at 1350 °C. This could be related with the higher density achieved in the samples (85 % vs 81 % density) and due to lower number of microstructural defects in the samples sintered at 1400 °C. After HIP most of the pores are closed, the density increased up to 97 % and the grain grew. The hardness of HIP samples increased despite of the grain growth, but this was related to the lamellar structure formation due to the fast cooling rate within the HIP sample.

Heat treatment study

Methods

To study the phase transformations, cylindrical surface-parallel samples with a diameter of 4 ± 0.1 mm and a length of 10 ± 0.3 mm were used. These samples were placed in a quenching dilatometer DIL L78 Q from Linseis. Before the measurement, the furnace atmosphere was twice brought to vacuum until 2×10^{-2} mbar and then filled with Argon. The samples' dilatations were measured using Alumina (Al_2O_3) and Quartz push-rods under a vacuum or in an Argon (Ar) atmosphere, the temperature was controlled using a type K thermocouple that was spot welded to the specimen's surface. The solution temperature for 17-4 PH samples was decided from literature and DTA analysis. It was set to 1100 °C and the hold time was 30 min, according to previous research by Rowolt et al. [48], and for H13 samples, it was set to 1040 °C and the hold time was set to 30 min, according to research done by Deirmina et al. [50]. The phase transformations were analysed through continuous heating at 10 K/min (or 0.167 K/s) and cooling at different rates. To detect phase transformation temperatures or precipitation events, the dilatometry data was differentiated concerning temperature as recommended in [50]. The Linseis Evolution software created Continuous Cooling Transformation (CCT) diagrams for both alloys. The transformation temperatures were also determined using Differential Thermal Analysis (DTA) with a Setsys Evolution (Setaram) instrument. An alumina crucible with a 4 mm diameter was used, and it was loaded with different specimens cut from the cylindrical samples, having 40 to 70 mg. The transformations were studied from 20 to 1100 °C (in 17-4 PH samples) and from 20 to 1040 °C (in H13 samples) throughout continuous heating and cooling at different rates under a 40 ml/min flow of argon to avert oxidation. The baseline was obtained by conducting a second scan under similar conditions but without a sample. By subtracting the signals, any phase transformation or precipitation phenomenon during the heating, as well as any martensitic transformations during cooling, can be identified

Results

Parts done with Markforged

Curves analysis

The results of a dilatometry test on 17-4PH steel are shown in Figure 64, which displays the dilatation strain (black curve), and derivative strain (red curve) as the steel is heated from room temperature to 1100 °C. The first contraction peak can be observed around 500 °C, associated with a Cu-precipitation in a recent conducted study [48]. The austenitic transformation (from α'-martensite to ϒ-austenite) causes a significant volume reduction as the steel is heated. The temperature at which this austenitic transformation begins (Ac_1) is approximately 678 °C, but precisely determining the end of this transformation (Ac_3) is unclear. Ac_3 is typically the point where the dilatation strain becomes nearly linear again, which in this case is approximately 728 °C. However, a small nonlinear contraction peak is still observed at around 980 °C, which was related to the end of austenite formation by Christien et al. in [51], who observed the presence

of martensite phase at 930 °C on the *in situ* neutron diffraction pattern of 17-4 PH steel, indicating incomplete austenitisation.
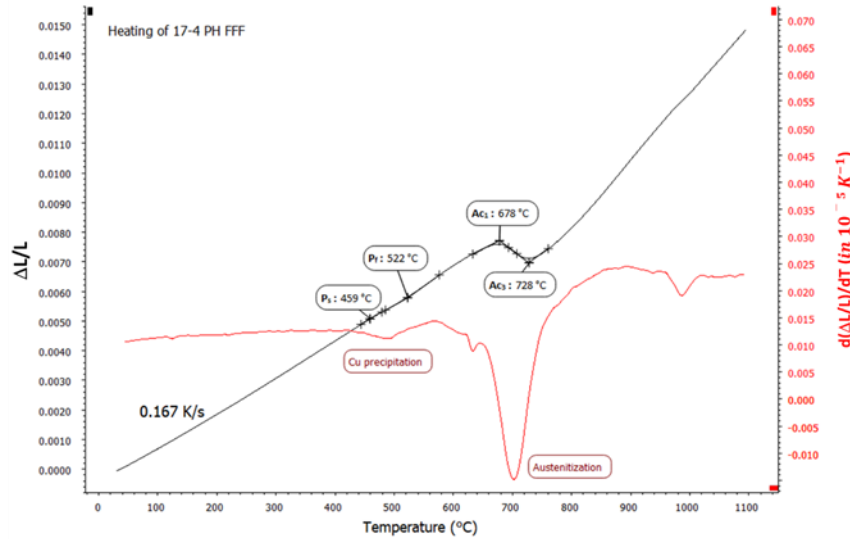
Figure 64. Dilatation strain and derivative strain curves while heating as-sintered 17-4 PH FFF samples.

Rowolt and other involved authors [48] conducted stepwise heating of conventional 17-4 PH samples up to different solution-annealing temperatures ranging from 700 to 1100 °C. The absence of a Cu-precipitation peak in reheating the DSC curve was observed when the sample was heated to a temperature of 800 °C, relating the phenomenon to the lack of dissolution. In contrast, heating and the maximum precipitation peak area were observed when the sample was heated to a temperature of 1000 °C.
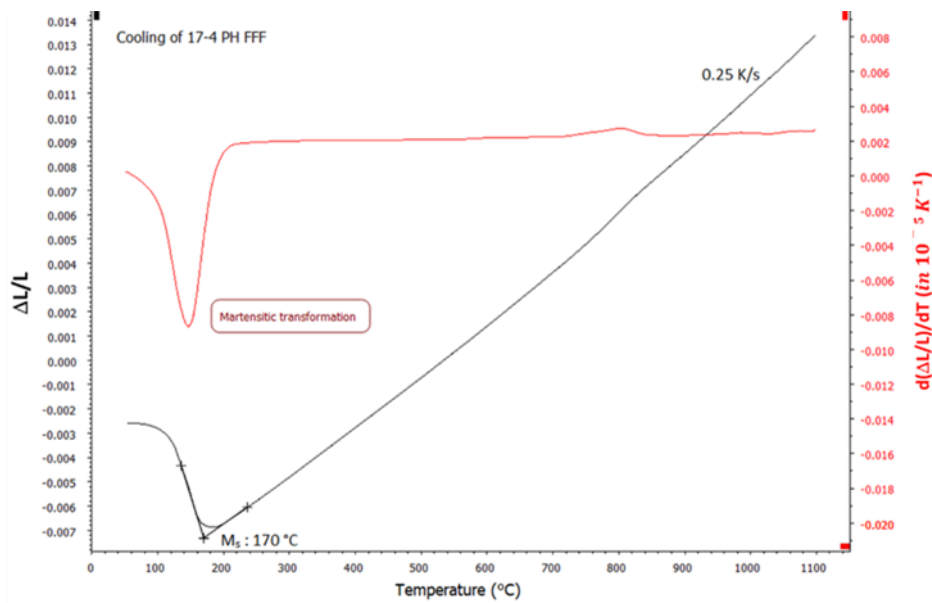

Figure 65. Dilatation strain and derivative strain curves while cooling as-sintered 17-4 PH FFF samples

Hence, the contraction peak around 980°C in the dilatation strain curve was attributed to the final dissolution of the Cu-rich phase. In [52], Kapoor and Batra also assigned this peak to the second step of austenitisation while conducting dilatometry analysis of M350 and PH 13-8 Mo maraging steels, but it was absent in case 17-4 PH stainless steel. Hence, the identification of this peak remains controversial.

Figure 65 illustrates the dilatation strain that occurs from 1100 °C to room temperature during the cooling process. The volume expansion caused by the martensitic transformation is evident. The 'martensite start' temperature, or Ms, can be determined with the tangent method at 170 °C. The tangent method determines the phase transformation temperature in dilatometry curves. The tangent method is based on the observation that the slope of the dilatometry curve changes at the phase transformation temperature. An additional change in the slope of the dilatation strain curve was observed around 100 °C, which is believed to be the 'martensite finish' temperature (M_f). This assumes that the martensitic transformation is nearing completion. However, the accuracy of the M_f temperature cannot be confirmed in this study as the dilatation curve does not become linear again.
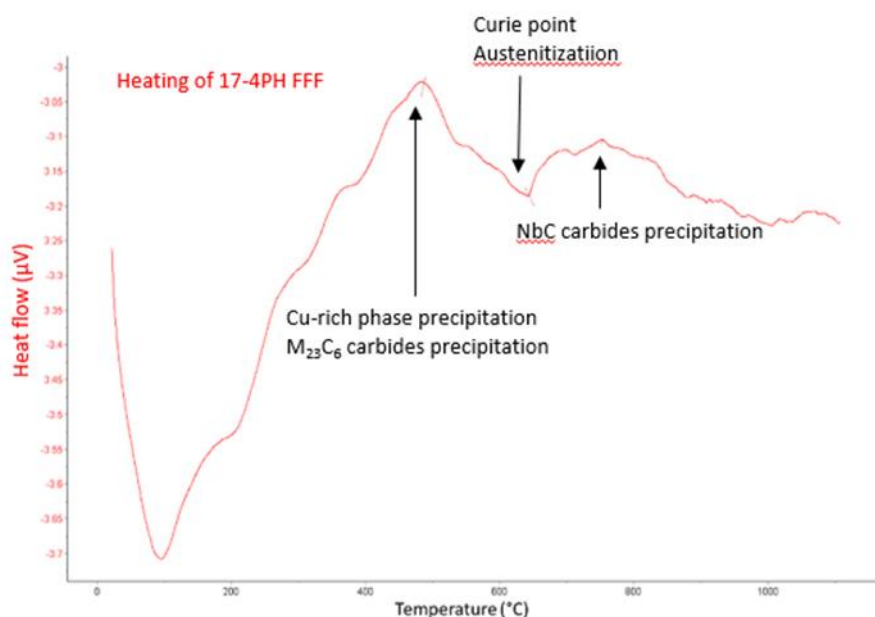
Figure 66. DTA signal of as-sintered 17-4 PH FFF sample while heating.

The DTA curve while heating the as-sintered 17-4 PH sample is displayed in Figure 66. The initial exothermic event observed in the 17-4 PH sample occurred at a temperature of 484 °C. This peak is believed to be caused by the formation of Cr-rich $M_{23}C_6$ carbides and Cu-rich precipitates, according to Lashgari et al. [53]. It is coherent with the results obtained by the dilatometry analysis explained before. The second thermal event, an endothermic peak, was found around 642 °C, which can be attributed to both Curie transition (ferromagnetic -> paramagnetic transition) and austenitisation. The final exothermic peak observed at around 753 °C could be caused by the precipitation of NbC carbides in the matrix or at the grain boundaries [53].

However, the precise temperature at which the transformation from ferrite to austenite starts (Ac_1) was challenging to determine due to noise in the DTA signal and multiples phenomenon in a small temperature range.

A similar thermal analysis was performed on the H13 sample. The dilatometry curve of as-sintered H13 demonstrates a linear pattern of expansion during the sample is heated up to 700 °C, which aligns with the expected thermal expansion. The derivative strain supports this trend. A contraction is observed between 700 and 750 °C which could be related to the Curie transition, followed by another contraction between 845 °C (Ac_1) and 887 °C (Ac_3), which is due to the transformation from ferrite to austenite (α-γ). As already shown, 17-4 PH phase transformations were measured by the tangent method during cooling.

Application on CCT diagrams

Dilatometry curves were recorded and analysed for several cooling rates. Regardless of the cooling rate, as-quenched 17-4 PH samples revealed the martensitic microstructure, as illustrated in Figure 67. A faster cooling rate (35 K/s) leads to a more homogeneous microstructure due to the reduced time for precipitation.
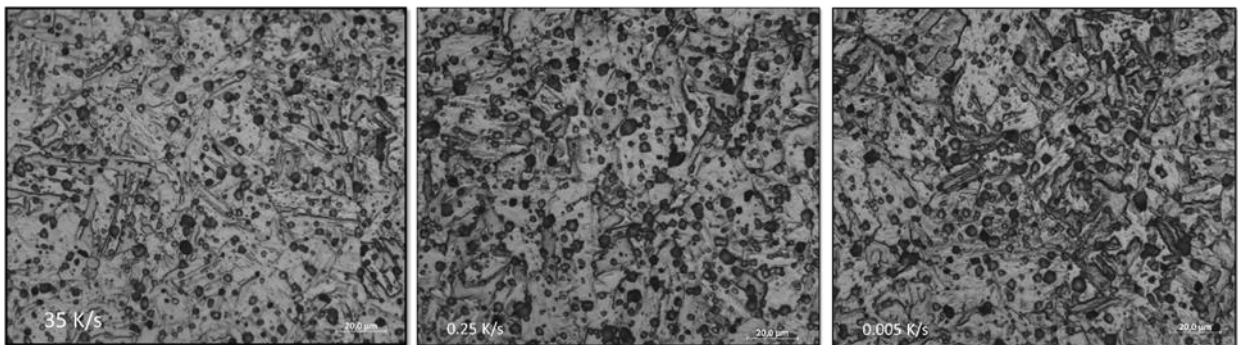
Figure 67. Microstructure of as-quenched 17-4 PH samples at different cooling rate 35 K/s, 0.25 K/s and 0.005 K/s.

In contrast, the effect of the cooling rate on H13 is significant, as evidenced in Figure 68. Only the martensite temperature is observed at high cooling rates, while at lower cooling rates, bainitic and pearlitic transformations are visible. All three microstructures depending on the cooling rate observed, are displayed in Figure 69.
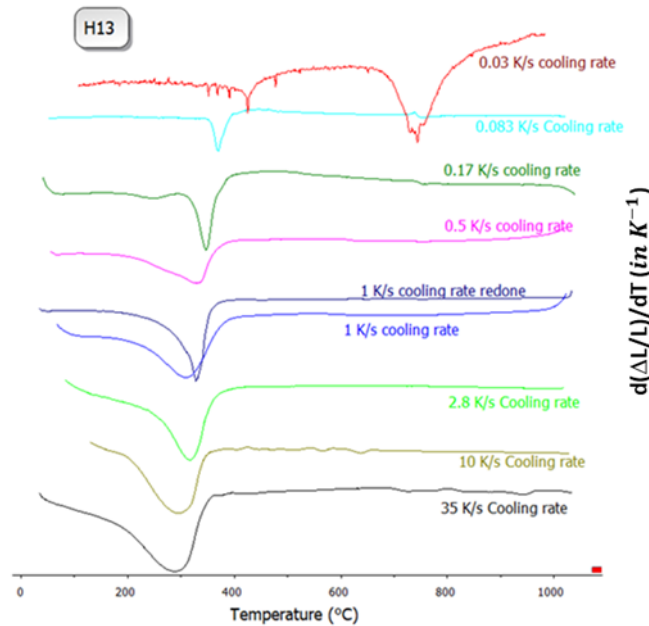
Figure 68. Influence of cooling rate on derivative strain curves.

With the fastest cooling rate of 35 K/s, a fine martensitic microstructure with prior austenite grain boundaries was formed. At the cooling rate of 0.5 K/s, bainite and martensite formation was noticed with their overlapping peaks at around 350 °C in the derivative strain curve. The slowest cooling rate of 0.03 K/s resulted in forming of a new pearlitic phase, as seen in the microstructure in Figure 69. The quenching rate has an impact on the hardness of the steel. Faster quenching rates lead to a higher hardness because of martensite formation. Samples that contain bainite have a lower hardness than martensite but a higher hardness than samples that contain pearlite.
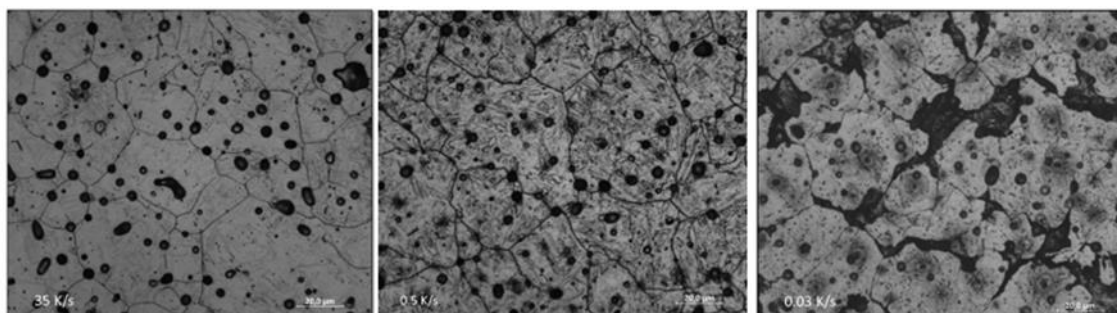
Figure 69. Microstructure of as-quenched H13 samples at a different cooling rates 35 K/s, 0.5 K/s and 0.03 K/s.

The relationship established between average hardness values (HV1) and cooling rates in both 17-4 PH and H13 samples are plotted in Figure 70. The evolution of hardness for 17-4 PH can be explained by Cu precipitation [48]. These microstructure information and hardness values of the as-quenched samples are then incorporated into the Continuous Cooling Transformation diagram of both the sheets of steel shown in Figure 71. These CCT diagrams are consistent with the literature corresponding to conventional materials. Therefore, the FFF process has a weak

effect on the microstructure and phase transformation, and standard heat treatment seems adapted to those materials.
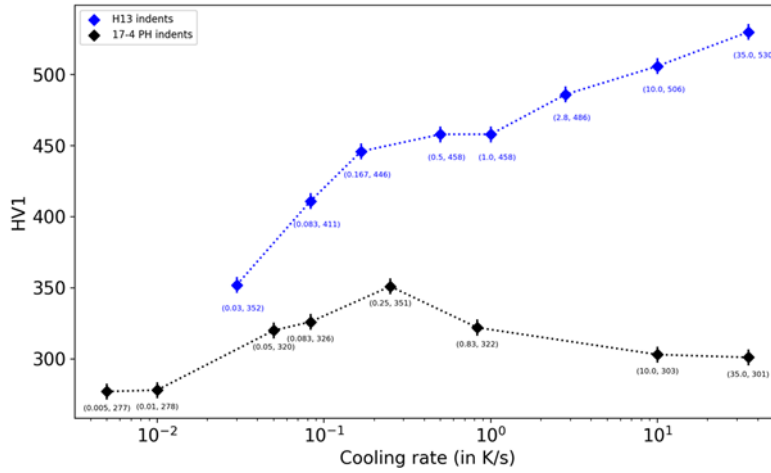
Figure 70. Hardness vs Cooling rate data for both steels.
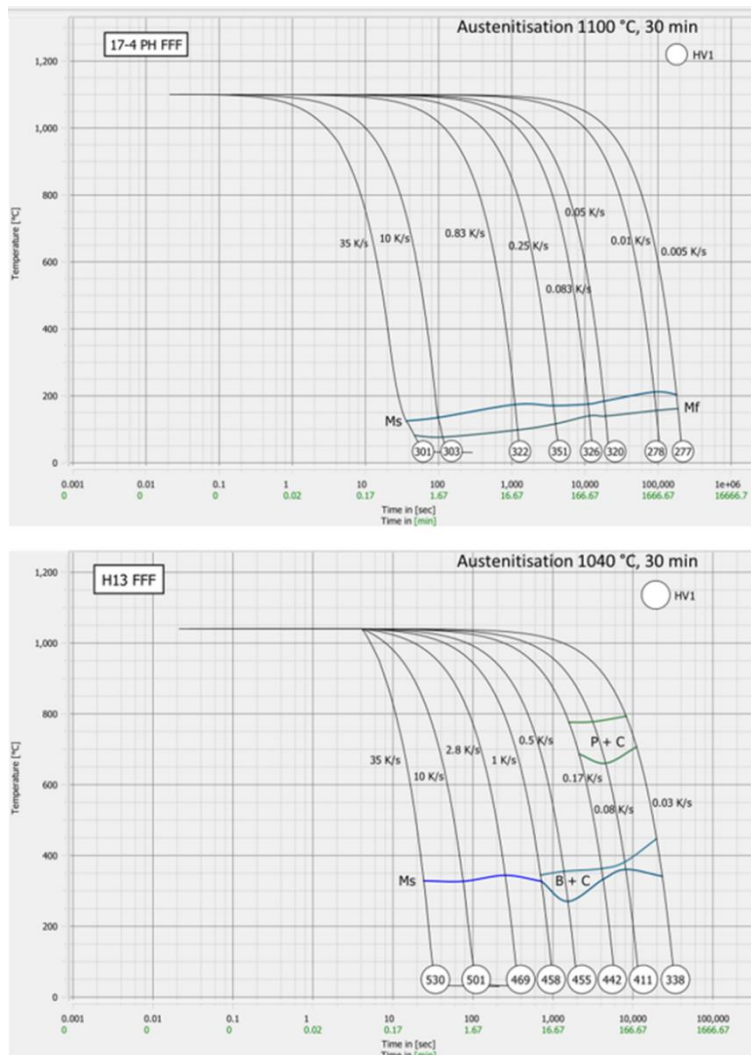
Figure 71. Continuous Cooling Transformation diagram of FFF manufactured 17-4 PH and H13.

> ➢ Mechanical properties in the sintered and HIPped parts manufactured with the Markforged Metal X machine.

Table 29. Obtained mechanical properties from tensile test for each material.

Material	R$_{p0.2}$ (Mpa)		Rm (Mpa)		A200 (%)	
	Average	Dev. St.	Average	Dev. St.	Average	Dev. St.
H13	263	10,2	583	10,7	16,4	0,7
H13 HIP	1439	13,9	1896	98,4	2,4	1
17.4-PH	707	7,6	1065	9,1	4,8	0,1

NDT analyses

All specimens were measured using following parameters
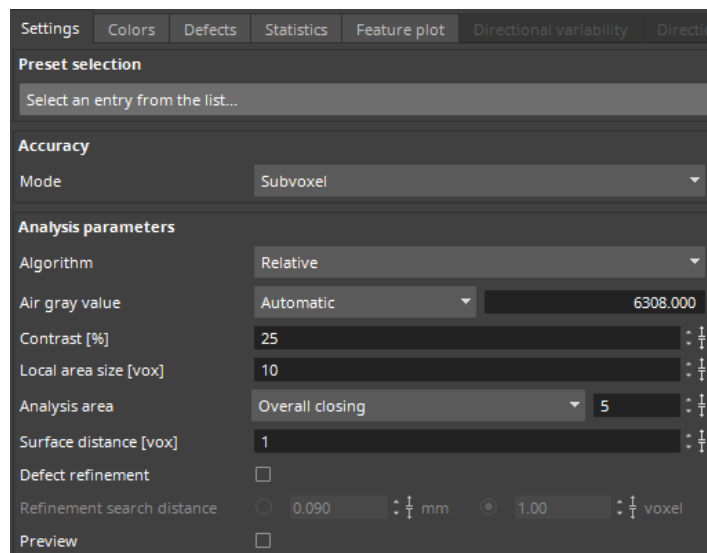
Figure 72. Parameters used for the NDT analyses.

Results:

GREEN	G-2

| M-DQDT5 | N-3 |
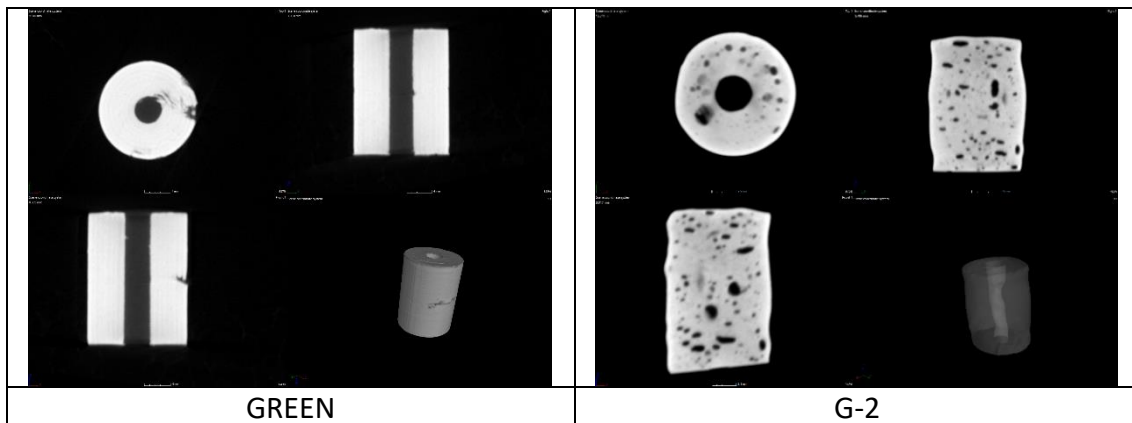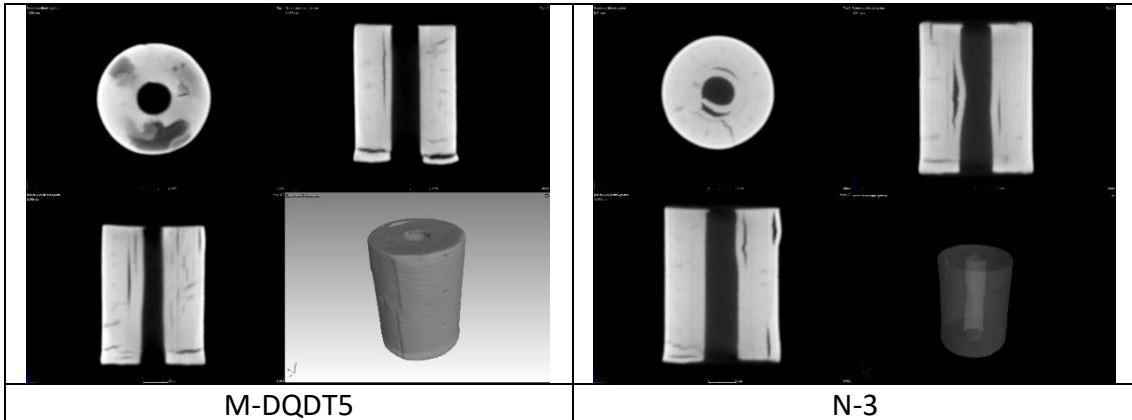
Figure 73. H13 Nanoe

| L3-H13 | L4-H13 |
| L5-H13 | L-2_H13 |
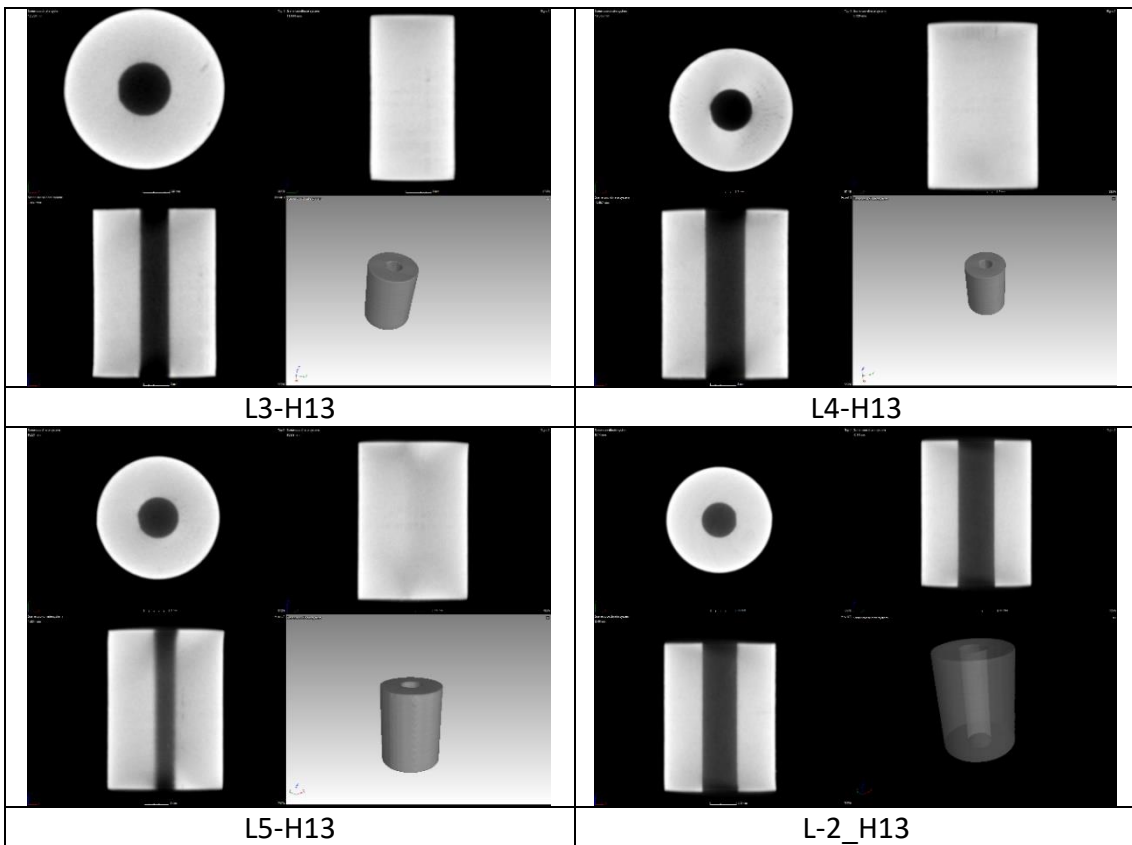
Figure 74. Markforged H13
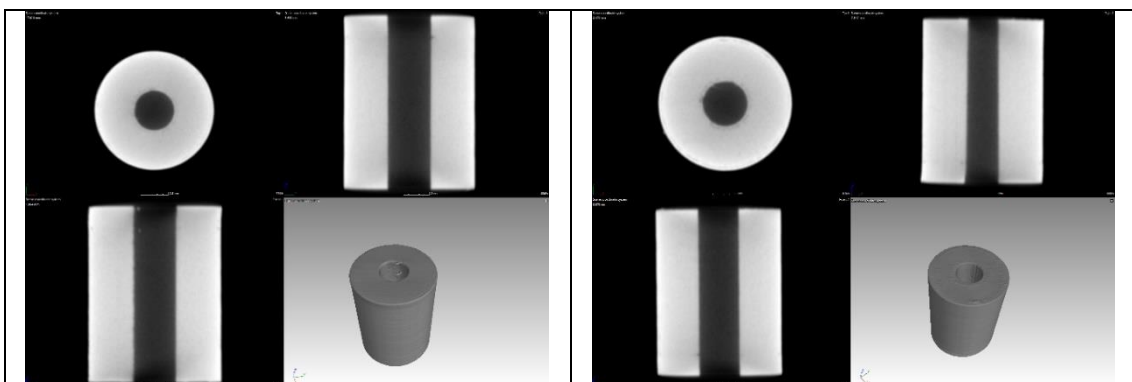
17_4PH-1	17_4PH-2

Figure 75. HIPped Markforged 17-4PH

I-2	F
I-HIP	F-HIP
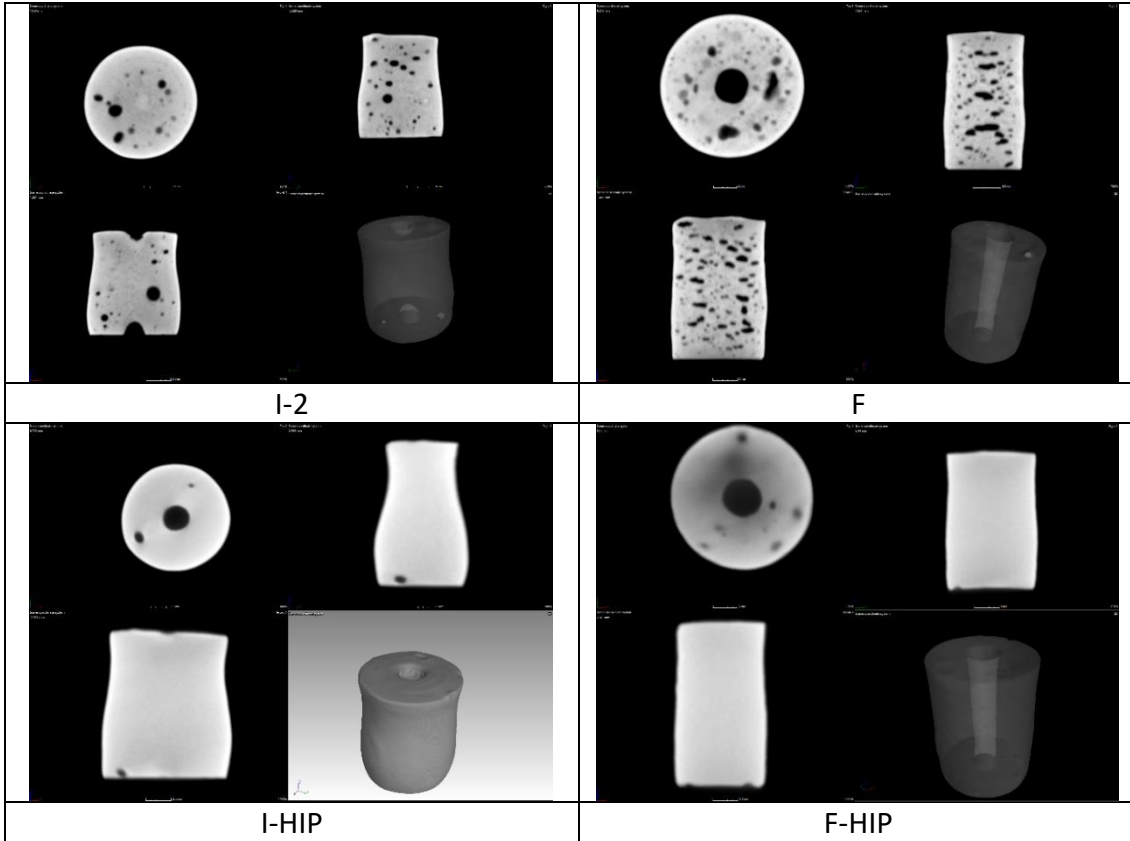
Figure 76. H13 HIP Nanoe

Conclusion and perspectives

The following conclusions can be drawn from this study:

- The porosity levels in the study were comparable to the predicted values given by the supplier's specifications and literature references. Both steel samples showed a slight porosity anisotropy, with the H13 selection having higher porosity and larger pores but less anisotropy compared to 17-4 PH.
- The filament had an unusual metal-polymer ratio of 40-60 % instead of the recommended 60-40 %. A better-suited matrix calcination technique could be considered to confirm this result. Despite this deviation, the porosity was comparable to the values reported in the literature, indicating that the lower metal-polymer ratio did not negatively impact the material's condition.
- Despite the slight anisotropy in porosity, hardness was minimal along the build direction and perpendicular to it. The microstructure observed was closer to wrought alloys than alloys processed through L-PBF, suggesting that the mechanical properties may be comparable to conventionally manufactured alloys rather than those produced through other additive manufacturing processes that involve melting.

- The CCT diagrams in the study match those found in the literature for conventional materials, suggesting that the FFF process has limited impact. It is worth mentioning that the hardness values are slightly lower, which could be due to material health. The as-received H13 showed low hardness, but it can increase by a factor of 3 after quenching.

The critical perspectives of this work could be:

- To determine the bulk mechanical properties of the as-received and heat-treated materials, focusing on conducting tensile tests further to confirm the absence of anisotropy in mechanical properties.
- To study the ageing process of 17-4 PH, as it is precipitation-hardening steel.

Pilot PT2-VIDRIMOLDE

Raw material characterization

Physical properties, interstitial elements and theoretical composition of the CX stainless steel powder with granulometry between +20-60 μm are gathered below (Table 30 and Table 31).

Table 30. Physical properties of the CX Stainless Steel powder.

Flow rate (s/50g)	Apparent density (g/cm^3)	Tap density (g/cm^3)	Pycnometer density (g/cm^3)
0.326	3.619	4.347	7.550

Table 31. Interstitial elements of the CX Stainless Steel powder.

O (%)	N (%)	C (%)	S (%)
0.0261	0.0075	0.0113	0.0030

Table 32. Theoretical composition of the CX Stainless Steel powder.

Elements	C	Cr	Ni	Mo	Al	Mn	Si
(%wt.)	0,05	11.00-13.00	8.40-11.00	1.10-1.30	1.20-2.00	0.40	0.40

On one hand, in Figure 77, electronic microscopy (SEM) images show a typical gas atomized powder with generally spherical shape and with the presence of several satellites and some splat.
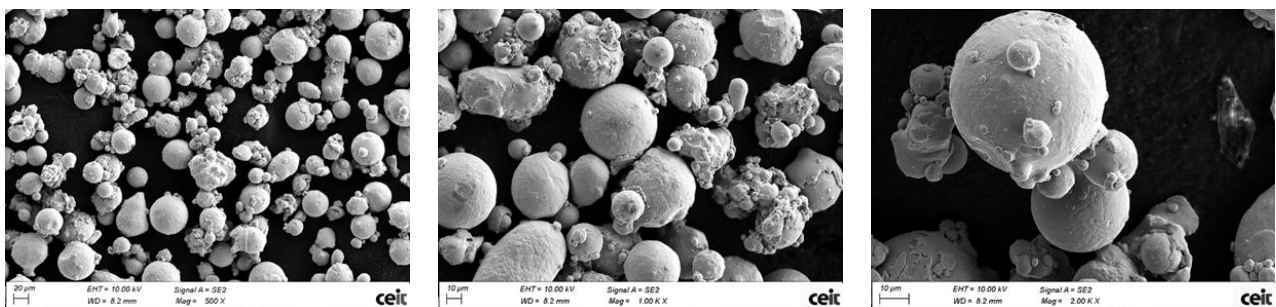
Figure 77. FEG-SEM images of the CX Stainless Steel powder.

On the other hand, cross section images of polished powder have been analyzed. Figure 78 show that there is no presence of internal porosity. Furthermore, the EDS analyses show homogeneous distribution of Cr, Ni, Mo, Al and Mn and zones enriched in Si.
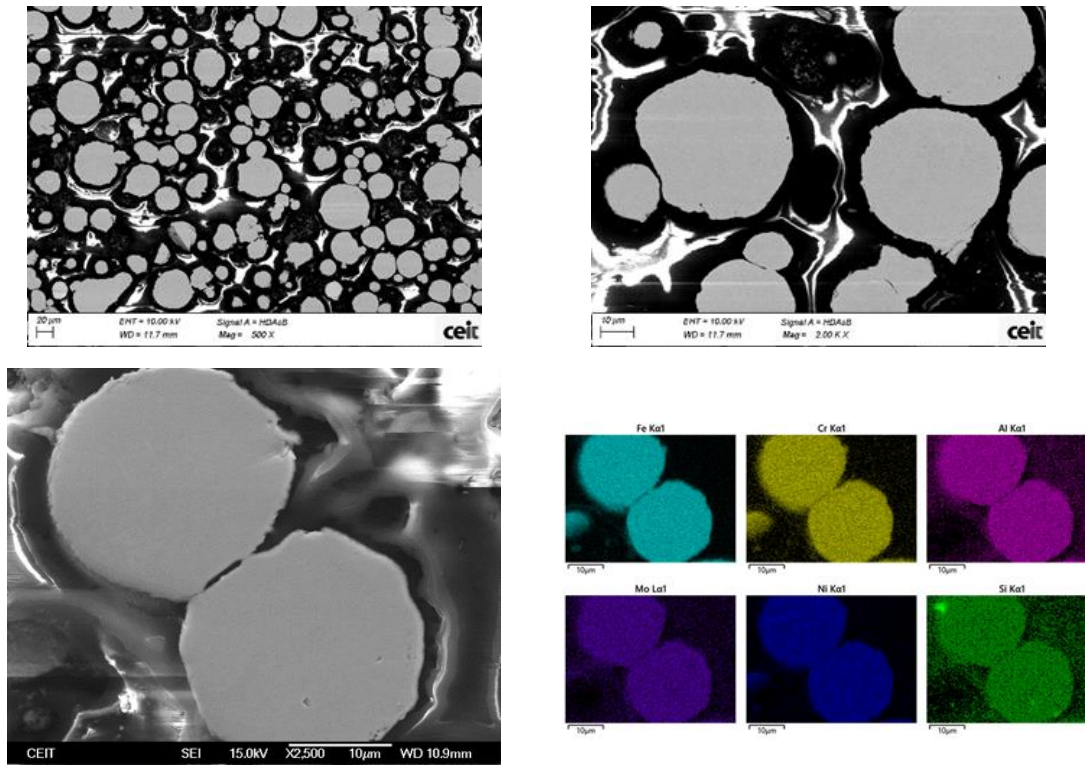
Figure 78. FEG-SEM images and EDS analysis (bottom) CX Stainless Steel powder

Finally, particle size distribution and powder sphericity has been measured using a Sympatec QIPIC/L02 with Rodos and Vibri as dispersion modules and results are collected in Table 33 and Figure 79. It can be asserted that both fulfill the requirements to be deposited by LPBF (sphericity close to one) with an average powder particle size of 38 µm.

Table 33. Particle size distribution and sphericity CX Stainless Steel powder

Dv(10) (µm)	24.17	S (10)	0.80
Dv(50) (µm)	37.77	S (50)	0.86
Dv(90) (µm)	58.33	S (90)	0.94
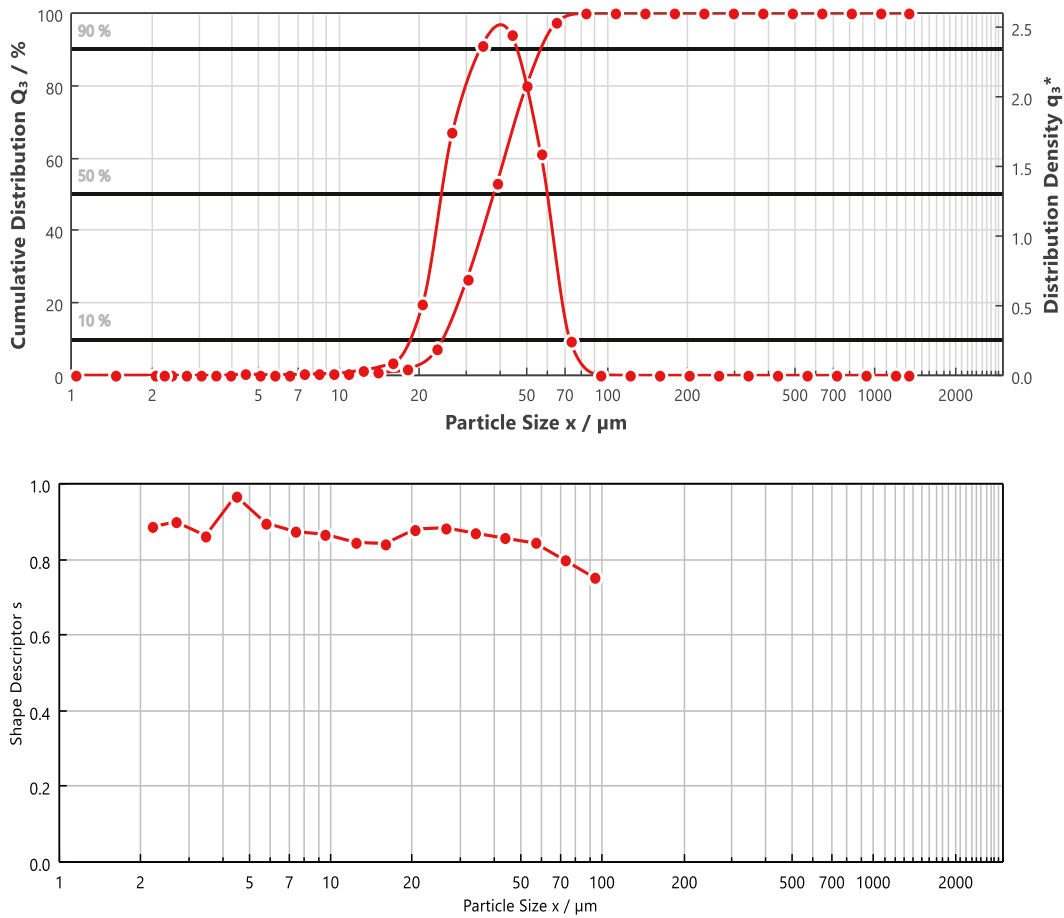
Figure 79. Particle size distribution (up) and shape factor (bottom) as function of the particle size of the CX Stainless Steel powder.

Microstructural characterisation

The hybridation of Laser Directed Energy Deposition (L-DED) with the Powder Bed Fusion (LPBF) process has been investigated. The objective of this work is to clear the following process parameters:

- Thickness of the solid layer covering the inner lattice structure. The research will seek to reduce this thickness value while still preventing the creation of defects on the structure inside.
- Fabrication parameters for the L-DED process, being these the laser power (P), feed rate (F) and powder flow (Q)

The study was performed in two steps. First, **single bead tests** were performed combining the parameter sets mentioned in table 33 with substrates of different thickness: 6, 1 and 0.7 mm The fabricated beads have a length of 25 mm and have been centred on the surface area of 15 mm x 32 mm.

Table 33. Single bead testing plan parameters.

N.	Test type	Parameter set	Substrate thickness (mm)
1	Single bead	Ref.	6
2	"	Reduced	6
3	"	Ref.	1
4	"	Reduced	1
5	"	Reduced	0.7

Secondly, **layer tests** using the reduced parameter values, on substrates of 2 and 1 mm of thickness was performed. These layers consist of 5 overlaid beads, with a distance of 1 mm between them. In order to simulate the effect a bigger deposition area would have on the fabrication process, a cooling time of 5 seconds is placed after each bead is deposited.

Table 34. Layer testing plan parameters.

N.	Test type	Parameter set	Substrate thickness (mm)
6	Layer	Reduced	2
7	"	Reduced	1

RESULTS

Bead tests

Two lines that distinguish a discontinuity in the substrate, following the dilution line were observed, Figure 80. This could indicate the formation of microcracking on the substrate.
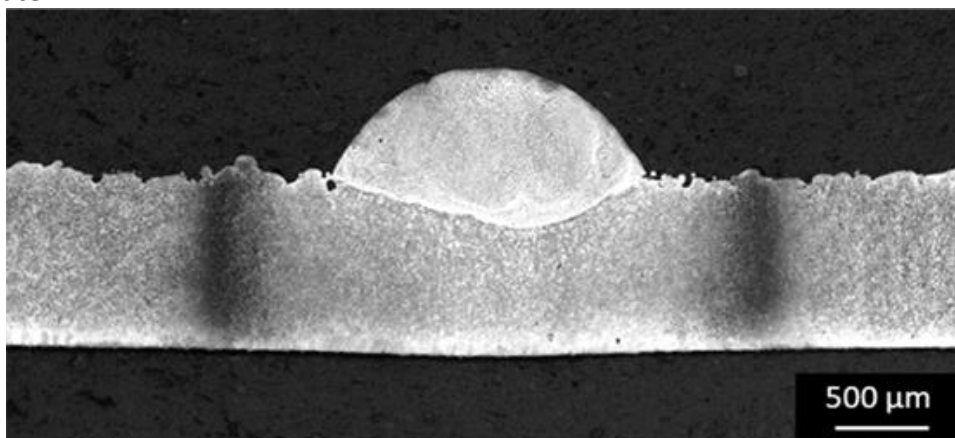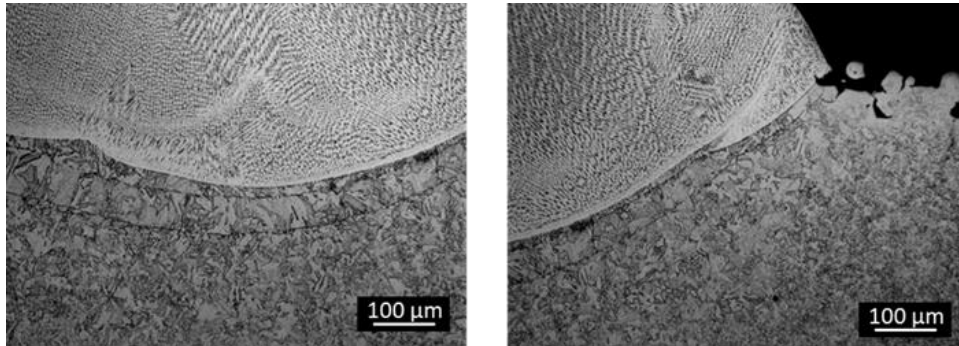
Figure 80. Cross-section of the bead test n 4.

Table 35. HAZ measurements of bead tests.

N.	Substrate thickness (mm)	HAZ Measurements (mm)
4	1	2.89
5	0.7	3.88

Layer tests

Cross-sections of the layers fabricated on a 2 mm and 1 mm thickness surface are gathered in figure 81.
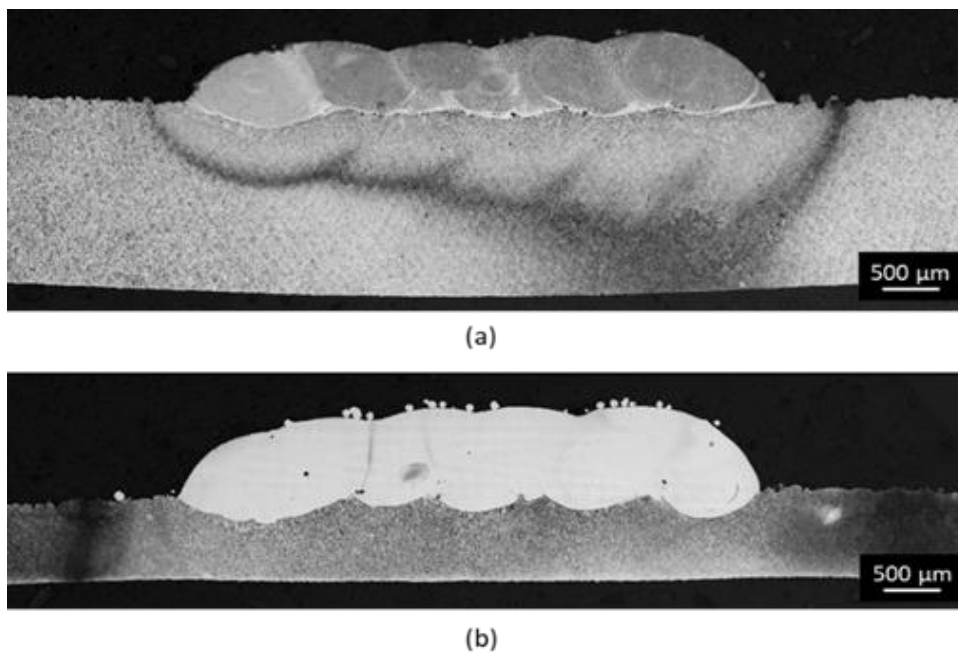
Figure 81. Cross-sections of the fabricated layers: (a) n.6 and (b) n.7.

Optimal process parameters for the L-DED process on a PBF substrate are the reduced ones from Table 36.

Table 36. Reference L-DED process parameter set.

	P (W)	F (mm/min)	Q (g/min)	P/F
Ref.	600	525	5.5	1.143
Reduced	500	525	5.5	0.952

The fabrication on a substrate as thin as 1 mm is feasible but with a significant deformation on the part as can be seen in the next Figure.
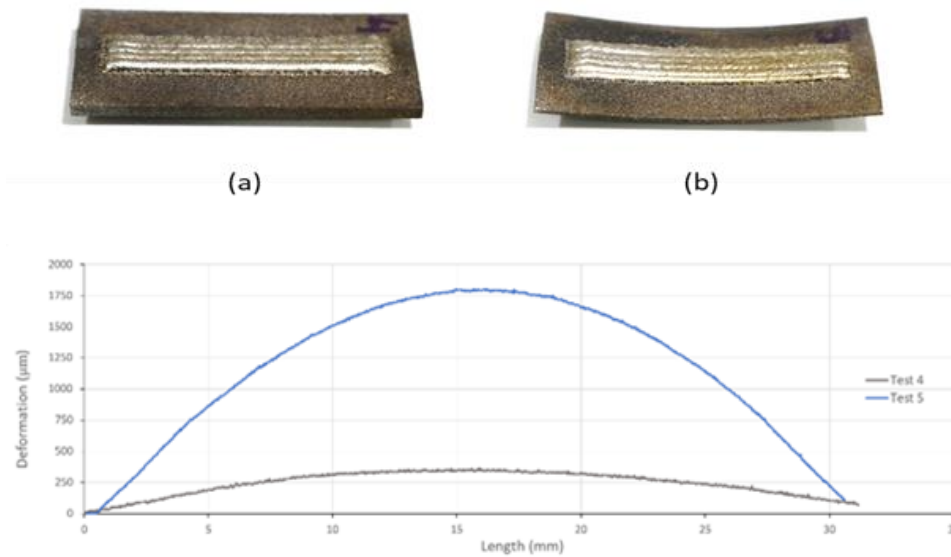
Figure 82. Deformation measurements in the n.4 and n.5 testing samples.

As a conclusion of the work done for Vidrimolde pilot the optimal manufacturing parameters were defined: Laser power (P) of 500 W, Feed rate (F) of 525 mm/min and Powder flow (Q) of 5.5 g/min are the optimal parameters for the deposition of material on thin substrates. With these parameters, substrates as thin as 0.7 mm can be used in the fabrication of single beads.

5. CONCLUSIONS

Materials used in the five pilots have been characterised in terms of microstructure, mechanical properties and other relevant characteristics. In all the cases, the materials have been chosen according to the requirements for each application and, after the intensive characterisation work performed in Additool, it can be confirmed that all the materials have successfully fulfil the requirements.

6. REFERENCES

[1] J. Schindelin *et al.*, "Fiji: an open-source platform for biological-image analysis," *Nat. Methods*, vol. 9, no. 7, pp. 676–682, Jul. 2012.

[2] Mirko Sinico; Ann Witvrouw; Wim Dewulf, "Influence of the particle size distribution on surface quality of Maraging 300 parts produced by Laser Powder Bed Fusion." Nantes, France, pp. 1–4, 2019.

[3] J. P. Kruth, L. Froyen, J. Van Vaerenbergh, P. Mercelis, M. Rombouts, and B. Lauwers, "Selective laser melting of iron-based powder," *J. Mater. Process. Technol.*, vol. 149, no. 1–3, pp. 616–622, Jun. 2004.

[4] J. Šafka, M. Ackermann, and L. Voleský, "Structural properties of H13 tool steel parts produced with use of selective laser melting technology," *J. Phys. Conf. Ser.*, vol. 709, p. 012004, Apr. 2016.

[5] G. Kasperovich, R. Becker, K. Artzt, P. Barriobero-Vila, G. Requena, and J. Haubrich, "The effect of build direction and geometric optimization in laser powder bed fusion of Inconel 718 structures with internal channels," *Mater. Des.*, vol. 207, p. 109858, Sep. 2021.

[6] L. Cao, J. Li, J. Hu, H. Liu, Y. Wu, and Q. Zhou, "Optimization of surface roughness and dimensional accuracy in LPBF additive manufacturing," *Opt. Laser Technol.*, vol. 142, p. 107246, Oct. 2021.

[7] A. du Plessis, "Effects of process parameters on porosity in laser powder bed fusion revealed by X-ray tomography," *Addit. Manuf.*, vol. 30, p. 100871, Dec. 2019.

[8] T. Reiber, J. Rüdesheim, M. Weigold, E. Abele, J. Musekamp, and M. Oechsner, "Influence of contour scans on surface roughness and pore formation using Scalmalloy® manufactured by laser powder bed fusion (PBF-LB)," *Materwiss. Werksttech.*, vol. 52, no. 4, pp. 468–481, Apr. 2021.

[9] K. Kempen, B. Vrancken, S. Buls, L. Thijs, J. Van Humbeeck, and J.-P. Kruth, "Selective Laser Melting of Crack-Free High Density M2 High Speed Steel Parts by Baseplate Preheating," *J. Manuf. Sci. Eng.*, vol. 136, no. 6, Dec. 2014.

[10] J. Saewe, C. Gayer, A. Vogelpoth, and J. H. Schleifenbaum, "Feasability Investigation for Laser Powder Bed Fusion of High-Speed Steel AISI M50 with Base Preheating System," *BHM Berg- und Hüttenmännische Monatshefte*, vol. 164, no. 3, pp. 101–107, Mar. 2019.

[11] S. Qin, S. Herzog, A. Kaletsch, and C. Broeckmann, "Effects of Pressure on Microstructure and Residual Stresses during Hot Isostatic Pressing Post Treatment of AISI M50 Produced by Laser Powder-Bed Fusion," *Metals (Basel).*, vol. 11, no. 4, p. 596, Apr. 2021.

[12] M. Balbaa, S. Mekhiel, M. Elbestawi, and J. McIsaac, "On selective laser melting of Inconel 718: Densification, surface roughness, and residual stresses," *Mater. Des.*, vol. 193, p. 108818, Aug. 2020.

[13] L. Scime and J. Beuth, "Melt pool geometry and morphology variability for the Inconel 718 alloy in a laser powder bed fusion additive manufacturing process," *Addit. Manuf.*, vol. 29, p. 100830, Oct. 2019.

[14] J. Kunz, J. Saewe, S. Herzog, A. Kaletsch, J. H. Schleifenbaum, and C. Broeckmann, "Mechanical Properties of High-Speed Steel AISI M50 Produced by Laser Powder Bed Fusion," *steel Res. Int.*, vol. 91, no. 5, p. 1900562, May 2020.

[15] T. DebRoy *et al.*, "Additive manufacturing of metallic components – Process, structure and properties," *Prog. Mater. Sci.*, vol. 92, pp. 112–224, Mar. 2018.

[16] BÖHLER, "W360 AMPO." [Online]. Available: https://www.bohler.fr/fr/products/w360-ampo-2/ (accessed February 23, 2023).

[17] C. M. Fang, M. H. F. Sluiter, M. A. van Huis, C. K. Ande, and H. W. Zandbergen, "Origin of Predominance of Cementite among Iron Carbides in Steel at Elevated Temperature," *Phys. Rev. Lett.*, vol. 105, no. 5, p. 055503, Jul. 2010.

[18] F. Wang, D. Qian, L. Xie, Z. Dong, and X. Song, "Microstructure Evolution and Tempering Transformation Kinetics in a Secondary Hardened M50 Steel Subjected to Cold Ring Rolling," *ISIJ Int.*, vol. 61, no. 1, pp. 361–371, Jan. 2021.

[19] C. K. Ande and M. H. F. Sluiter, "First-Principles Calculations on Stabilization of Iron Carbides (Fe3C, Fe5C2, and η-Fe2C) in Steels by Common Alloying Elements," *Metall. Mater. Trans. A*, vol. 43, no. 11, pp. 4436–4444, Nov. 2012.

[20] E. . Morra, P.V., Böttger, A.J. & Mittemeijer, "Decomposition of Iron-based Martensite. A kinetic analysis by means of differential scanning calorimetry and dilatometry," *J. Therm. Anal. Calorim.*, vol. 64, pp. 905–914, 2001.

[21] A. Verma, M. Sundararaman, J. B. Singh, and S. A. Nalawade, "A new method for determining the Curie temperature using a dilatometer," *Meas. Sci. Technol.*, vol. 21, no. 10, p. 105106, Oct. 2010.

[22] V. B. E. ¬Co KG, "Hot Work Tool Steel. BÖHLER W360 ISOBLOC."

[23] P. Yang *et al.*, "Effect of thermal annealing on microstructure evolution and mechanical behavior of an additive manufactured AlSi10Mg part," *J. Mater. Res.*, vol. 33, no. 12, pp. 1701–1712, Jun. 2018.

[24] P. D. Nezhadfar, S. Thompson, A. Saharan, N. Phan, and N. Shamsaei, "Structural integrity of additively manufactured aluminum alloys: Effects of build orientation on microstructure, porosity, and fatigue behavior," *Addit. Manuf.*, vol. 47, p. 102292, Nov. 2021.

[25] M. Buttard *et al.*, "Multi-scale microstuctural investigation of a new Al-Mn-Ni-Cu-Zr aluminium alloy processed by laser powder bed fusion," *Materialia*, vol. 18, p. 101160, Aug. 2021.

[26] J. R. Croteau *et al.*, "Microstructure and mechanical properties of Al-Mg-Zr alloys processed by selective laser melting," *Acta Mater.*, vol. 153, pp. 35–44, Jul. 2018.

[27] C. Galera-Rueda, M. L. Montero-Sistiaga, K. Vanmeensel, M. Godino-Martínez, J. Llorca, and M. T. Pérez-Prado, "Icosahedral quasicrystal-enhanced nucleation in Al alloys fabricated by selective laser melting," *Addit. Manuf.*, vol. 44, p. 102053, Aug. 2021.

[28] S. Griffiths, M. D. Rossell, J. Croteau, N. Q. Vo, D. C. Dunand, and C. Leinenbach, "Effect of laser rescanning on the grain microstructure of a selective laser melted Al-Mg-Zr alloy," *Mater. Charact.*, vol. 143, pp. 34–42, Sep. 2018.

[29] J. H. Martin, B. D. Yahata, J. M. Hundley, J. A. Mayer, T. A. Schaedler, and T. M. Pollock, "3D printing of high-strength aluminium alloys," *Nature*, vol. 549, no. 7672, pp. 365–369, Sep. 2017.

[30] R. Mertens, L. Baert, K. Vanmeensel, and B. Van Hooreweder, "Laser powder bed fusion of high strength aluminum," *Mater. Des. Process. Commun.*, vol. 3, no. 5, Oct. 2021.

[31] R. A. Michi *et al.*, "Microstructural evolution and strengthening mechanisms in a heat-treated additively manufactured Al–Cu–Mn–Zr alloy," *Mater. Sci. Eng. A*, vol. 840, p. 142928, Apr. 2022.

[32] A. B. Spierings *et al.*, "Microstructural features of Sc- and Zr-modified Al-Mg alloys processed by selective laser melting," *Mater. Des.*, vol. 115, pp. 52–63, Feb. 2017.

[33] P. J. Spierings, A. B., Dawson, K., Voegtlin, M., & Palm, F., Uggowitzer, "Microstructure and mechanical properties of as-processed scandium-modified aluminum using selective laser melting," *CIRP Ann. - Manuf. Technol.*, vol. 65, pp. 213–216, 2016.

[34] K. V. Yang, Y. Shi, F. Palm, X. Wu, and P. Rometsch, "Columnar to equiaxed transition in Al-Mg(-Sc)-Zr alloys produced by selective laser melting," *Scr. Mater.*, vol. 145, pp. 113–117, Mar. 2018.

[35] H. Zhang, H. Zhu, X. Nie, J. Yin, Z. Hu, and X. Zeng, "Effect of Zirconium addition on crack, microstructure and mechanical behavior of selective laser melted Al-Cu-Mg alloy," *Scr. Mater.*, vol. 134, pp. 6–10, Jun. 2017.

[36] P. Yang, L. A. Deibler, D. R. Bradley, D. K. Stefan, and J. D. Carroll, "Microstructure evolution and thermal properties of an additively manufactured, solution treatable AlSi10Mg part," *J. Mater. Res.*, vol. 33, no. 23, pp. 4040–4052, Dec. 2018.

[37] J. Costa, E. Sequeiros, M. T. Vieira, and M. Vieira, "Additive Manufacturing," *U.Porto J. Eng.*, vol. 7, no. 3, pp. 53–69, Apr. 2021.

[38] T. C. Henry, M. A. Morales, D. P. Cole, C. M. Shumeyko, and J. C. Riddick, "Mechanical behavior of 17-4 PH stainless steel processed by atomic diffusion additive manufacturing," *Int. J. Adv. Manuf. Technol.*, vol. 114, no. 7–8, pp. 2103–2114, Jun. 2021.

[39] C. S. Y. Wu, R.M. German, D. Blaine, B. Marx, "Effects of residual carbon content on

sintering shrinkage, microstructure and mechanical properties of injection molded 17-4 PH stainless steel," *J. Mater. Sci.*, vol. 37, pp. 3573–3583, 2002.

[40]   S. Sabooni *et al.*, "Laser powder bed fusion of 17–4 PH stainless steel: A comparative study on the effect of heat treatment on the microstructure evolution and mechanical properties," *Addit. Manuf.*, vol. 46, p. 102176, Oct. 2021.

[41]   S.-M. Yeon *et al.*, "Normalizing Effect of Heat Treatment Processing on 17-4 PH Stainless Steel Manufactured by Powder Bed Fusion," *Metals (Basel).*, vol. 12, no. 5, p. 704, Apr. 2022.

[42]   L. Zai *et al.*, "Laser Powder Bed Fusion of Precipitation-Hardened Martensitic Stainless Steels: A Review," *Metals (Basel).*, vol. 10, no. 2, p. 255, Feb. 2020.

[43]   J. Schröder *et al.*, "On the influence of heat treatment on microstructure and mechanical behavior of laser powder bed fused Inconel 718," *Mater. Sci. Eng. A*, vol. 805, p. 140555, Feb. 2021.

[44]   M. Ozer, "Influence of heat treatments on microstructure and wear behavior of AISI H13 tool steel," *Kov. Mater. Mater.*, vol. 60, no. 6, Nov. 2022.

[45]   "Markforged_H13_V1.1_fr.pdf." 2023.

[46]   P. Nandwana, R. Kannan, and D. Siddel, "Microstructure evolution during binder jet additive manufacturing of H13 tool steel," *Addit. Manuf.*, vol. 36, p. 101534, Dec. 2020.

[47]   "17-4PH-v2-SS-Datasheet.pdf." 2023.

[48]   C. Rowolt, B. Milkereit, A. Springer, C. Kreyenschulte, and O. Kessler, "Dissolution and precipitation of copper-rich phases during heating and cooling of precipitation-hardening steel X5CrNiCuNb16-4 (17-4 PH)," *J. Mater. Sci.*, vol. 55, no. 27, pp. 13244–13257, Sep. 2020.

[49]   "SITHERM 2344 Steel (Mat.No. 1.2344, DIN X40CrMoV51, AISI H13)." 2023.

[50]   F. Deirmina, N. Peghini, B. AlMangour, D. Grzesiak, and M. Pellizzari, "Heat treatment and properties of a hot work tool steel fabricated by additive manufacturing," *Mater. Sci. Eng. A*, vol. 753, pp. 109–121, Apr. 2019.

[51]   F. Christien, M. T. F. Telling, and K. S. Knight, "A comparison of dilatometry and in-situ neutron diffraction in tracking bulk phase transformations in a martensitic stainless steel," *Mater. Charact.*, vol. 82, pp. 50–57, Aug. 2013.

[52]   R. Kapoor and I. S. Batra, "On the α' to γ transformation in maraging (grade 350), PH 13-8 Mo and 17-4 PH steels," *Mater. Sci. Eng. A*, vol. 371, no. 1–2, pp. 324–334, Apr. 2004.

[53]   H. R. Lashgari, C. Kong, E. Adabifiroozjaei, and S. Li, "Microstructure, post thermal treatment response, and tribological properties of 3D printed 17-4 PH stainless steel," *Wear*, vol. 456–457, p. 203367, Sep. 2020.

Interreg
Sudoe

EUROPEAN UNION

ADDiTOOL

European Regional Development Fund

www.additool.eu